SANDIA REPORT
SAND2002-1890
Unlimited Release
Printed October 2002

Surface Measurements of a Supersonic Jet in Subsonic Compressible Crossflow for the Validation of Computational Models

Steven J. Beresh, John F. Henfling, and Rocky J. Erven

Prepared by
Sandia National Laboratories
Albuquerque, New Mexico 87185 and Livermore, California 94550

Sandia is a multiprogram laboratory operated by Sandia Corporation, a Lockheed Martin Company, for the United States Department of Energy under Contract DE-AC04-94AL85000.

Issued by Sandia National Laboratories, operated for the United States Department of Energy by Sandia Corporation.

Available to DOE and DOE contractors from
U.S. Department of Energy
Office of Scientific and Technical Information
P.O. Box 62
Oak Ridge, TN 37831

Telephone: (865)576-8401
Facsimile: (865)576-5728
E-Mail: reports@adonis.osti.gov
Online ordering: http://www.doe.gov/bridge

Available to the public from
U.S. Department of Commerce
National Technical Information Service
5285 Port Royal Rd
Springfield, VA 22161

Telephone: (800)553-6847
Facsimile: (703)605-6900
E-Mail: orders@ntis.fedworld.gov
Online order: http://www.ntis.gov/ordering.htm

SAND2002-1890
Unlimited Release
Printed October 2002

Surface Measurements of a Supersonic Jet in Subsonic Compressible Crossflow for the Validation of Computational Models

Steven J. Beresh, John F. Henfling, and Rocky J. Erven
Engineering Sciences Center
Sandia National Laboratories
P.O. Box 5800
Albuquerque, NM 87185-0834

Abstract

Despite many decades of jet-in-crossflow experimentation, a distinct lack of data remains for a supersonic jet exhausting into a subsonic compressible crossflow. The present investigation seeks to address this deficiency by examining the flowfield structure of a Mach 3.73 jet injected transversely from a flat plate into a subsonic compressible freestream. The experimental results described herein include the mean surface pressure field as mapped using static pressure taps on the flat plate and an identification of flow features by employing an oil-based surface flow tracer. The possibility of flow separation within the nozzle itself also is addressed using pressure taps along the nozzle interior wall, as is the asymmetry of the separation line due to the variation of the local backpressure around the perimeter of the nozzle orifice resulting from the jet-in-crossflow interaction. Pressure data both on the flat plate and within the nozzle are presented at numerous angles with respect to the crossflow freestream direction to provide a breadth of measurements throughout the interaction region. Since the data are intended for use in validating computational models, attention is paid to providing details regarding the experimental geometry, boundary conditions, flowfield nonuniformities, and uncertainty analyses. Eight different sets of data are provided, covering a range of values of the jet-to-freestream dynamic pressure ratio from 2.8 to 16.9 and a freestream Mach number range of 0.5 to 0.8.

Acknowledgments

The authors would like to express their appreciation to both the Engineering Sciences Research Foundation, guided by Arthur C. Ratzel, and the Campaign 6 (formerly MAVEN) program, guided by Jaime L. Moya, for funding the research contained herein. The aforementioned program managers have exhibited great patience while substantial amounts of hardware were fabricated and rebuilt and in allowing the present study to reach fruition.

In addition, the authors would like to thank the following Sandia staff members for their insightful advice and discussions, without which these efforts would have significantly less attractive results: Vincent A. Amatucci, William L. Oberkampf, Jeffrey L. Payne, Carl W. Peterson, Michael R. Prairie, Christopher J. Roy, Walter H. Rutledge, and Walter P. Wolfe.

Contents

Tables

Figures

Nomenclature

c_p	pressure coefficient
d	jet exit diameter
J	jet-to-freestream dynamic pressure ratio, $J=(p_e M_e^2) / (p_w M_8)$
l	nozzle axial position measured from throat
l_0	nozzle expansion length
M	Mach number
M_8	freestream Mach number
M_e	jet exit Mach number
p	pressure
P_0	freestream stagnation pressure
P_{0j}	jet stagnation pressure
p_e	jet exit pressure
p_w	freestream static wall pressure, measured upstream of the jet interaction
T_0	freestream stagnation temperature
T_{0j}	jet stagnation temperature
u	velocity
x	distance from center of nozzle exit
?	specific heat ratio
?	gas density
?	nozzle installation orientation (?=0° is aligned with the wind tunnel freestream)

1 Introduction

Though a jet in crossflow is one of the classic problems in fluid dynamics, surprisingly little research has been conducted on a supersonic jet in subsonic compressible crossflow. This lack of data has forced aerodynamicists to adapt results from incompressible or entirely supersonic flowfields to the transonic regime and offers computationalists little assistance with code validation. As a result, the detailed physics of this problem are incompletely understood, which impacts, for example, the design of transonic flight vehicles that rely on supersonic jets for attitude or roll control. The difficulty is markedly worse for more complex geometries, such as those involving asymmetric nozzles or a jet-fin interaction.

While past jet-in-crossflow research endeavors have largely focused on incompressible flowfields or entirely supersonic flowfields, a few studies have examined a supersonic jet in subsonic compressible crossflow. One of the most useful was reported by Chocinski et al.[1] and Chocinski,[2] who provided surface pressure measurements and surface flow tracers of a Mach 2.5 jet issuing transversely from a flat plate into a Mach 0.75 crossflow. Mean flowfield measurements of the velocity field and total pressure field also were gathered at several crossplanes using five-hole pressure probes. Other researchers have obtained surface pressure measurements both for flat plate[3] and axisymmetric[4,5] configurations of a supersonic jet exhausting into subsonic compressible crossflow, and some analytical efforts also have been published.[6-8] A few additional efforts have involved sonic jets exhausting into a subsonic compressible freestream.[9-13]

The present research program aims to explore the flowfield behavior of a supersonic jet in subsonic compressible crossflow and to compare the results with the analogous incompressible and fully supersonic flowfields. The research presented here is restricted to the relatively simple flowfield produced by an axisymmetric jet transversely injected from a flat plate and concerns the examination of surface flow features using a fluorescent oil tracer to reveal the surface streamline patterns and extensive measurement of surface pressures. Measurements on the flat plate seek to reveal such physical phenomena as separated flow regions, vortex locations, and the extent of the jet's wake. The possibility of flow separation within the nozzle itself is addressed by pressure measurements along the inside wall of the nozzle, as it is believed to be a potential occurrence under conditions likely to be experienced by transonic flight vehicles of interest. While supersonic nozzle flow separation has previously been investigated for free jet configurations,[14-29] no experiments known to the present authors have examined this possibility for supersonic jet-in-crossflow interactions. These data will help fill a substantial gap in the jet-in-crossflow literature by identifying variations in the flowfield structure for transonic crossflows.

An important component of the present research is to acquire data with sufficient breadth and detail to meet the specific needs for the validation of computational models. As development of Sandia's ASCI codes proceeds, it is vital to provide data specifically designed for an unambiguous comparison between experimental and numerical results, as well as to aid in the evolution of the underlying physical models. Past efforts have shown

that most existing data sets do not meet the criteria necessary for such validation activities and experiments must be conducted specifically for this purpose, providing not just the main body of data but also the ancillary information (e.g., boundary conditions) necessary for computational modeling.[30-33] The present study of a jet-in-crossflow interaction has been identified as one of the most critical cases for the validation of Sandia's compressible fluid mechanics codes.[34] This is partly because of its direct bearing on the performance of specific flight systems and partly because it encompasses a significant range of complex physical phenomena, including wall-bounded flows, free shear flows, turbulent separated flows, and unsteady flows. These fluid mechanics phenomena must be accurately simulated not just for those flight vehicles employing attitude or roll-control jets, but also for a wide variety of flowfields important to other flight vehicles, which makes jet-in-crossflow interactions especially attractive as a source of validation data.

The present experiment was designed to meet these validation needs. In the process of investigating the surface flowfield properties of the transonic jet-in-crossflow interaction, data were acquired specifically for code validation activities. These include not just careful measurements of the flowfield itself, but also a characterization of boundary conditions and wind tunnel flow parameters that are a necessary constituent of any validation activity. Such a characterization of the wind tunnel flow is presented to the extent possible using the measurement techniques of the present investigation. The intention of the current document is to provide the experimental details and the resulting data in as complete a manner as possible. Previous publications concerning the present research have focused upon physical discovery of the transonic jet-in-crossflow interaction;[35,36] this document focuses upon providing the requisite data needed to support code validation.

2 Experimental Apparatus

2.1 Trisonic Wind Tunnel

All experiments were performed in Sandia's Trisonic Wind Tunnel (TWT). The TWT is a blowdown-to-atmosphere facility with five interchangeable test sections, each using air as the test gas. One is a transonic nozzle permitting a continuously variable Mach number from 0.5 to 1.3, the walls of which are perforated to prevent the reflection of shock waves and also to ease tunnel blockage restrictions near sonic conditions. During typical use, the 305 × 305 mm^2 (12 × 12 $inch^2$) rectangular test section traditionally has been fitted with either four porous walls or two porous walls (top and bottom) and two solid walls (the side walls) containing windows used primarily for schlieren imaging. Models mount at the tunnel centerline on a pitching strut and sting. The test section is enclosed in a pressurized plenum to contain the flow that passes through the porous walls. Four other contoured nozzles provide supersonic Mach numbers of 1.5, 2.0, 2.5, and 3.0.

Recent modifications to the TWT have been necessary to meet the needs of both jet-in-crossflow experimentation and the validation of CFD models. Because all experiments were conducted in a transonic freestream, modifications were required only for the transonic test section. Its porous walls have been replaced with solid walls for the present experiments, typically of surface roughness 1 micron rms (32 microinches rms) but in some places 2 micron rms (63 microinches rms). This was intended both to supply a flat plate from which the jet will issue and to provide computationally tractable boundary conditions for comparison of experimental data with numerical simulations. Whereas porous walls introduce a numerically imprecise aspect into the model, the solid walls remove this source of potential ambiguity and thus enhance the opportunity for a meaningful quantitative assessment of CFD model performance. Use of a wall-mounted jet was deemed superior to a sting-mounted flat plate to avoid such uncertainties as plate deflection and flow interference from the jet supply apparatus beneath the plate, both of which would pose additional complications for comparison between experiments and simulations. While use of a solid-wall test section limits the Mach number range of the flowfield, this does not pose a significant impediment because experiments are not planned for near-sonic or supersonic conditions. Further modifications have been made to provide a high-pressure, high-flow-rate gas source for the jet. The upgrades to the TWT also have included improvements to the optical access (which are notably easier for a solid-wall test section of this modest size as opposed to porous walls) and flow seeding capabilities for future experiments utilizing laser-based instrumentation.

Although the present experiment mounts all apparatus from the wind tunnel walls rather than utilizing the pitching strut, the strut itself cannot be removed from the wind tunnel. The sting was removed from the strut and replaced with a blank that maintained the streamlined contour of the strut. The entire strut remained downstream of the end of the test section and thus its influence was minimized. The leading edge of the strut was 139.7 mm (5.5 inch) from the end of the test section at its centerline and 102.9 mm (4.05 inch) away at its closest point at the top or bottom wall.

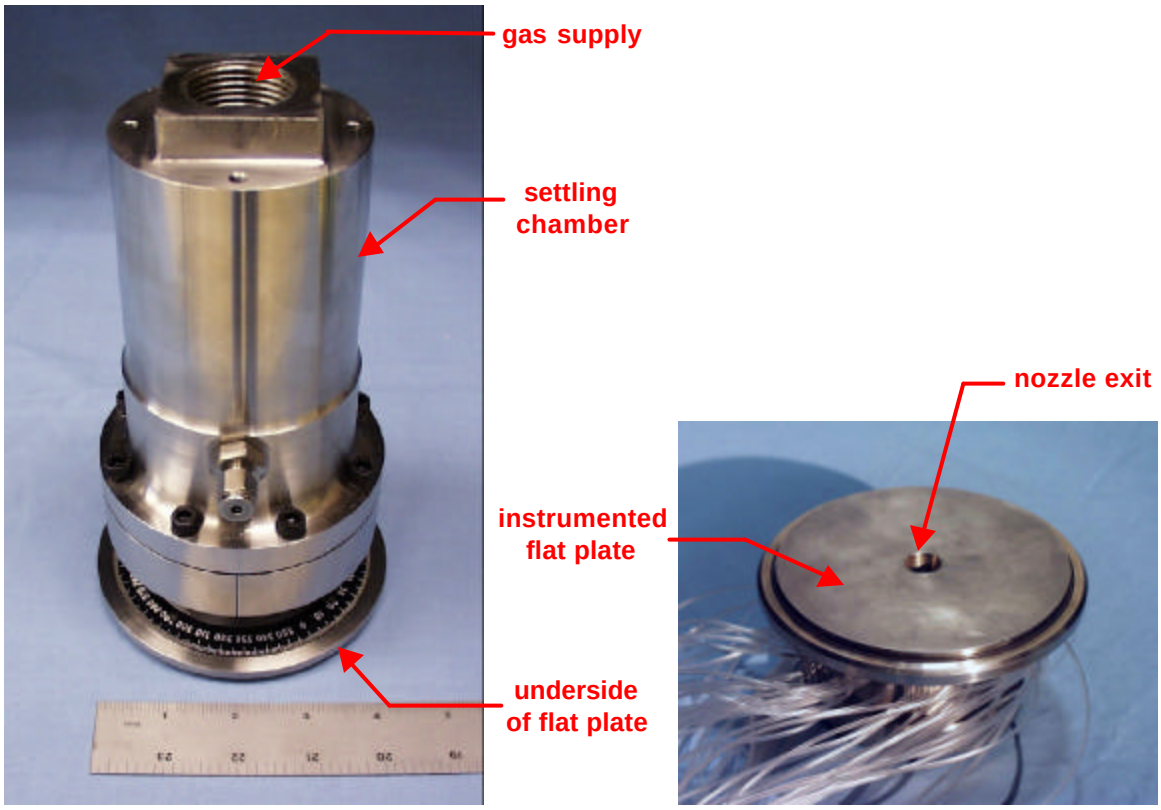

(a) (b)

Figure 1: Supersonic jet nozzle hardware; (a) the settling chamber and nozzle assembly; (b) one of the interchangeable nozzles.

2.2 Supersonic Jet Hardware

Multiple conical nozzles were fabricated for the transverse jet. For the work reported in this document, all nozzles are axisymmetric with a design Mach number of 3.73 and an expansion half-angle of 15°; they differ only in their instrumentation and exit diameter. The three nozzles used in the present study have an exit diameter of 12.7 mm (0.50 inch). One nozzle is instrumented with pressure taps on the flat plate from which the jet emanates to measure surface pressures beneath the jet-in-crossflow interaction, and a second nozzle is instrumented within the nozzle itself to allow an examination of internal flow separation. The remaining nozzle is uninstrumented. Further details are found below in section 2.3.1. The surface roughness of the nozzle contour is 1 micron rms (32 microinches rms).

Any of the interchangeable nozzles may be connected to a settling chamber located behind either the top wall of the transonic test section or one of the side walls. The settling chamber is designed to pressurize to a maximum of 14 MPa (2000 psi) and is instrumented with a transducer and a thermocouple to provide stagnation pressure and temperature measurements. A photograph of the settling chamber is shown in Figure 1a.

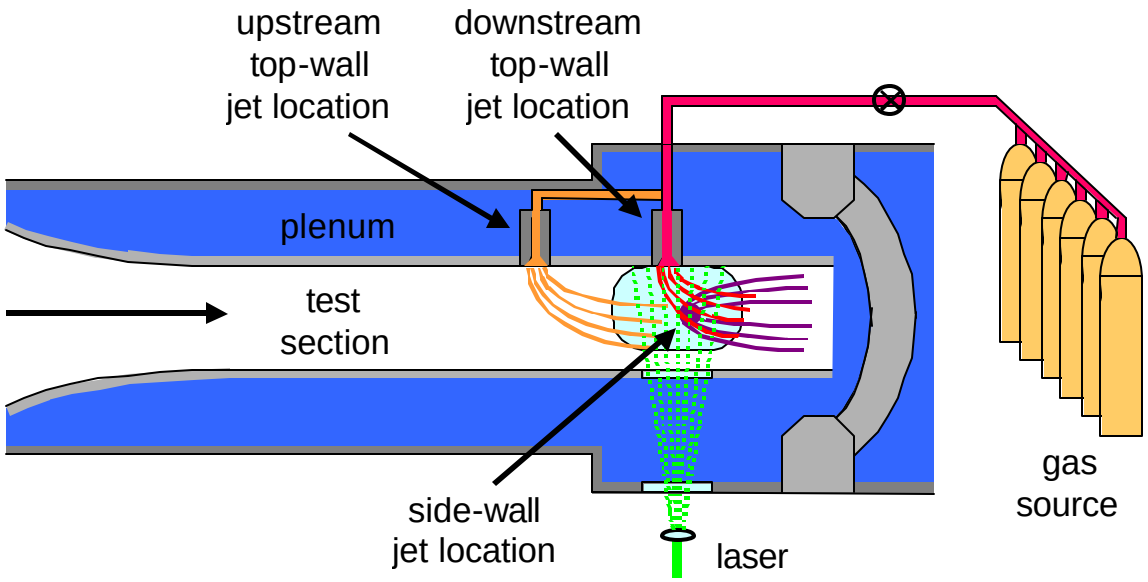

Figure 2: A sketch of the jet nozzle installation into the TWT, including three different mounting locations (two on the top wall and one on a side wall) to place the jet into different locations relative to the windows.

The gas source enters through the pipe fitting at the top of the settling chamber and one of the nozzles attaches at the bottom. Figure 1b shows the nozzle with the instrumented flat plate.

A schematic of the nozzle installation into the TWT is drawn in Figure 2. Three different locations for the jet are shown, as are the optical access and laser sheet used for measurements in aspects of this investigation that will be reported in future documents. Potential mounting positions are limited by the wind tunnel support structure behind the test section walls, so three different mounting locations have been chosen to provide varied alignment with the tunnel's windows and different instrumentation access. Figure 3 shows the jet apparatus mounted in its side-wall position by securing it in a window blank; it is visible from behind the test section in Figure 3a and inside the test section in Figure 3b. One advantage of this configuration is that it provides superior access to the myriad of pressure tubing and allows for an easier rotation of the nozzle to place the pressure taps into different angular positions with respect to the wind tunnel freestream. It also is easily viewed from the opposite window for surface flow visualizations. For proper alignment with the side-wall windows, the jet may be mounted into one of the two top-wall positions depending on whether the windows should be aligned with the near-field or the far-field of the jet interaction. Figure 4a shows a view that includes the jet hardware mounted above the test section in the downstream top-wall position, and Figure 4b shows the interior of the test section with the jet in the same location. The top-wall positions primarily are intended for studies employing optical diagnostics. The side-wall arrangement has been the primary configuration for the experiments reported in this document; a limited set of pressure measurements were acquired with the jet mounted in

(a)

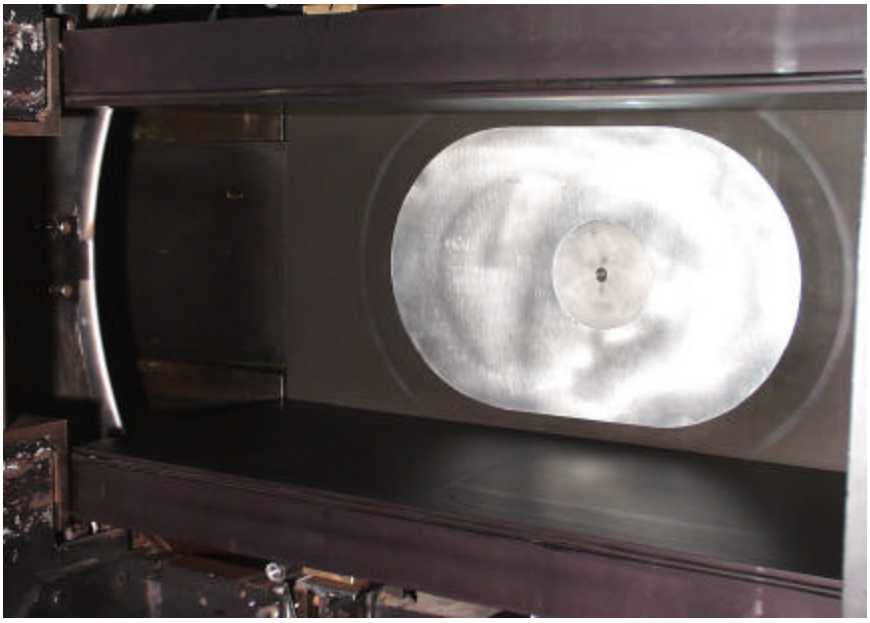

(b)

Figure 3: The jet nozzle hardware installed into the wind tunnel's side-wall mounting position; (a) seen from behind the tunnel wall; (b) seen from the front of the wind tunnel with an open test section. The coloration differences between wall plates in (b) are because some have not yet been anodized.

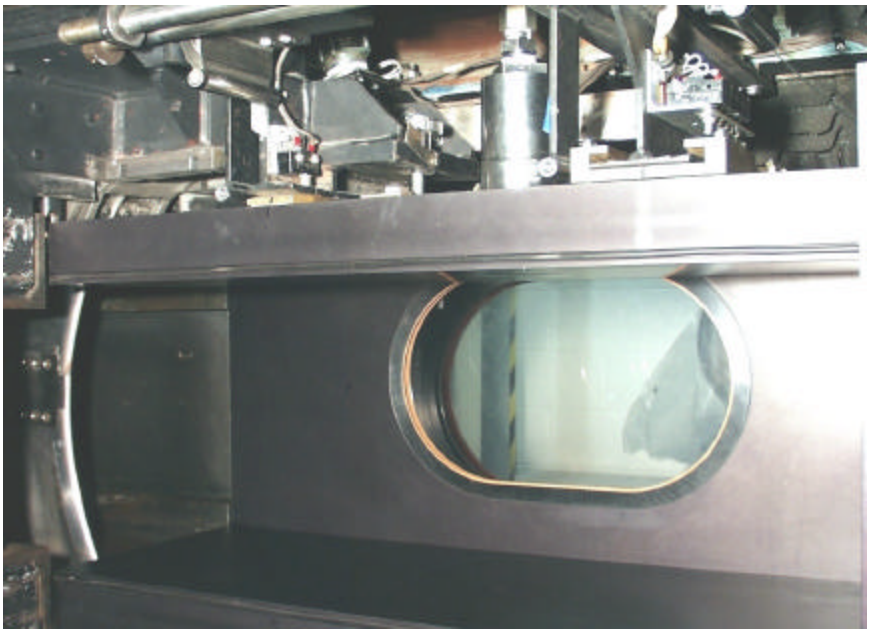

(a)

Figure 4: The jet nozzle hardware installed into the wind tunnel's top-wall mounting position. Both views are seen from the front of the wind tunnel with an open test section; (a) shows the wind tunnel support structure and the jet above the tunnel wall; (b) shows the interior top wall of the test section.

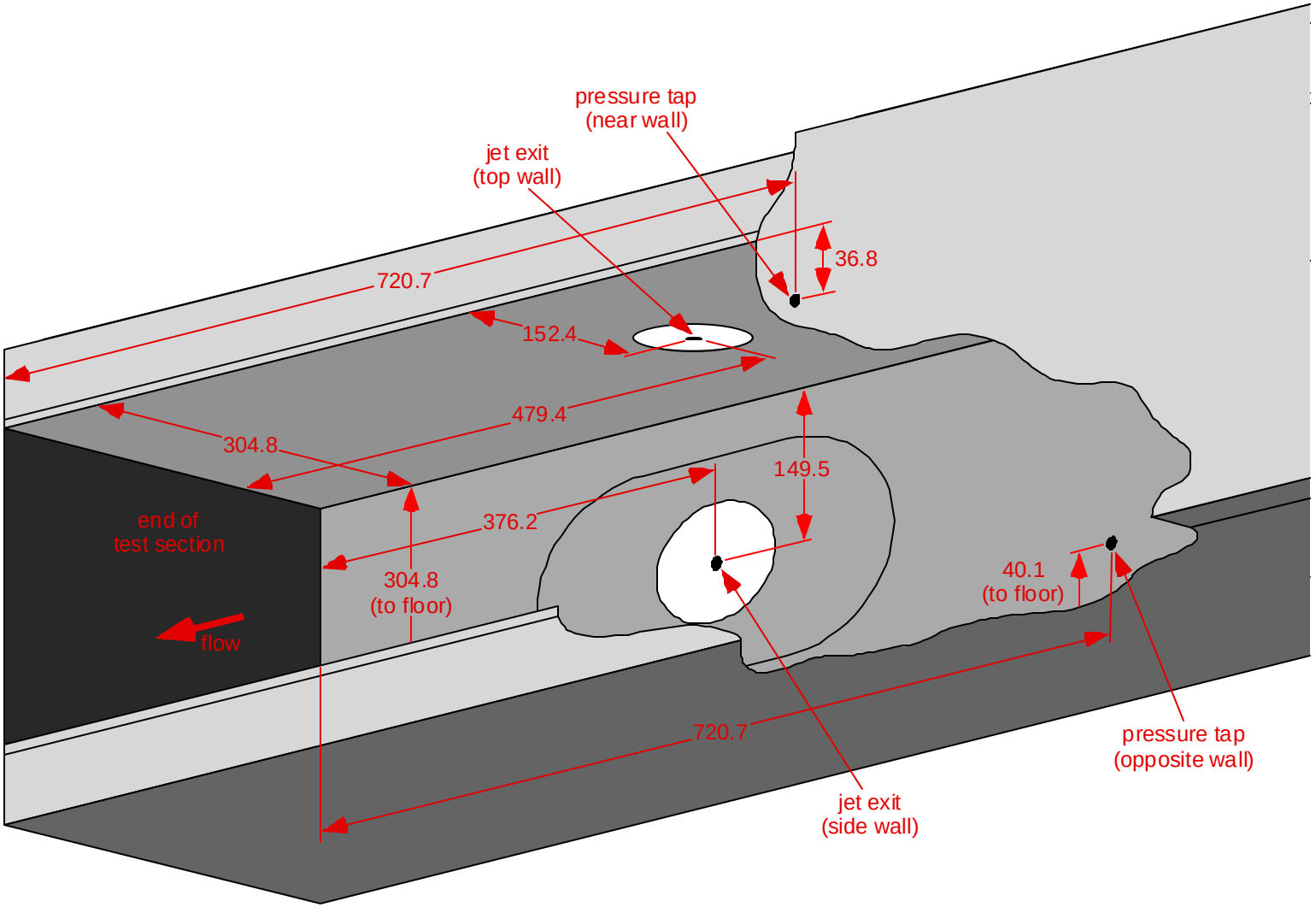
pressure tap
(near wall)
jet exit
(top wall)
36.8
720.7
152.4
479.4
304.8
149.5
376.2
end of
test section
304.8
(to floor)
flow
40.1
(to floor)
720.7
pressure tap
(opposite wall)
jet exit
(side wall)

18

the downstream location of the two top-wall mounting positions. These latter data were used to provide a comparison of the jet-in-crossflow emanating from the top wall as compared to the side wall.

A dimensioned schematic detailing the two jet locations employed in the present document is shown in Figure 5. When installed into the top-wall location, the jet was mounted, to within standard machining tolerances, on the wind tunnel centerline. However, when mounted in the side-wall position, it was slightly off-center as shown in Figure 5. This resulted from a variety of shimming and other adjustments that were required to fit the original test section into place when it was installed in 1983. These adjustments have become a permanent part of the TWT and positioning of the jet, though off-center, was highly repeatable. The test section maintains a constant cross-section for 466.8 mm upstream of the top-wall jet position, although the figure does not extend that far. At this point it interfaces with the curving walls of the sonic nozzle and the wind tunnel's contraction section. Similarly, the test section's cross-section is maintained for a downstream distance of 720.7 mm until it expands into the diffuser section of the wind tunnel. The interface with the diffuser section at this point resembles a backwards-facing step on each of the four walls. Detailed mechanical drawings of the wind tunnel, including the solid-wall test section and the contraction and diffuser sections, are available from the authors. Figure 5 also shows the location of two wall pressure transducers that will be discussed below.

A manifold of six nitrogen bottles pressurized to 24 MPa (3500 psi) provides the gas source for the nozzles, as seen in Figure 2. A dome-loaded regulator (Tescom 44-1300 series with ER3000 controller), remotely controlled from the wind tunnel control room, reduces the pressure to the desired stagnation condition. The hardware downstream of the regulator is designed to support a maximum pressure of 2000 psi with a flow rate of at least 900 cfm.

2.3 Instrumentation

2.3.1 Surface Pressure Measurements

As described above, two of the interchangeable nozzles are instrumented with pressure taps. Photographs are shown in Figure 6 and schematics are drawn in Figure 7. One nozzle is instrumented on the flat plate surface, as shown in Figures 6a and 7a. A ring of 24 taps surrounds the exit plane of the nozzle and two radial rows of taps 180° apart extend outward for a distance of approximately four jet diameters from the nozzle exit. One row has 25 taps and the other 26, with one of the rows offset with respect to the other by one-half a pressure tap spacing. Thus if the nozzle is rotated 180° and reinstalled, the pressure taps from one row will fill the gaps between tap locations in the previous configuration, effectively doubling the spatial resolution of the mean measurements. The nozzle is designed such that it can be installed into the test section at any chosen rotational angle. Repositioning the taps between wind tunnel runs produces a detailed mapping of the mean surface pressure field. A dial on the nozzle and an indicator mounted on the test section wall combine to permit accurate measurements of

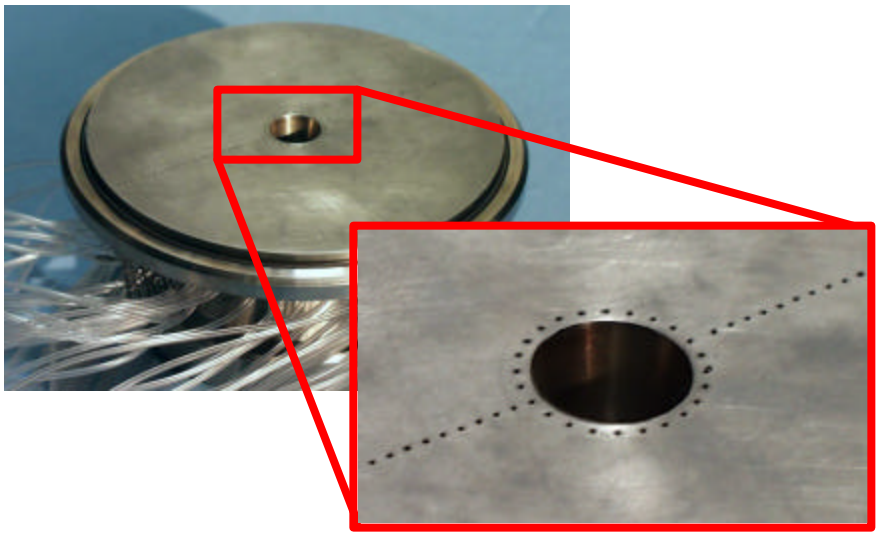

(a)

the radial position of the pressure taps. The diameter of all pressure taps is 0.51 mm (0.020 inch) and tap spacing is typically 1.57 mm (0.063 inch); different spacings are indicated

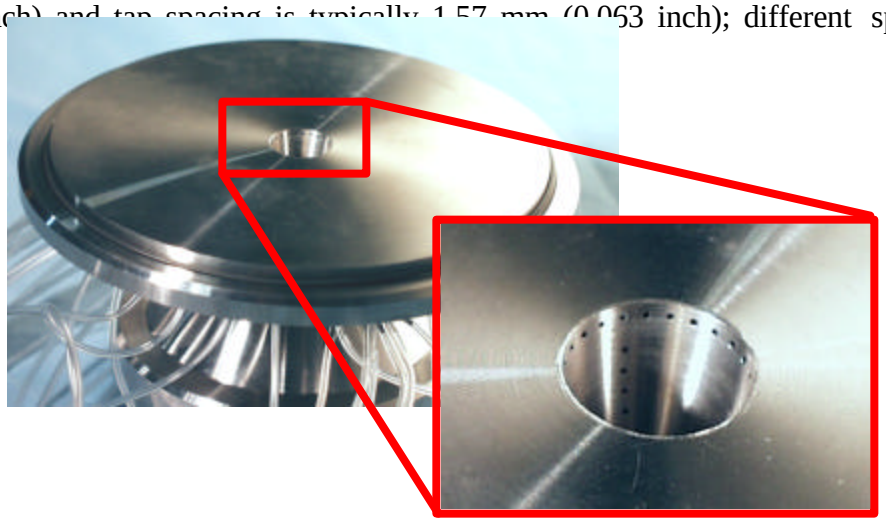

(b)

Figure 6: Pressure tap arrangements for each of the two instrumented nozzles; (a) instrumented flat plate; (b) instrumented within the nozzle.

The secon zle itself, as shown in Figu the nozzle depicted in Fig e exit plane of the nozzle a thirds of the way back tow vs are offset with respect to rotation of

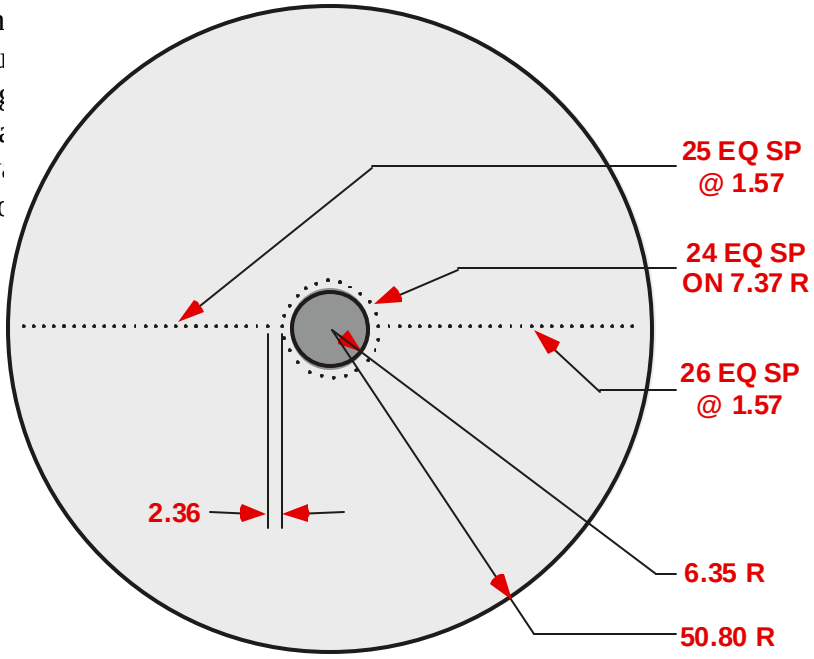

(a)

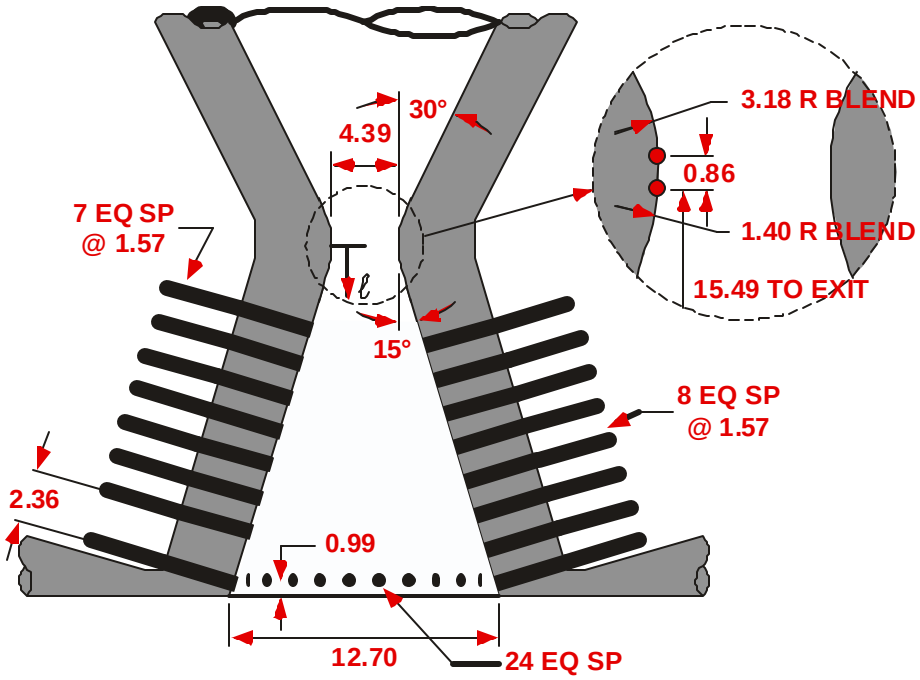

(b)

Figure 7: Pressure tap locations for each of the two instrumented nozzles; (a) instrumented flat plate; (b) instrumented within the nozzle. All dimensions are in millimeters and all taps are 0.51 mm in diameter. Critical nozzle dimensions also are given.

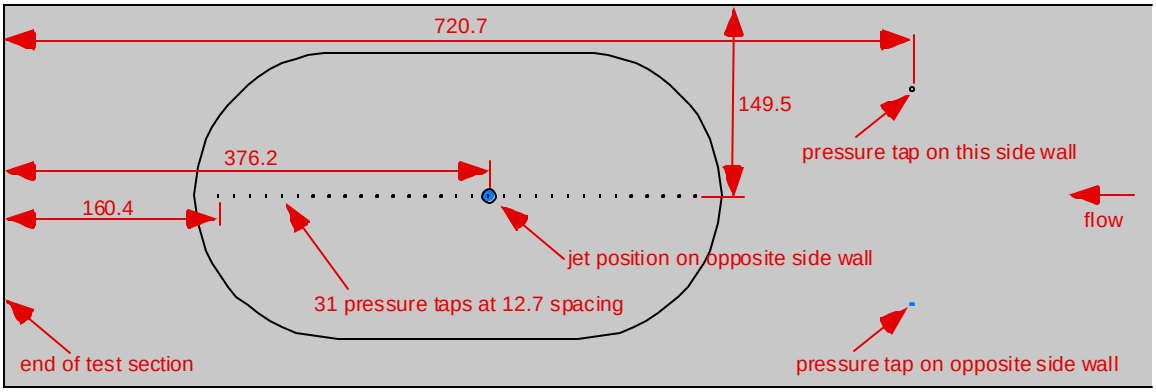

Figure 8: Location of the pressure taps in the instrumented window blank on the side wall opposite the jet's side-wall mounting position. The two upstream pressure taps shown in Figure 5 also are shown here. All dimensions are in millimeters and the sketch is not to scale.

the nozzle produces an effective doubling in the spatial resolution of the mean pressure field. The taps may be positioned at any chosen angle, which is again determined using a dial and indicator. Again, the tap diameter is 0.51 mm (0.020 inch) and the tap spacing is typically 1.57 mm (0.063 inch). Key nozzle dimensions also are marked in Figure 7b. Blend radii are used to maintain a smooth nozzle contour as the converging and diverging sections meet at the short cylindrical throat.

In addition to the two instrumented nozzles, the wind tunnel side wall opposite the jet's side-wall mounting point contained a row of pressure taps as drawn in Figure 8. The measurements from this instrumented window blank were used to determine the effect of the jet interaction on the wind tunnel's axial pressure distribution, which is particularly important for the solid-wall test section when operated near sonic conditions where choking could present an issue.

Pressure measurements were made using a Pressure Systems Inc. Model 8400 electronically scanned pressure system. The pressure taps from either of the two instrumented nozzles and the instrumented wind tunnel side wall were connected by tubing to pressure scanning modules (PSI ESP series) located behind the test section wall but within the TWT plenum. Electrical connections and control, calibration, and reference pressure lines passed through the plenum bulkhead to connect with the pressure control unit and the model 8400 system located in the wind tunnel control room. Both calibration and data acquisition were controlled using LabView on a Pentium-III-class personal computer. All measurements in the present study were made by a ±100 kPa (±15 psi) ESP module for the flat-plate-instrumented nozzle and a ±700 kPa (±100 psi) ESP module for the internally-instrumented nozzle, each with a manufacturer's quoted instrument uncertainty of 0.1% of full scale. However, this does not include additional noise sources from amplifiers and other electronics, so a more reasonable instrument uncertainty is 0.25% of full scale, or about ±0.5 kPa (±0.08 psi). These uncertainties are discussed fully in section 4.3.2 and 4.4.2 below. The ESP transducers were referenced to

atmospheric pressure, which was measured with a digital barometer (Druck DPI 140) with an accuracy of 0.01% of the reading.

Measurements from each pressure port were acquired simultaneous with measurements of the stagnation pressure and temperature of the wind tunnel, P_0 and T_0, as well as the jet settling chamber, P_{0j} and T_{0j}. P_0 was the average of values measured at two locations in the wind tunnel stagnation chamber using 700 kPa (100 psi) Statham pressure transducers and P_{0j} was measured using a single 15 MPa (2000 psi) Statham pressure transducer. The two P_0 measurements were not found to vary significantly from one another. The instrument uncertainty for each Statham transducer is quoted as 0.1% of full scale, but probably is more conservatively estimated as 0.25% of full scale when additional noise due to amplifiers and other electronics is considered. This produces a ±2 kPa (±0.3 psi) uncertainty for P_0 and a ±40 kPa (±5 psi) uncertainty for P_{0j}. T_0 was the average of two T-type thermocouples placed in the same location as the P_0 measurements and T_{0j} was measured by a single T-type thermocouple. Similarly to the P_0 measurements, the two values of T_0 were not found to possess significant discrepancies. The instrumentation uncertainty of the T_0 and T_{0j} measurements is estimated to be 2° C (4° F), including the thermocouple itself, its reference junction, and the amplifier. The static pressure in the test section p_w was measured from two wall pressures located upstream of the influence of the jet interaction as shown in Figures 5 and 8. These two pressures were measured by the ±100 kPa (±15 psi) PSI modules used for the interaction pressure measurements and hence have an uncertainty of about ±0.5 kPa (±0.08 psi). The nominal wind tunnel Mach number M_8 was determined assuming an isentropic expansion from the ratio of p_w and the tunnel stagnation pressure P_0. Since the test section possesses a constant cross-section, boundary layer growth will produce a gradually increasing M_8 so strictly speaking the quoted values of p_w and M_8 are valid only at the location of the p_w pressure taps sketched in Figures 5 and 8. For each wind tunnel run, 400 individual data points from each PSI pressure port were acquired simultaneous with measurements of P_0, T_0, p_w, P_{0j}, and T_{0j} at a rate of 100 Hz, then averaged to provide the mean data presented here.

All data measured on the flat plate and the instrumented window blank are presented as pressure coefficients, computed using the equation:

$$c_p = \frac{p - p_w}{\frac{1}{2}\gamma p_w M_\infty{}^2} \quad . \tag{1}$$

Since p_w and M_8 are determined at the upstream pair of wall pressure transducers, all values of c_p are therefore normalized to a point about 27 jet exit diameters upstream of the side-wall jet mounting location. The same data acquisition approach was used for data acquired within the nozzle, although the pressure ratio p/P_{0j} was calculated rather than c_p.

Some concerns must be addressed about the accuracy of the pressure measurements. Pressure lag in the tubing between the taps and the pressure scanners is not a concern for the mean measurements that are presently the focus of this investigation, particularly given the relatively large tap pressures.[37] The small size of the nozzle itself with respect to the pressure tap diameter may present a more subtle issue. If the diameter of the

pressure tap is a significant fraction of the boundary layer thickness of the flow passing over it, some measurement bias may result.[38-44] Adapting the analysis of Ducruet[44] to the present flowfield, it easily can be shown that no significant bias will occur for measurements made on the flat plate where wind tunnel wall length scales prevail. In contrast, measurements made within the nozzle are much more subject to this difficulty. The nozzle wall boundary layer thickness is substantially smaller with respect to the pressure tap diameter than the test section boundary layer thickness, which may lead to appreciable measurement biases. Additional effects due to wall curvature and large velocity gradients – both prominent features of nozzle flows – tend to aggravate the potential for such a bias. Estimating the magnitude of this bias is difficult because the available analyses do not fully apply to the present flowfield conditions. Nevertheless, extrapolating Ducruet's[44] work to the present case, it appears that the wall curvature and velocity gradient effects only contribute substantially to the bias for taps near the throat. The remaining bias due to the tap diameter is present throughout and may be no worse than +0.01 in terms of p/P_{0j}, but this estimate does not account for supersonic Mach number effects that could potentially alter the magnitude of the bias (although Flack's[43] work suggests that this is not the case). However, since the primary motivation for gathering measurements within the nozzle is to ascertain the presence of flow separation, these biases may not create a difficulty since separation is characterized by a distinct pressure rise regardless of whatever biases may be superimposed upon it. Thus while the pressure measurements themselves may experience a common bias, the determination of the separation point should remain reliable. Any comparison of the nozzle wall pressure values to those predicted by computations must account for the possible pressure hole biases. While +0.01 p/P_{0j} is a reasonable estimate of this error, it may in fact be larger, and this unknown must be respected in any validation activity. Because of the added biases near the throat, pressure magnitudes probably should only be used for the downstream half of the diverging section, that is, where $l/l_0=0.5$.

Just as the large size of the pressure taps with respect to the boundary layer thickness inside the nozzle may create an effect upon the measurements, the presence of the pressure taps themselves may create an effect upon the nozzle flowfield. Moulden et al.'s[41] study suggests that in the present geometry, the nozzle flow may experience a perturbation generated by the pressure taps. For this reason, a nozzle was fabricated without any pressure taps to generate an unperturbed flowfield, which was used for the surface flow tracer experiments to avoid any potential perturbations in the jet induced by the pressure taps.

2.3.2 Surface Flow Tracers

In addition to the surface pressure measurements that form a large component of the present work, surface flow tracers have been used to provide insight into the nature of the jet-in-crossflow flowfield. Such images do not provide for a quantitative validation of computational results, but do allow an approximate assessment of the model's ability to reproduce the gross flowfield features.

This study has used Zyglo ZL-60D, an oil-based fluorescent dye manufactured by Magnaflux. Zyglo is typically used as a penetrant for inspecting surfaces for cracks or flaws, but it also has proven effective for fluid mechanics experimentation. When illuminated using an ultraviolet light with a peak near 365 nm, the penetrant fluoresces in the green and can be viewed using virtually any standard camera. In the present case, images were photographed using a digital color camera peering through a high-pass cutoff filter to eliminate the illuminating light from the higher-wavelength fluorescing light. Images were acquired once the test section was opened following a tunnel run, because insufficient ultraviolet light could be directed through both the plenum and test section windows with the camera in place as well. Images were acquired rapidly after the conclusion of a tunnel run before the streamline features began to blur as the oil ran down the side wall; this was found not to be a problem unless an inordinate amount of time was consumed (approximately twenty minutes). It also was found that the fluorescent dye performed best during these experiments if it was allowed to dry for 20-30 minutes after application (but prior to a wind tunnel run) to increase its viscosity. The improved clarity of the surface flow images and the easy aerosol application of Zyglo were found to be preferential to the use of the more prevalent kerosene lampblack.

3 Experimental Conditions

The experimental conditions, like the jet design Mach number, have been selected to represent those found on transonic flight vehicles of interest that employ supersonic jets for attitude or roll control. The primary freestream Mach number was M_8=0.8 with a wind tunnel stagnation pressure P_0=154 kPa (22.4 psia), which at this Mach number yields a test section static pressure p_w=101 kPa (14.7 psia). The wind tunnel Reynolds number per unit length at these conditions is 20×10^6 m^{-1} (6×10^6 ft^{-1}). The nominal stagnation pressure for the Mach 3.73 jet was P_{0j}=4.96 MPa (720 psia). These conditions combine to produce a nominal jet-to-freestream dynamic pressure ratio of J=10.2. A primary group of seven additional sets of testing conditions also were employed to span a range of J values while maintaining a constant M_8=0.8, or to span a range of subsonic values of M_8 while maintaining a constant J=10.2. A few supplementary conditions were tested as well, in less depth, to ascertain particular trends or verify scaling laws; those data may be found in an earlier report concerning this investigation.[35] The choice of J and M_8 must keep within the subsonic restrictions imposed by the tunnel blockage issues inevitable with the solid-wall transonic test section.[35]

The eight primary experimental conditions, including the nominal case, are given in Table 1 for those experiments using the flat-plate-instrumented nozzle. Table 2 shows the equivalent information for the internally-instrumented nozzle and Table 3 provides the conditions for the surface oil flow tracers. While nominally the same, small differences in instrumentation and experimental technique, discussed more thoroughly below, contribute to the variation in the actual mean conditions. No precision uncertainties are provided for the oil flow tracer data because only one wind tunnel run was performed for each condition (except the nominal case, for which an uncertainty is provided). Case 4, which tested the lowest value of J, is not represented in the oil flow tracer data because this condition was added to the experiment subsequent to conducting the flow tracer measurements. Case 5 is not shown in the internally-instrumented data because no flow separation was observed for either case 1 or case 5, which makes case 5 identical to case 1 once the nozzle pressures are normalized. Each table shows the nominally selected value for each parameter, the mean value of the actual measured parameter over all wind tunnel runs for that condition, and the run-to-run precision uncertainty from those tunnel runs. The precision uncertainty represents with 95% confidence that the deviation of any one measurement from the given mean value will not exceed the given precision uncertainty. This is not the total measurement uncertainty because it does not include the effects of various potential biases; these will be discussed at length below.

In addition to those conditions detailed in Tables 1-3, experiments were also conducted without the jet mounted in the wind tunnel. These “tunnel empty” measurements consisted of wall pressure measurements along the two test section side walls and were used to get a baseline of the pressure distribution through the wind tunnel without any jet interaction effects. These data can be used to ensure that computational models are capable of simulating the simple wind tunnel flow alone before investigating

the complexity of the jet-in-crossflow interaction. The tunnel empty conditions are detailed in Table 4 and discussed in section 4.1 below.

In addition to the cases run with the jet exhausting from the wind tunnel side wall, a limited number of experiments were conducted with the jet exhausting from the top wall. The conditions for these measurements are given in Tables 5 and 6, where Table 5 shows the values acquired when using the flat-plate-instrumented nozzle and Table 6 shows the values using the internally-instrumented nozzle. No precision uncertainties are provided because fewer runs were conducted for these conditions. Case 5 was omitted from the internal measurements, as it was for the side-wall internal measurements listed in Table 2, because no separation is observed for this case and the normalized results are identical to case 1.

At the location on the wind tunnel side wall from which the jet exhausts, the 99%-velocity boundary layer thickness has been measured as 12.7 ± 0.5 mm (0.50 ± 0.02 inch) using a Pitot probe survey. At the top-wall jet mounting location, a similar Pitot probe survey showed the boundary layer thickness to be 11.5 ± 0.5 mm (0.45 ± 0.02 inch). The probes were inserted through the position of the jet exit centerline, but the probe tip was 77.5 mm (3.05 inch) long and hence the boundary layer thickness actually was measured this distance upstream of the jet locations given in Figure 5.

The Reynolds number of the nozzle flow based on the nozzle exit conditions and length of the nozzle diverging section is estimated as 7×10^6 for the nominal conditions. This is expected to be turbulent,[23] but may retain some degree of transitional character.

The presentation of the data in chapter 4 includes detailed discussions concerning the uncertainties of all the measurements, which includes numerous potential bias errors in addition to the repeatabilities given in Tables 1-3. These more complete uncertainties are summarized in Table 7 and are recommended for use in comparison with numerical simulations.

case	M_8			J			P_0 (kPa)			P_w (kPa)		
	nom	*act*	δ	*nom*	*act*	δ	*nom*	*act*	δ	*nom*	*act*	δ
1	0.8	0.797	0.002	10.2	10.23	0.06	154	154.4	0.7	101	101.5	0.4
2	0.8	0.795	0.002	8.4	8.58	0.06	154	154.3	0.4	101	101.8	0.3
3	0.8	0.800	0.002	5.6	5.67	0.05	154	154.2	0.5	101	101.2	0.3
4	0.8	0.802	0.002	2.8	2.84	0.05	154	154.3	0.6	101	101.0	0.3
5	0.8	0.793	0.002	16.9	16.96	0.16	154	154.4	0.5	101	102.0	0.3
6	0.7	0.702	0.002	10.2	10.19	0.08	141	140.6	0.5	101	101.2	0.4
7	0.6	0.603	0.001	10.2	10.12	0.05	130	129.5	0.4	101	101.3	0.4
8	0.5	0.506	0.001	10.2	10.04	0.11	121	120.7	0.7	101	101.3	0.6

case	P_{0j} (MPa)			T_0 (K)			T_{0j} (K)		
	nom	*act*	δ	*nom*	*act*	δ	*nom*	*act*	δ
1	5.00	4.99	0.02	320	319	6	295	291	4
2	4.14	4.17	0.02	320	320	8	295	291	6
3	2.76	2.78	0.02	320	319	8	295	294	6
4	1.38	1.39	0.02	320	319	8	295	295	5
5	8.27	8.22	0.06	320	319	6	295	288	4
6	3.83	3.84	0.02	320	319	10	295	290	5
7	2.83	2.82	0.01	320	318	9	295	292	5
8	1.93	1.97	0.02	320	317	8	295	294	6

Table 1: Summary of the eight testing conditions used for the flat-plate-instrumented experiments. Nominal (*nom*) and actual (*act*) conditions are shown along with the run-to-run precision uncertainties (δ) of the actual measurements. The first case is considered the nominal condition.

case	M_8			J			P_0 (kPa)			P_w (kPa)		
	nom	*act*	δ	*nom*	*act*	δ	*nom*	*act*	δ	*nom*	*act*	δ
1	0.8	0.796	0.002	10.2	10.21	0.07	154	154.3	0.5	101	101.6	0.2
2	0.8	0.793	0.002	8.4	8.61	0.06	154	154.2	0.4	101	101.9	0.2
3	0.8	0.799	0.002	5.6	5.67	0.07	154	154.3	0.6	101	101.4	0.3
4	0.8	0.800	0.002	2.8	2.81	0.05	154	154.3	0.5	101	101.2	0.3
5	0.8	n/a	n/a	16.9	n/a	n/a	154	n/a	n/a	101	n/a	n/a
6	0.7	0.700	0.002	10.2	10.19	0.13	141	140.6	0.6	101	101.4	0.4
7	0.6	0.602	0.001	10.2	10.10	0.09	130	129.5	0.4	101	101.4	0.3
8	0.5	0.505	0.001	10.2	10.08	0.11	121	120.1	0.4	101	100.9	0.3

case	P_{0j} (MPa)			T_0 (K)			T_{0j} (K)		
	nom	*act*	δ	*nom*	*act*	δ	*nom*	*act*	δ
1	5.00	4.98	0.02	320	316	8	295	293	5
2	4.14	4.17	0.02	320	314	8	295	293	3
3	2.76	2.77	0.03	320	315	7	295	294	4
4	1.38	1.38	0.02	320	315	5	295	295	4
5	8.27	n/a	n/a	320	n/a	n/a	295	n/a	n/a
6	3.83	3.83	0.02	320	314	7	295	292	5
7	2.83	2.81	0.02	320	314	5	295	295	5
8	1.93	1.97	0.02	320	314	4	295	295	4

Table 2: Summary of the eight testing conditions used for the internally-instrumented experiments. Nominal (*nom*) and actual (*act*) conditions are shown along with the run-to-run precision uncertainties (δ) of the actual measurements. The first case is considered the nominal condition. Case 5 was not run because the pressures inside the nozzle are identical to case 1 when appropriately normalized.

case	M_8			J			P_0 (kPa)			P_w (kPa)		
	nom	*act*	δ	*nom*	*act*	δ	*nom*	*act*	δ	*nom*	*act*	δ
1	0.8	0.807	0.002	10.2	10.08	0.11	154	155.9	0.3	101	101.5	0.1
2	0.8	0.808	n/a	8.4	8.37	n/a	154	155.1	n/a	101	100.9	n/a
3	0.8	0.817	n/a	5.6	5.63	n/a	154	155.0	n/a	101	99.9	n/a
4	0.8	n/a	n/a	2.8	n/a	n/a	154	n/a	n/a	101	n/a	n/a
5	0.8	0.798	n/a	16.9	16.81	n/a	154	155.1	n/a	101	102.0	n/a
6	0.7	0.716	n/a	10.2	10.02	n/a	141	141.4	n/a	101	100.6	n/a
7	0.6	0.607	n/a	10.2	10.08	n/a	130	130.8	n/a	101	102.0	n/a
8	0.5	0.516	n/a	10.2	10.14	n/a	121	120.7	n/a	101	100.6	n/a

case	P_{0j} (MPa)			T_0 (K)			T_{0j} (K)		
	nom	*act*	δ	*nom*	*act*	δ	*nom*	*act*	δ
1	5.00	5.04	0.03	320	329	4	295	288	2
2	4.14	4.17	n/a	320	322	n/a	295	288	n/a
3	2.76	2.84	n/a	320	325	n/a	295	294	n/a
4	1.38	n/a	n/a	320	n/a	n/a	295	n/a	n/a
5	8.27	8.25	n/a	320	323	n/a	295	284	n/a
6	3.83	3.90	n/a	320	326	n/a	295	293	n/a
7	2.83	2.87	n/a	320	324	n/a	295	290	n/a
8	1.93	2.06	n/a	320	324	n/a	295	292	n/a

Table 3: Summary of the eight testing conditions used for the surface oil flow tracer experiments. Nominal (*nom*) and actual (*act*) conditions are shown; run-to-run precision uncertainties (δ) are omitted except for case 1 because this was the only case that was repeated. Case 4 was not performed. The first case is considered the nominal condition.

case	M_8			P_0 (kPa)			P_w (kPa)			T_0 (K)		
	nom	*act*	δ	*nom*	*act*	δ	*nom*	*act*	δ	*nom*	*act*	δ
1	0.8	0.801	0.003	154	153.1	0.9	101	100.3	0.6	320	320	6
2	0.8	0.801	n/a	154	111.6	n/a	101	73.2	n/a	320	319	n/a
3	0.8	0.801	n/a	154	127.3	n/a	101	83.4	n/a	320	320	n/a
4	0.8	0.801	n/a	154	214.0	n/a	101	140.2	n/a	320	320	n/a
6	0.7	0.704	n/a	141	138.6	n/a	101	99.6	n/a	320	318	n/a
7	0.6	0.600	n/a	130	128.2	n/a	101	100.5	n/a	320	316	n/a
8	0.5	0.500	n/a	121	118.7	n/a	101	99.4	n/a	320	318	n/a

Table 4: Summary of the testing conditions used for the "tunnel empty" pressure measurements. Nominal (*nom*) and actual (*act*) conditions are shown; run-to-run precision uncertainties (δ) are given only for case 1 because this was the only case that was repeated. The first case is considered the nominal condition.

case	M_8			J			P_0 (kPa)			P_w (kPa)		
	nom	*act*	δ	*nom*	*act*	δ	*nom*	*act*	δ	*nom*	*act*	δ
1	0.8	0.795	n/a	10.2	10.34	n/a	154	154.5	n/a	101	101.9	n/a
2	0.8	0.792	n/a	8.4	8.76	n/a	154	153.9	n/a	101	101.8	n/a
3	0.8	0.799	n/a	5.6	5.75	n/a	154	154.6	n/a	101	101.6	n/a
4	0.8	0.801	n/a	2.8	2.88	n/a	154	154.5	n/a	101	101.2	n/a
5	0.8	0.790	n/a	16.9	17.07	n/a	154	154.6	n/a	101	102.5	n/a
6	0.7	0.701	n/a	10.2	10.29	n/a	141	140.8	n/a	101	101.4	n/a
7	0.6	0.602	n/a	10.2	10.20	n/a	130	129.4	n/a	101	101.3	n/a
8	0.5	0.506	n/a	10.2	10.20	n/a	121	120.1	n/a	101	100.9	n/a

case	P_{0j} (MPa)			T_0 (K)			T_{0j} (K)		
	nom	*act*	δ	*nom*	*act*	δ	*nom*	*act*	δ
1	5.00	5.03	n/a	320	312	n/a	295	289	n/a
2	4.14	4.23	n/a	320	308	n/a	295	288	n/a
3	2.76	2.82	n/a	320	311	n/a	295	290	n/a
4	1.38	1.41	n/a	320	313	n/a	295	295	n/a
5	8.27	8.26	n/a	320	312	n/a	295	290	n/a
6	3.83	3.88	n/a	320	311	n/a	295	289	n/a
7	2.83	2.83	n/a	320	311	n/a	295	291	n/a
8	1.93	1.99	n/a	320	311	n/a	295	293	n/a

Table 5: Summary of the eight testing conditions used for the experiments conducted on the wind tunnel top wall using the flat-plate-instrumented nozzle. Nominal (*nom*) and actual (*act*) conditions are shown. Run-to-run precision uncertainties (δ) are omitted because few tunnel runs were conducted. The first case is considered the nominal condition.

case	M_8			J			P_0 (kPa)			P_w (kPa)		
	nom	*act*	δ	*nom*	*act*	δ	*nom*	*act*	δ	*nom*	*act*	δ
1	0.8	0.794	n/a	10.2	10.34	n/a	154	154.2	n/a	101	101.8	n/a
2	0.8	0.792	n/a	8.4	8.64	n/a	154	154.2	n/a	101	101.9	n/a
3	0.8	0.797	n/a	5.6	5.77	n/a	154	154.1	n/a	101	101.3	n/a
4	0.8	0.800	n/a	2.8	2.90	n/a	154	154.1	n/a	101	101.1	n/a
5	0.8	n/a	n/a	16.9	n/a	n/a	154	n/a	n/a	101	n/a	n/a
6	0.7	0.699	n/a	10.2	10.34	n/a	141	140.4	n/a	101	101.2	n/a
7	0.6	0.602	n/a	10.2	10.26	n/a	130	129.6	n/a	101	101.5	n/a
8	0.5	0.505	n/a	10.2	10.09	n/a	121	120.0	n/a	101	100.8	n/a

case	P_{0j} (MPa)			T_0 (K)			T_{0j} (K)		
	nom	*act*	δ	*nom*	*act*	δ	*nom*	*act*	δ
1	5.00	5.02	n/a	320	306	n/a	295	296	n/a
2	4.14	4.18	n/a	320	308	n/a	295	295	n/a
3	2.76	2.81	n/a	320	307	n/a	295	294	n/a
4	1.38	1.42	n/a	320	307	n/a	295	296	n/a
5	8.27	n/a	n/a	320	n/a	n/a	295	n/a	n/a
6	3.83	3.87	n/a	320	306	n/a	295	295	n/a
7	2.83	2.85	n/a	320	306	n/a	295	296	n/a
8	1.93	1.96	n/a	320	306	n/a	295	297	n/a

Table 6: Summary of the eight testing conditions used for the experiments conducted on the wind tunnel top wall using the internally-instrumented nozzle. Nominal (*nom*) and actual (*act*) conditions are shown. Run-to-run precision uncertainties (δ) are omitted because few tunnel runs were conducted. The first case is considered the nominal condition. Case 5 was not run because the pressures inside the nozzle are identical to case 1 when appropriately normalized.

variable	uncertainty
P_0	±2 kPa (±0.3 psi)
T_0	2° C (4° F)
P_{0j}	±40 kPa (±5 psi)
T_{0j}	2° C (4° F)
p_w	±0.5 kPa (±0.08 psi)
c_p (tunnel empty)	±0.02
c_p (flat plate)	±0.04
p/P_{0j} (nozzle wall)	±0.014
l_{sep}/l_0	varies based on l

Table 7: Recommended uncertainties for use in comparison with numerical simulations.

4 Results and Discussion

4.1 Tunnel Empty

Wall pressure measurements were conducted in an empty wind tunnel (that is, the jet was removed and replaced with a wall blank) using the instrumented window blank and the two independent wall pressure taps upstream of it (which provide p_w). This was intended both to supply a baseline of the pressure distribution through the solid-wall test section without any interference from the jet interaction and to provide a computationally simple case from which modeling constants can be calibrated.

Measurements were conducted at wind tunnel conditions similar to those described in section 3.0, except that, obviously, the jet was not present to allow any variation of P_{0j} or J. The nominal flow conditions were M_8=0.8 with P_0=154 kPa (22.4 psia), producing p_w=101 kPa (14.7 psia), and additional runs were conducted at lower Mach numbers for the same p_w, plus a few runs at M_8=0.8 but different values of p_w to assess any possible Reynolds number effects. The experimental conditions for the tunnel empty cases are given in Table 4; run-to-run variations were available only for the nominal case.

The resulting pressure coefficients along the instrumented window blank are shown in Figure 9 for the nominal flow conditions (case 1 in Table 4); the given data is the mean of several independent wind tunnel runs. Also shown is a trace of the increasing wall Mach number as inferred from these pressures, caused by the growth of the boundary layer through the constant area test section. The values of c_p remain negative throughout because they are referenced to p_w, which is measured upstream of the instrumented window blank where the static pressure is slightly larger than it is upon the instrumented window blank; for the same reason, all values of M are larger than M_8. The repeatability of the c_p trace is ±0.003, which is less than the thickness of the lines displayed in Figure 9. This run-to-run precision uncertainty is the 95% confidence interval that any one given measurement lies within this distance of the mean, which is found as approximately twice the standard deviation of several independent wind tunnel runs, where the actual multiplier is somewhat larger than 2, as determined by Student's t-distribution. Vertical dashed lines represent the location of the nozzle exit if it had been present. Small undulations are visible in both traces, which are more likely to have resulted from some sort of measurement bias between taps than from actual flowfield conditions; the uncertainty created by these undulations is assessed by the flowfield nonuniformity investigation described below.

Measurements of c_p conducted for differing values of P_0 (ranging from 112 kPa to 214 kPa, or 16.2 psia to 31.0 psia), and hence different wind tunnel Reynolds numbers, while M_8 remained constant at 0.8 did not produce results appreciably different from the nominal conditions shown in Figure 9. Two standard deviations of these variations in c_p due to P_0 variations was no more than ±0.004, which is not meaningfully larger than the repeatability of ±0.003. The resulting pressure traces are not shown since they appear identical to the one displayed in Figure 9. Additional wind tunnel runs were conducted at lower Mach numbers and the resulting c_p curves are shown in Figure 10. The pressure

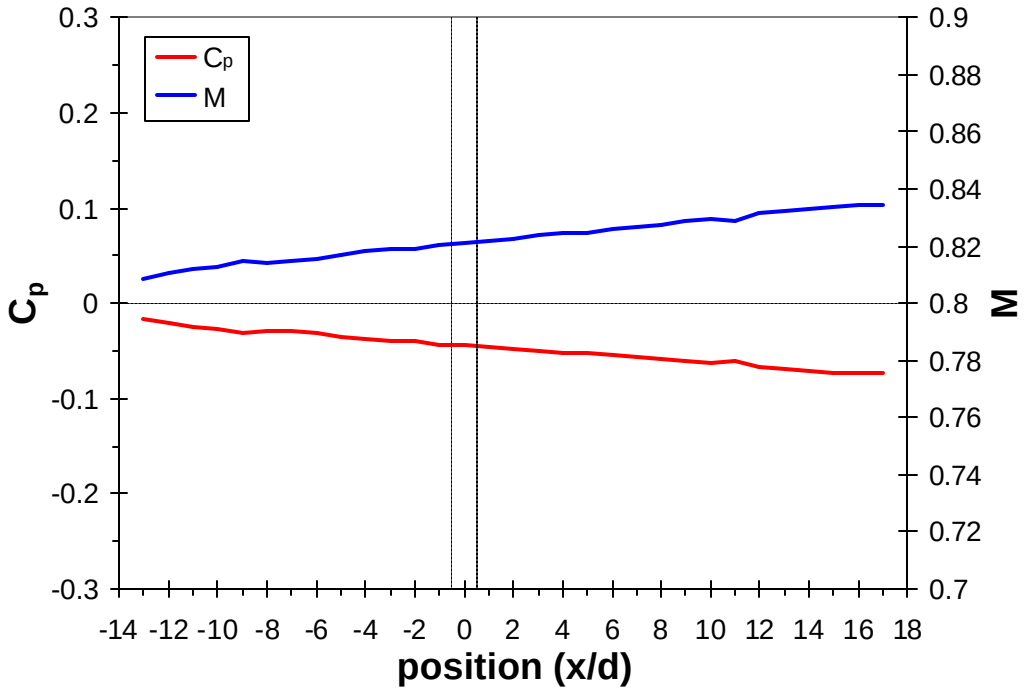

Figure 9: Surface pressures measured by the instrumented window blank for tunnel empty conditions at M_8=0.8 and p_w=101 kPa. The inferred wall Mach number also is shown. The jet, if present, would have been located at x=0.

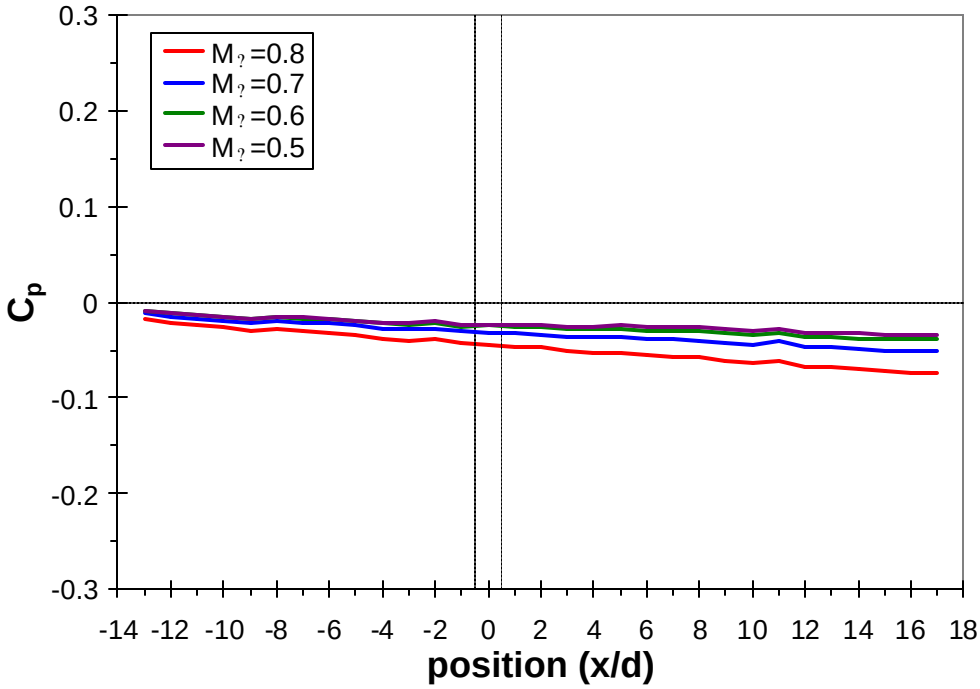

Figure 10: Surface pressures measured by the instrumented window blank for tunnel empty conditions at different freestream Mach numbers and p_w=101 kPa. The jet, if present, would have been located at x=0.

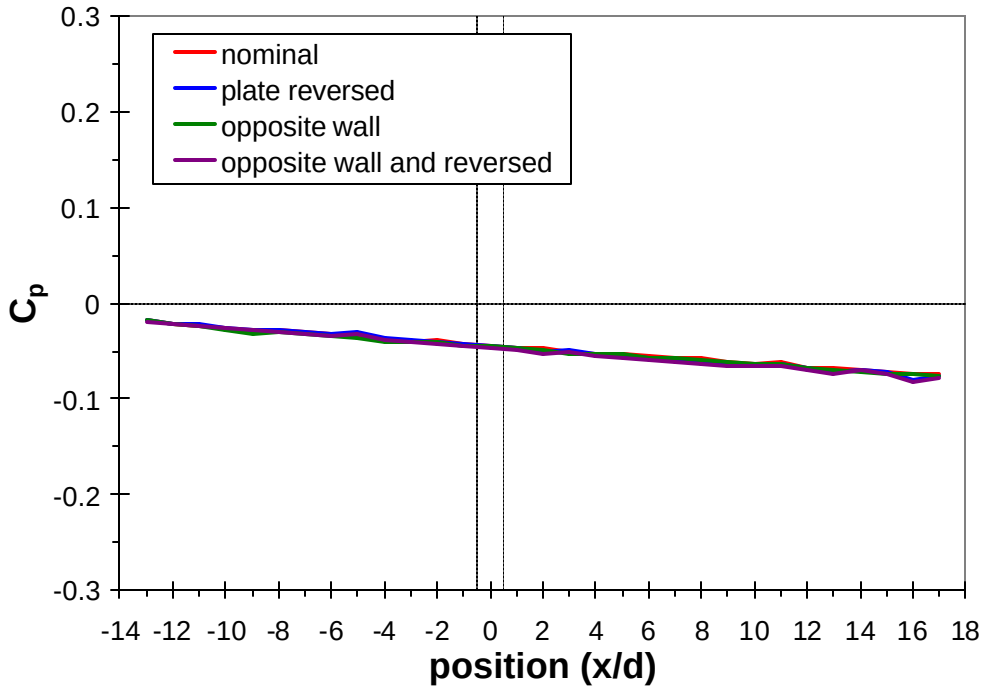

Figure 11: Surface pressures measured when relocating the instrumented window blank into positions of geometric similarity for M_8=0.8 and p_w=101 kPa.

drops less through the test section for lower M_8, which is consistent with a thinner boundary layer for smaller Mach numbers. It also is evident in the figure that the small undulations in the pressure traces are consistent between different Mach numbers, which suggests that they are not related to pressure waves in the solid-wall test section but rather are created by small imperfections in the wall plate, burrs in the pressure taps, leaks in the pressure lines, or transducer biases. Nevertheless, these ripples are small in magnitude, representing only about ±0.002 c_p.

In an effort to investigate concerns regarding any potential flowfield asymmetry, the instrumented window blank was moved into different positions within the test section that nominally are geometrically symmetric. This should help reveal any nonuniformities in the pressure field created either by the flow through the test section, the machining or installation of the pressure taps in the window blank, or biases in the pressure transducers. The window blank was first rotated 180° and mounted back in position, which places the pressure taps into the same locations as in the original configuration but in reverse order. The resulting pressure trace is shown in Figure 11. It is evident that the pressures measured in this position are not significantly different from those in the unrotated position; all but two of the data points lie within the ±0.003 c_p repeatability of the measurements and those two outliers are no more than ±0.004 c_p from the unrotated case. The window blank was then moved to the opposite side wall of the wind tunnel and measurements were taken there with the plate in both the 0° and 180° positions. Those pressure traces also are displayed in Figure 11, and again, no discernable difference is seen with respect to the nominal case. The measurements on the opposite wall at 0° lie within ±0.002 c_p and those at 180° lie within ±0.005 c_p, suggesting that the effects of

rotating the plate are greater than those of moving it to the opposite side of the test section. However, in no case is the effect meaningfully large and this procedure has detected no substantial nonuniformity in the test section when operated in "tunnel empty" mode.

Since the tunnel nonuniformity as measured by the pressure taps has been found to be small, and since the repeatability of the measurements is equally small, the primary contributor to measurement uncertainty for the tunnel empty case is the instrumentation error. As discussed in section 2.3.1, this error source is 0.5 kPa (0.08 psi), which translates to ± 0.02 c_p and is the total estimated uncertainty for tunnel empty wall pressure measurements.

The absence of any detectable nonuniformity in the test section flow is consistent with the wall pressure measurements made using the two upstream pressure taps shown in Figure 5, which did not show any appreciable difference between them. The difference between these two pressure taps was typically 0.07-0.15 kPa (0.01-0.02 psi), which is less than the approximately 0.5 kPa (0.08 psi) instrument uncertainty of the pressure transducers. These observations suggest that the axial location of the measured value of p_w is the only important parameter in locating the position of this measurement; its lateral distance from the wind tunnel centerline is insignificant. Strictly speaking, however, the tunnel nonuniformity pressure measurements have shown only that the tunnel is symmetric from one side wall to the other and even then only on the centerplane of the test section. The consistency of the two upstream pressure taps indicates no vertical nonuniformity at this position in the test section, which is most relevant to treatment of values of p_w. While these results are reassuring, it would be a premature extrapolation to declare that no tunnel asymmetry exists in the pressure field.

4.2 Surface Flow Tracers

The Zyglo fluorescent oil flow tracer was used to provide flow visualization of the gross surface flowfield features of the jet-in-crossflow interaction. While the resulting images are purely qualitative and subject to interpretation, they do highlight the primary features found on the flat plate surface and can be compared with those generated by computational efforts. While such a comparison clearly is not a numerical validation of the code's results, it does provide a qualitative assessment for their veracity by establishing that the simulation can accurately capture the gross flowfield features of the interaction. Figure 12 sketches the common features of jet-in-crossflow interactions, some of which should be detectable by the surface flow tracers. Both the horseshoe vortices and the wake vortices are expected to be evident. While the jet trajectory and spreading will have an influence on the oil flow patterns, the jet's counter-rotating vortex pair will not be directly observable.

Oil flow tracers were employed only on the flat plate surface of the jet-in-crossflow interaction. Although the use of this technique within the nozzle would have been interesting as a means of locating the separation line, this was found to be impractical for the present experiment. Useful images could not be photographed within the small

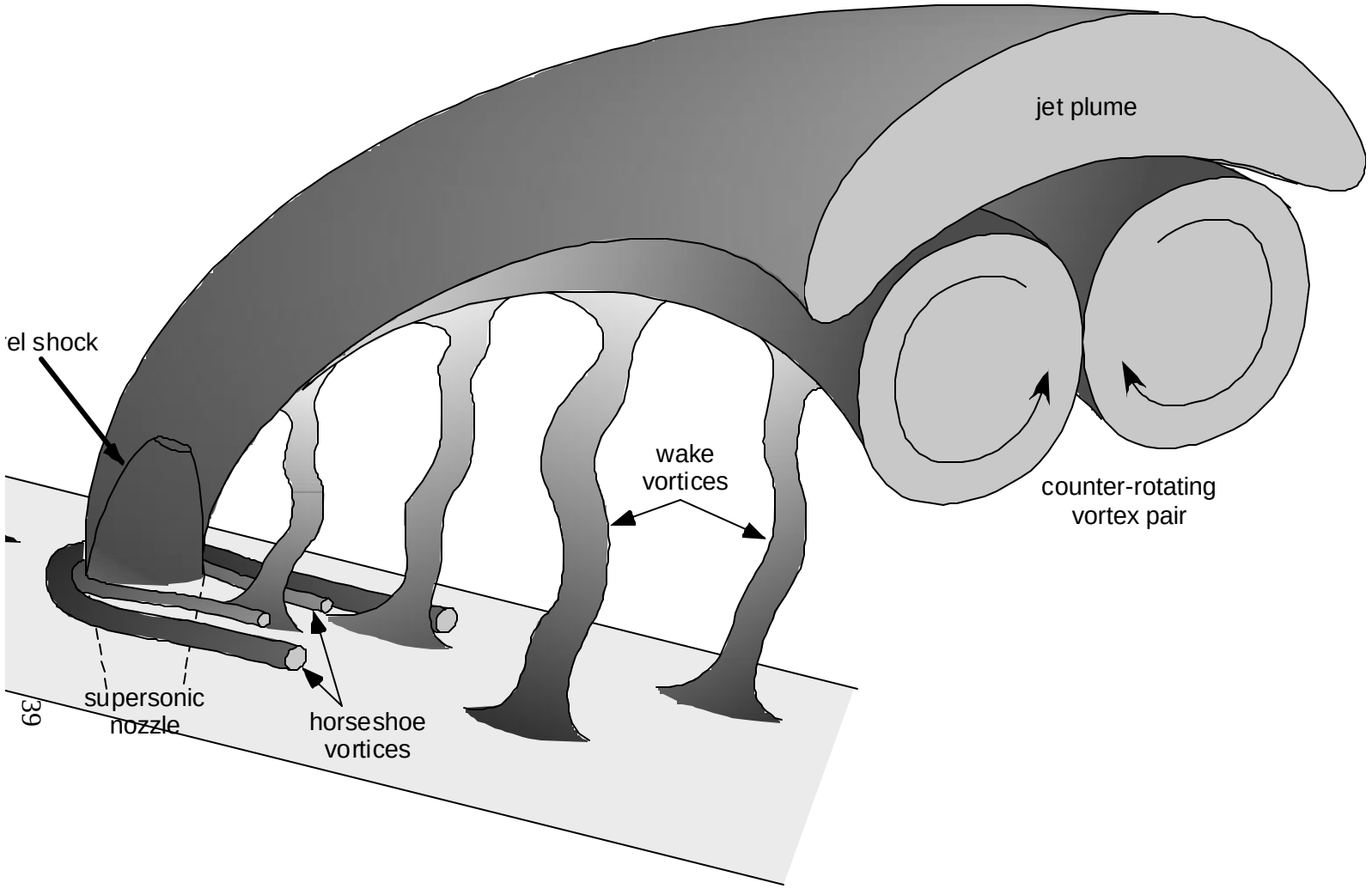
jet plume
el shock
wake
vortices
counter-rotating
vortex pair
supersonic
nozzle
horseshoe
vortices

confines of the nozzle, and furthermore, the oil seemed more prone to running along the inside nozzle walls following a wind tunnel run than on the flat plate. Thus no flow visualization was accomplished inside the nozzle.

Figure 13 displays the surface flow features as highlighted by the Zyglo fluorescent oil tracer. Images are presented for seven of the eight sets of flowfield conditions as detailed in Table 4. Since the jet exit diameter is 12.7 mm (0.500 inch), this feature can be used as a dimensional scale in each image. The general appearance of Figure 13a, for which the flow conditions most closely agree with those of Chocinski et al.,[1] qualitatively matches their oil flow tracers, lending confidence that the technique is highlighting appropriate fluid mechanics features. Repeat runs were conducted only for those conditions displayed in Figure 13a; the flow structure revealed by the measurement technique was nearly identical for the repeated images, with differences restricted to artifacts resulting from a variance in the initial concentration of oil.

Although flowfield structures are distinctly visualized, these images must be interpreted cautiously, as some effects are products of the diagnostic technique. This includes the large disk that dominates all seven images, which results from the use of different materials for the nozzle hardware and the window blank into which it mounts. Large build-ups of fluorescent oil prior to a wind tunnel run, such as within the crevice between the nozzle insert and the tunnel wall, are prone to create conspicuous bright streaks in regions of the images that have no connection to the fluid dynamics of the jet-in-crossflow. A prominent example is obvious in Figure 13c. Some buildup of oil near the downstream edge of the jet insert disk also is observed in the images, which is likely to represent another artifact of the visualization technique. Scratches seen in the wake of the jet where it lies outside the nozzle insert disk are remnants of the machining process; they do not represent anything of significance and in fact are well within the surface smoothness tolerances of the part.

Some general features can be observed for all seven images spanning the range of M_8 and J. The dark region wrapping around the jet is a horseshoe vortex created by flow separation and its reattachment line is visualized by the distinct line seen in the near-wake of the jet. The brighter region wrapping around this horseshoe vortex is believed to be a second horseshoe vortex; these dual horseshoe vortices have been observed in incompressible jets in crossflow.[45-48] The horseshoe vortices are observed to increase in size as either J rises or M_8 is increased, although they are sufficiently small at $M_8=0.5$ that they are scarcely notable. The dark wedge behind the jet indicates the extent of its wake. Visualization of the wake appears to be reliable on the nozzle disk, but may not be upon the window blank into which it mounts. As the wake extends over this junction, its clarity is noticeably diminished due to oil becoming disturbed by the flowlines created at this mechanical intersection. The two parts were mated together to excellent tolerances, producing a flush surface and a small crevice, but apparently the oil flow is sufficiently sensitive to respond to these small features. The problem is particularly evident at either low M_8 or J. Nevertheless, the initial extent of the wake where it remains on the nozzle disk (and where the pressure drop would be strongest) does not appear to suffer from such an influence.

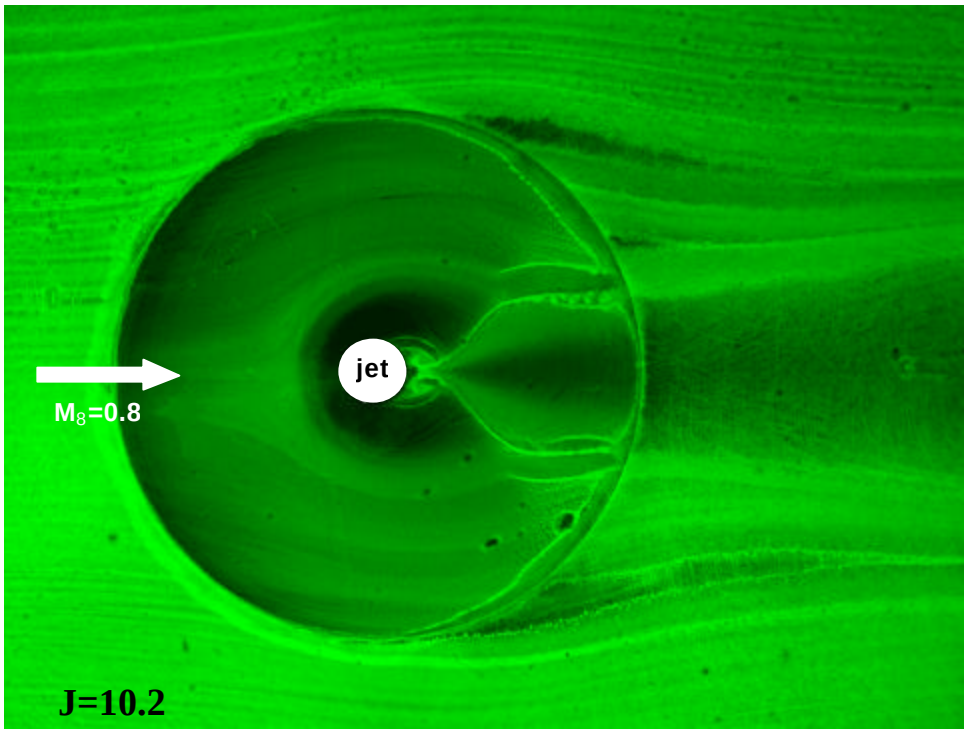

(a)

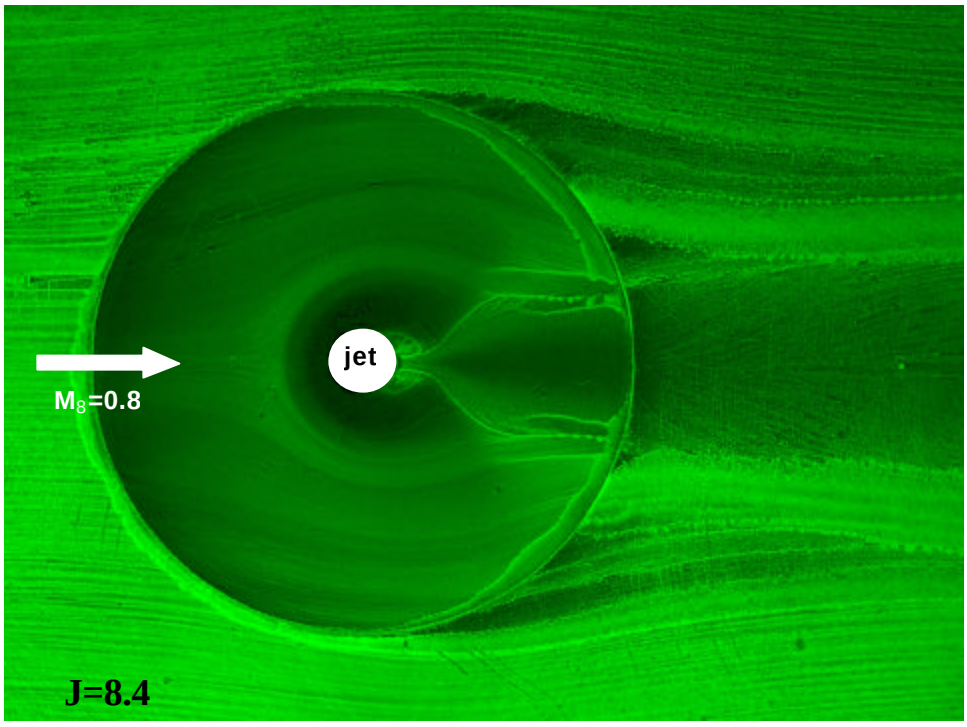

(b)

Figure 13: Images of the surface flow features as highlighted by a fluorescent oil tracer. Data is presented at seven different flowfield conditions as indicated in (a) through (g). (continued on the following pages)

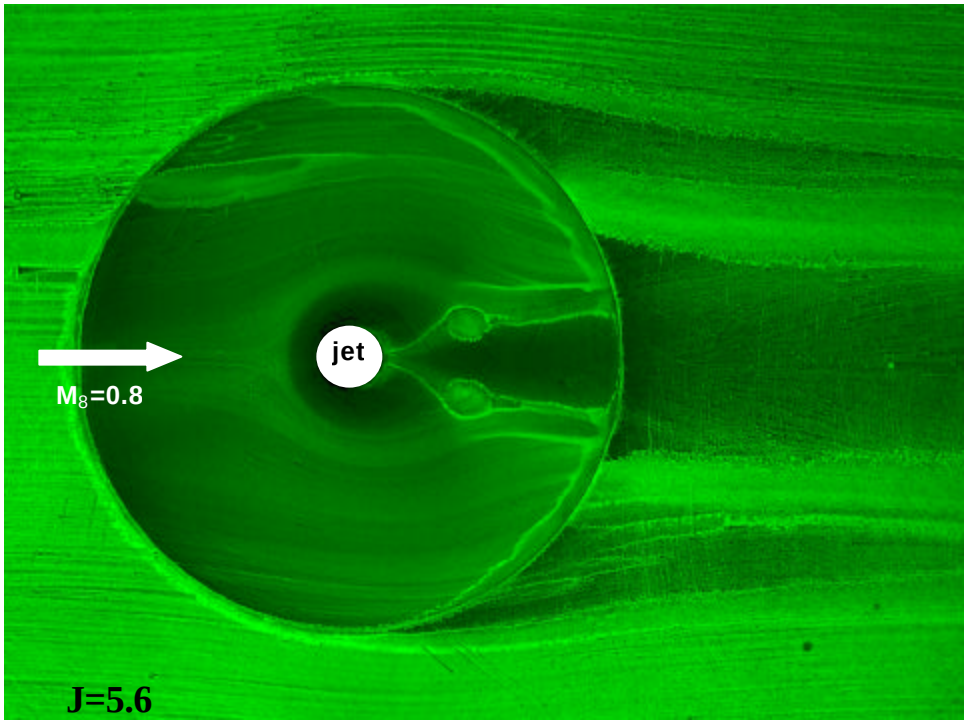

(c)

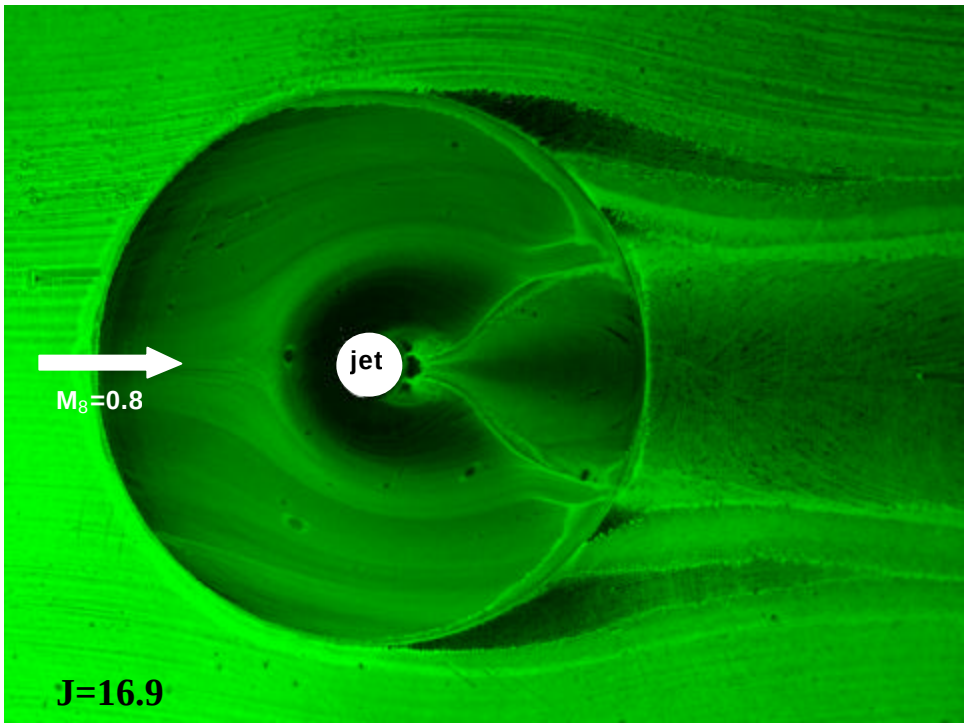

(d)

Figure 13, continued

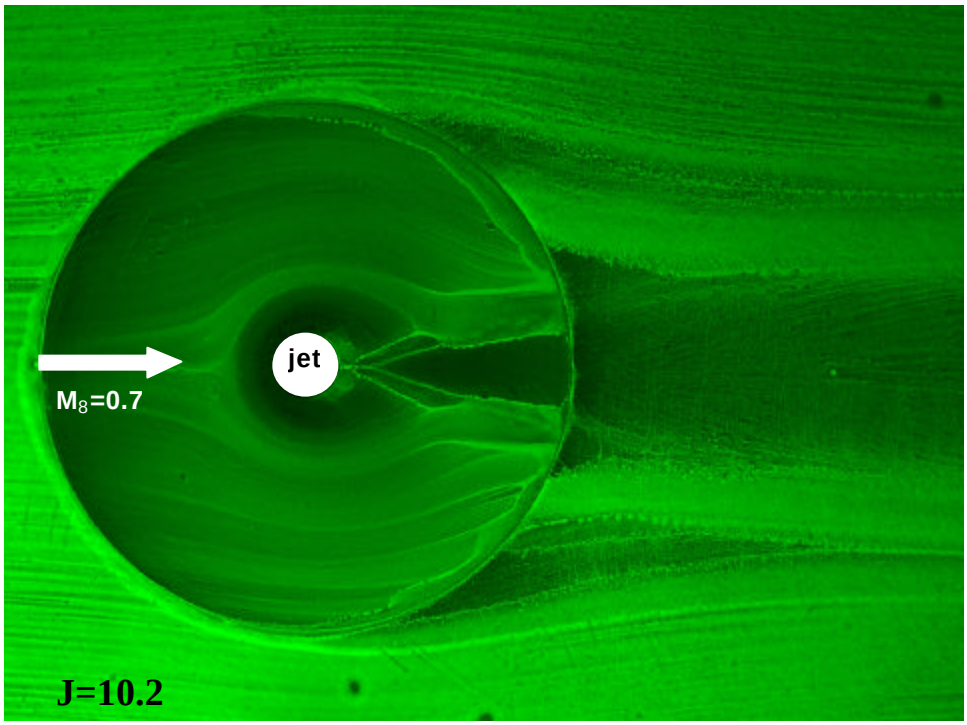

(e)

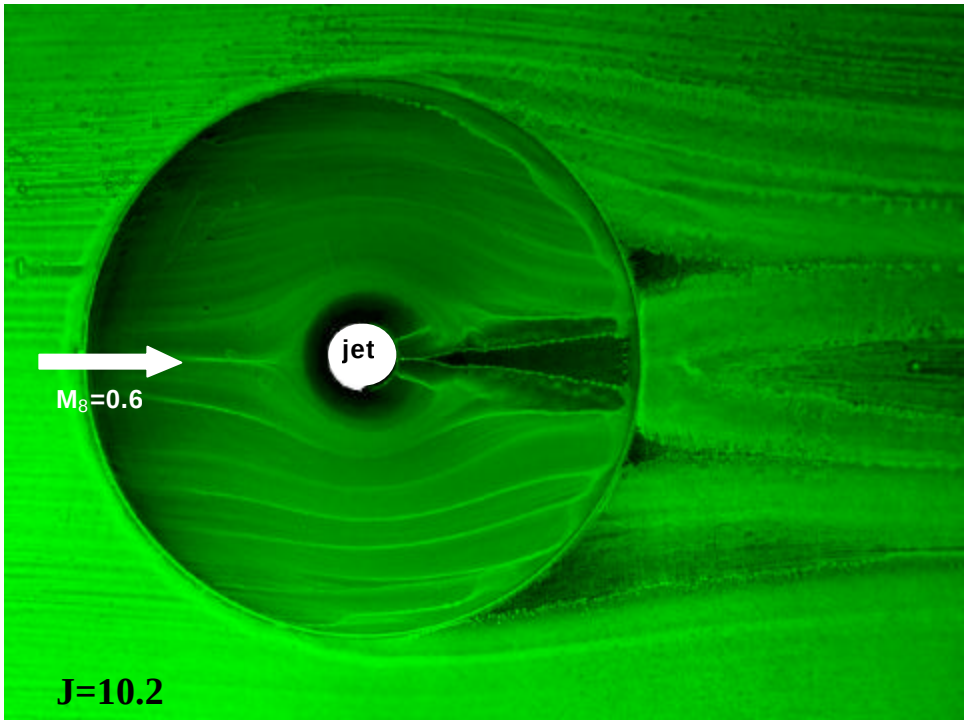

(f)

Figure 13, continued

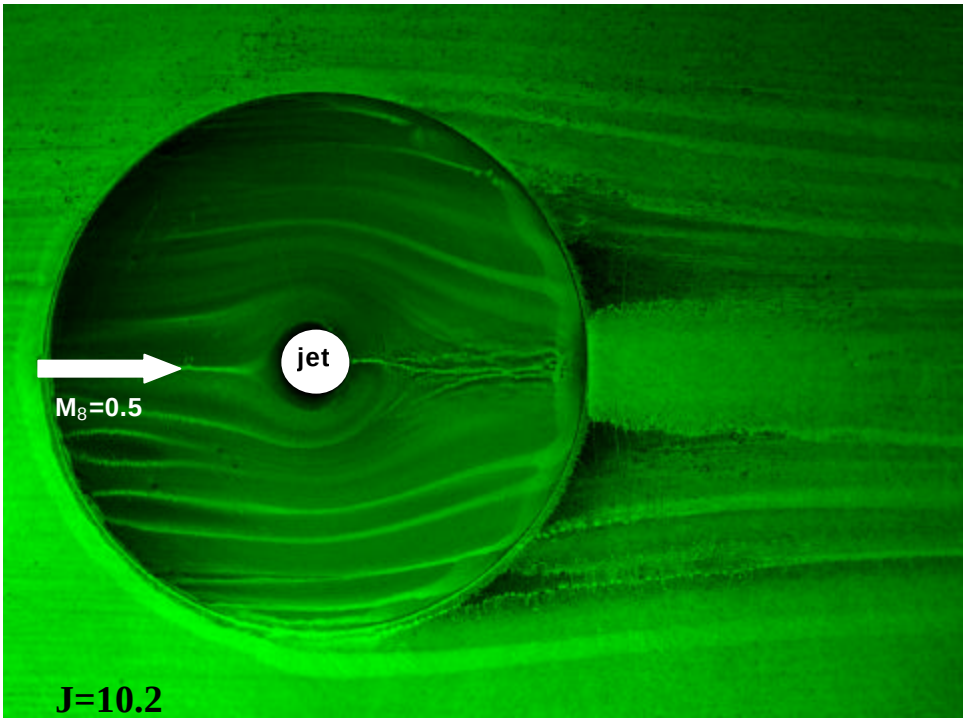

(g)

Figure 13, concluded

Also visible in some of the images are what appear to be the steady-state footprints of two vertically-oriented wake vortices that are shed from the jet, analogous to vortex shedding over a cylinder, which were identified by Fric and Roshko.[45] Figure 13c displays them most prominently. These features quantitatively appear much like those observed by Krothapalli[46] using oil flow tracers on the incompressible flowfield induced by a slit jet exhausting into a crossflow. As J increases while M_8 remains constant, the wake vortices appear to move close to the jet exit and shrink in size, but the images do not present incontestable evidence that these structures adjacent to the jet orifice in Figures 13a, 13b, and 13d result from the same phenomena as the apparent vortex footprints in Figure 13c. However, Kelso et al.[48] observed such structures in the immediate wake of their incompressible flowfield and speculated that they originated from a horseshoe vortex wrapped around the base of the jet before being turned and lifted off the surface. Computational studies have produced similar observations.[49,50] Comparable but less distinct structures can be seen at lower Mach numbers in Figures 13e and 13f. It is difficult to speculate on the nature of these vortex footprints using a qualitative measurement technique with essentially no frequency response to study an inherently unsteady interaction, but it seems likely that they result from either the wake vortices or liftoff of the horseshoe vortices.

4.3 Flat Plate Surface Pressure Measurements

4.3.1 Initial Measurements

Pressure measurements were first gathered on the flat plate using the flat-plate-instrumented nozzle mounted in the side-wall position. A sample of the mean pressure data is shown in Figure 14. The results shown are for the nominal condition of M_8=0.8 and J=10.2. Figure 14a shows the pressure coefficients along a line aligned with the freestream reaching approximately four jet diameters upstream and downstream. Figure 14b shows the pressure coefficients along an annulus surrounding the exit orifice of the nozzle; the 0° angle is referenced to the upstream edge of the jet. The data shown in Figure 14a are a combination of two wind tunnel runs, one made with the nozzle rotated 180° to interleave the pressure tap locations and effectively double the measurement resolution, as described in section 2.3.1 above. Occasional gaps in the data points are partly the infrequent result of data discarded due to leaks in the pressure lines and partly due to having slightly fewer pressure transducers than pressure taps. These gaps occurred a sufficient distance away from the jet exit such that the loss in spatial resolution did not create a problem because the interaction features exhibited only gradual variations.

Figure 14 displays the common features of jet-in-crossflow interactions. The surface pressures steadily rise as the crossflow stagnates against the jet exhaust in Figure 14a, terminating in a sharp pressure rise near the jet where the inner horseshoe vortex wraps around the base of the plume. The small drop in pressure just prior to this sharp increase (located at about x/d=-1) has been documented in supersonic flowfields just upstream of the bow shock location[51,52] and, as in the present case, appears to correspond to the flow separation that creates the inner horseshoe vortex. The location of this presumed separation point approximately coincides with the separation line visualized by the

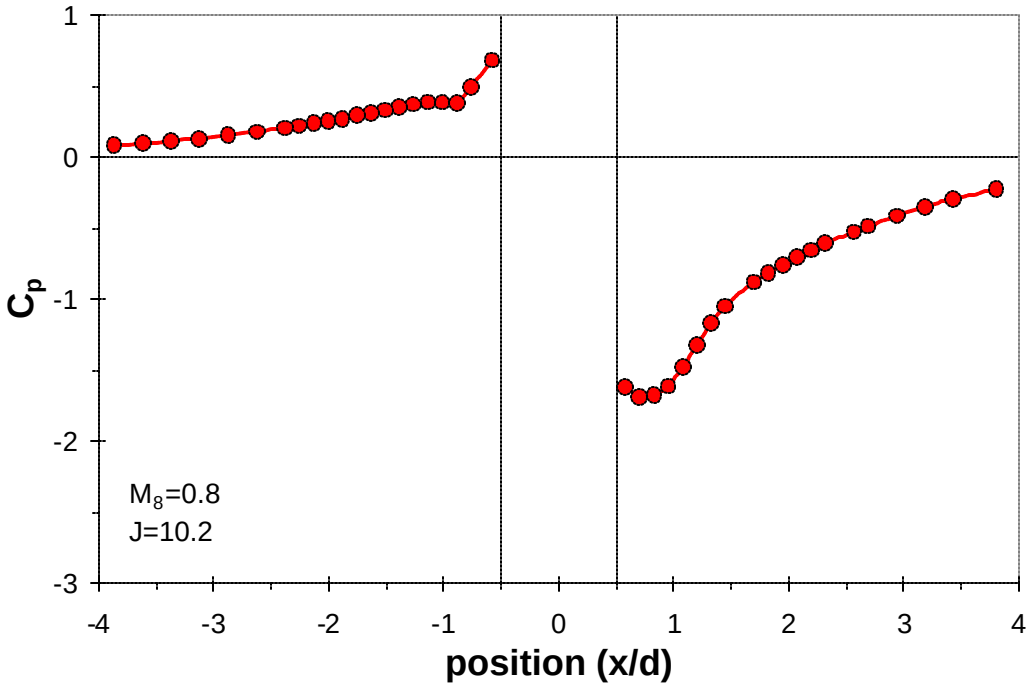

(a)

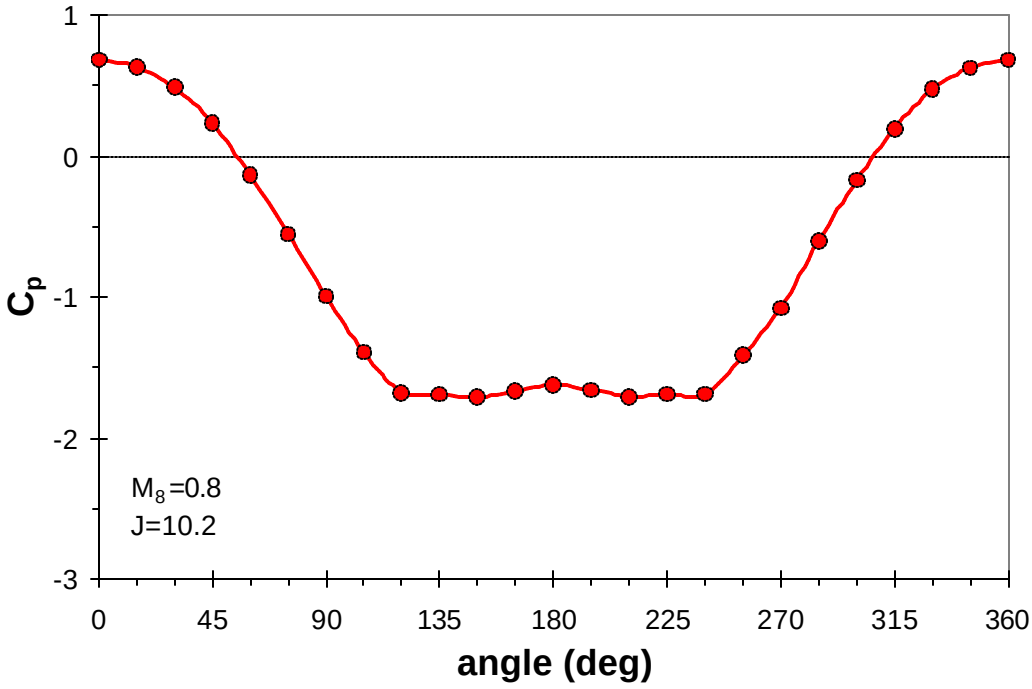

(b)

Figure 14: Mean surface pressure coefficients on the flat plate surface for the nominal flow conditions of M_8=0.8 and J=10.2; (a) along a line aligned with the freestream; (b) around an annulus surrounding the jet exit, where 0° is referenced to the upstream edge of the jet.

surface oil flow tracers in Figure 13a. Figure 14a also shows a local minimum just downstream of the jet, which plausibly is related to the near-wake structures (possibly the steady-state footprint of the wake vortices) observed in Figure 13a. Figure 14b shows that the local pressures shift from an elevated stagnation pressure to a wake pressure not at the side of the jet at 90° but rather, occurs further upstream near 60°. This is not obvious from the surface flow tracers in Figure 13a. Figure 14b additionally shows that the minimum wake pressure does not occur directly behind the jet at 180° as might be expected, but actually is found slightly to the sides at 150° and 210°. The wake structure visualized in Figure 13a is consistent with this observation.

4.3.2 Uncertainty Analysis

The nominal flow conditions were duplicated in four additional wind tunnel runs spread out over several days time to assess the repeatability of the measurements. The estimated mean variation between these runs for the flat plate surface pressures was ±0.007 c_p for most pressure taps and always less than ±0.02 c_p (as in the tunnel empty pressure measurements, found as the 95% confidence interval using Student's t-distribution that any given measurement lies within this distance of the mean). The larger latter repeatability was found to occur on only two of the 63 pressure taps measured on the flat plate, and even this value is within the thickness of the lines drawn in Figure 14. It should be noted that these values are a little smaller than the variations seen within any one wind tunnel run, indicating that this level of repeatability is consistent with the known ability to control the experimental parameters. It also is important to realize that the precision uncertainties quoted in Table 1 for the measurements of the wind tunnel and jet conditions are incorporated into the repeatability precision uncertainty of the measured surface pressures because any fluctuations in these conditions would influence the surface pressures.

Instrumentation uncertainty will be a factor in the measurement repeatability determined above, but this is simply the precision error it creates. The instrumentation additionally will induce uncertainties from the bias error associated with such phenomenon as calibration drift, electronic noise, temperature effects, and hysteresis. For pressure transducers, a reasonable conservative estimate of these effects is 0.25% of the full-scale measurement. The PSI ESP transducer modules have a manufacturer's quoted uncertainty of 0.1%, but this does not include effects from amplifiers, filters, cables, etc, so the 0.25% estimate is considered to be sufficiently conservative. For the ±100 kPa (±15 psi) transducers used in the flat plate measurements, this translates to an error of at most ±0.03 c_p depending upon the chosen flow conditions. Like the error induced by experimental repeatability, this is approximately the thickness of the pressure traces in Figure 14.

Past investigations have indicated that given a constant M_8, the dominant scaling parameter is J.[53-56] This has been confirmed for the present experiment by Figure 15, which shows the pressure traces for M_8=0.8 with the values of P_{0j} and p_w varied over four different cases to maintain J=10.2. As can be seen, when normalized properly, the data collapse. This is observed for the pressure trace aligned with the freestream direction in

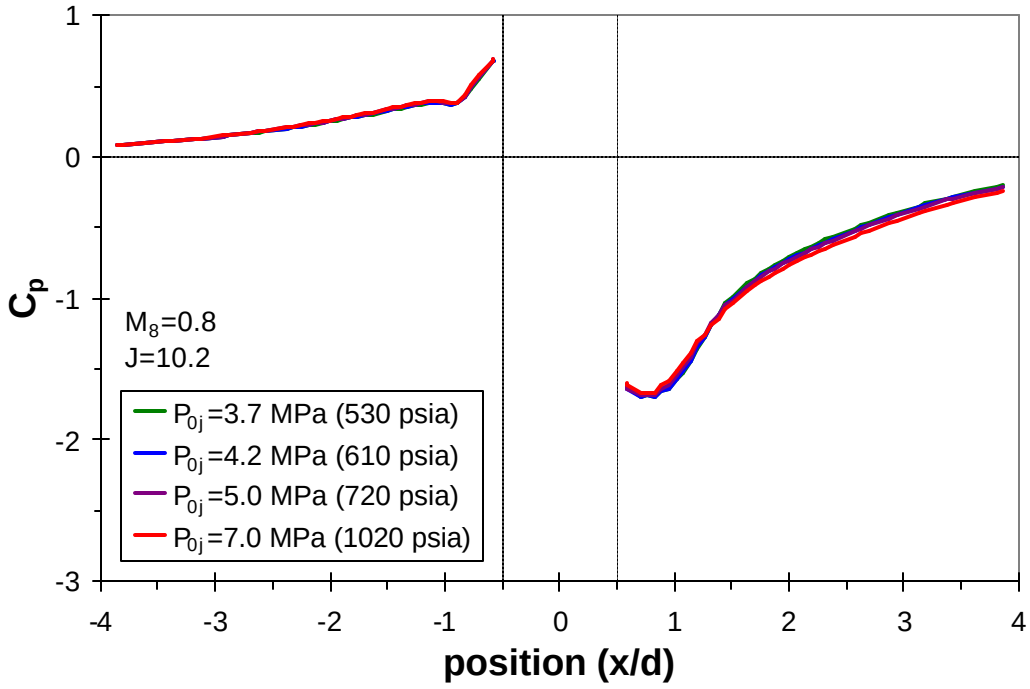

(a)

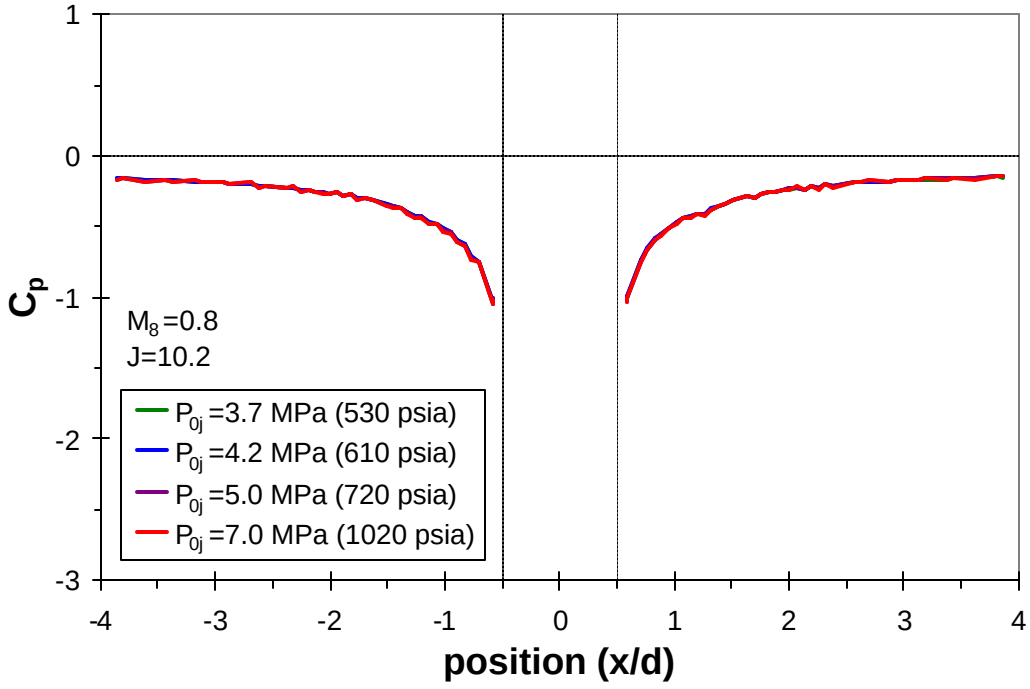

(b)

Figure 15: Collapse of the mean surface pressure coefficients on the flat plate surface for M_8=0.8 with P_{0j} and P_w varied to maintain J=10.2; (a) along a line aligned with the freestream; (b) along a line perpendicular to the freestream; (c) around an annulus surrounding the jet exit (on following page).

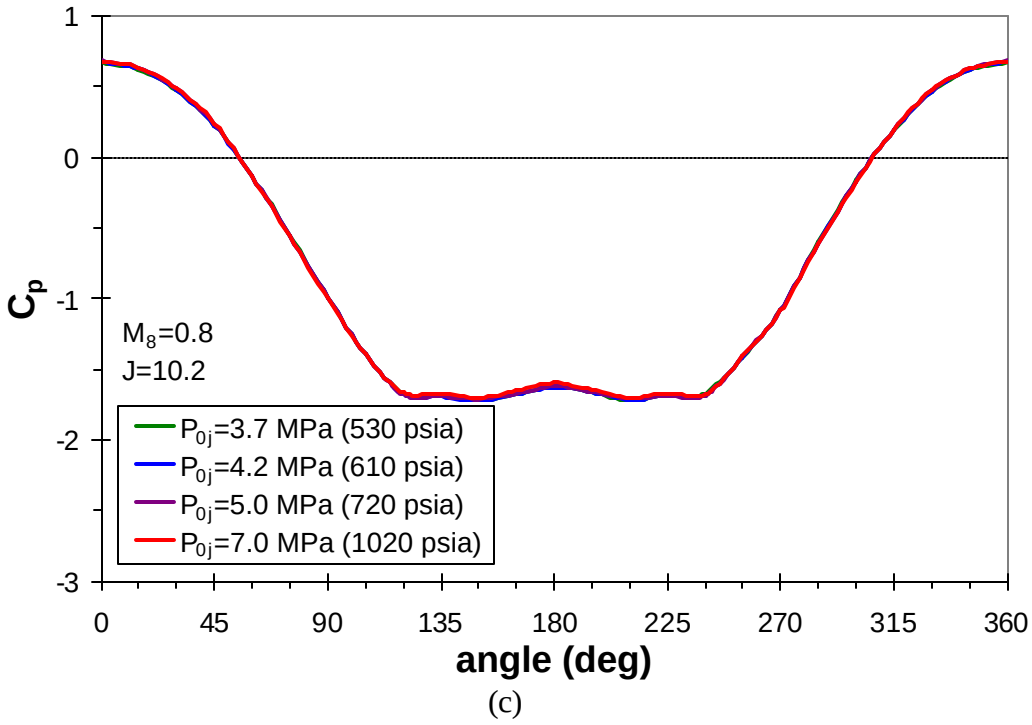

(c)

Figure 15, continued.

Figure 15a (i.e., the nozzle insert is oriented to ?=0° and ?=180° for the two interleaved wind tunnel runs), for the pressure trace perpendicular to the freestream direction in Figure 15b (i.e., the nozzle insert is oriented to ?=90° and ?=270°), and for the annulus of pressure taps around the exit orifice in Figure 15c. Similar results were found for different values of M_8 and J, but are omitted for brevity. This knowledge can be invoked to limit the number of different conditions that need to be studied since pressure-matching similarity can be employed.

A noteworthy characteristic of the pressure trace in Figure 15b is that the undulations seen in it are constant at the different values of P_{0j}. Their repeatability indicates that it is not created by the precision of the instrumentation, which is consistent with the earlier estimate of the precision uncertainty to be less than the amplitude of these wiggles. Some sort of bias error also could contribute to this phenomenon, possibly due to minor leaks in the pressure tubing or burrs in the pressure taps, but the most likely explanation is that it results from the interleaving of the taps. Recall that each pressure trace is formed from two wind tunnel runs, where for one run the nozzle insert is rotated 180° with respect to its position in the previous run. Therefore, once these two runs are assembled into one pressure trace, any difference between them will create a variation in the pressure trace with a period equal to the physical spacing of the pressure taps. It already has been established that repeatability considerations are not sufficient to induce the observed amplitude of rippling, so these variations must result from some flowfield nonuniformity around the axial centerline of the test section. When the pressure taps are oriented in their first position, they measure a slightly different flowfield than that seen when rotated

into their second position. Upon assembly into a single interleaved pressure trace, the undulations of Figure 15b are created. It is not immediately clear whether this nonuniformity is found in the wind tunnel freestream, the jet insert itself, the instrumentation, or some combination thereof.

To further investigate the nonuniformity, Figure 16 displays pressure traces acquired with the nozzle oriented into two different symmetrical positions across the wind tunnel centerline. Figure 16a shows the surface pressures on the annulus of pressure taps and Figure 16b shows the pressures perpendicular to the freestream direction; because the pressure trace aligned with the freestream direction lies on the wind tunnel's plane of symmetry, it is not expected to display any variation with nozzle orientation and is omitted from this figure. For this figure, it is necessary to derive the pressure traces from a single wind tunnel run rather than two interleaved runs to isolate the influence of nonuniformities. Each figure also shows a single pressure trace reflected across the line of symmetry for comparison. If the flow nonuniformity originates entirely with the wind tunnel freestream, the pressure trace acquired with a nozzle orientation of ?=0° in Figure 16a should overlap the pressure trace at ?=180° since regardless of the nozzle orientation the same nonuniform freestream would be measured. On the other hand, if the nonuniformity is produced solely by the nozzle insert (either due to a machining asymmetry in the nozzle contour or the interface between the nozzle's flat plate surface and the test section's window blank), it would rotate with the nozzle orientation; therefore, mirroring the pressure trace from the nozzle orientation of ?=0° across the wind tunnel centerline should match the pressures measured at a nozzle orientation of ?=180°. In the former case, the pressure taps are moved to measure the nonuniformity, but in the latter case the nonuniformity moves with the pressure taps. The same argument can be made with regards to the nozzle orientations of ?=90° and ?=270° in Figure 16b.

Unfortunately, the results of this exercise are not perfectly clear. Figure 16a shows only small differences between the three pressure traces, but where differences are evident, the mirrored ?=0° case is sometimes closer to the ?=0° curve and sometimes closer to the ?=180° curve. Similar behavior is seen in Figure 16b. This suggests that nonuniformities arise both from the flow through the test section and from the nozzle itself (or its mounting apparatus). However, the differences between the curves are rarely greater than the thickness of the lines. Recalling that the instrumentation and repeatability uncertainties are approximately the line thickness, this indicates that the pressure differences observed in Figure 16 are not sufficiently large to draw any substantial conclusions concerning the source of the nonuniformity. The deviations in the data incurred by this effect have an estimated mean of about ±0.03 c_p and rise to a maximum of ±0.1 c_p in regions of greatest variation. The former value represents the observed deviation due to nonuniformity for about 95% of the data points, while the larger latter value is representative of only a few locations. This is a greater effect than was observed for the nonuniformity investigation in the tunnel empty measurements.

The nonuniformity investigation captured by Figure 16 should also account for the presence of leaks in the pressure tubing. Significant leaks were easily detected during the rigorous instrumentation checkout since they created spikes in the pressure traces, but small leaks could plausibly have escaped this process. However, upon rotating the nozzle

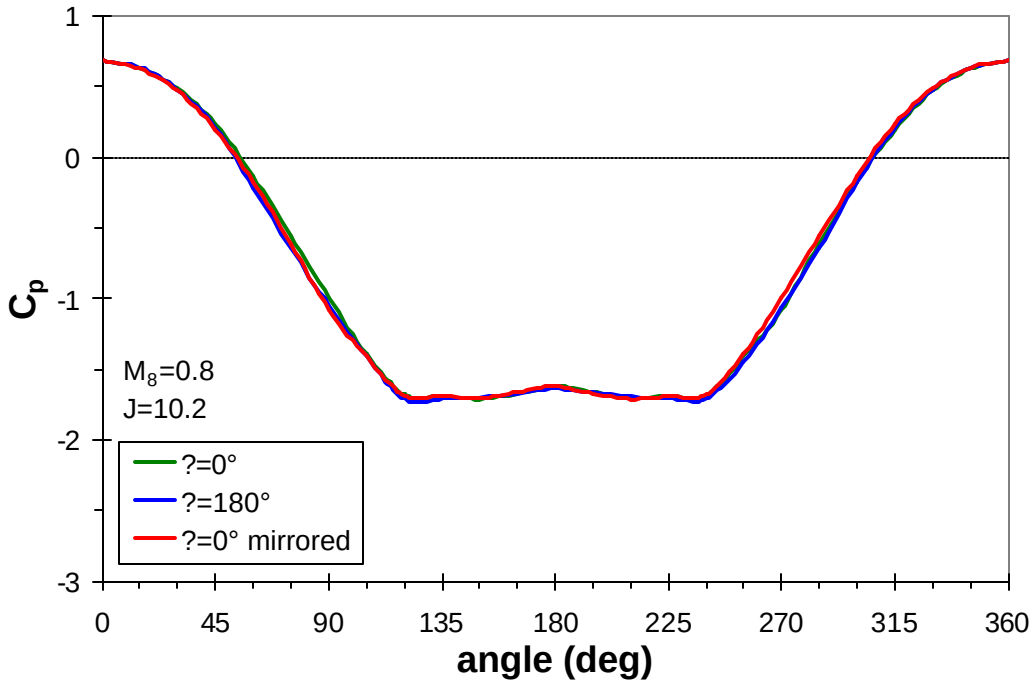

(a)

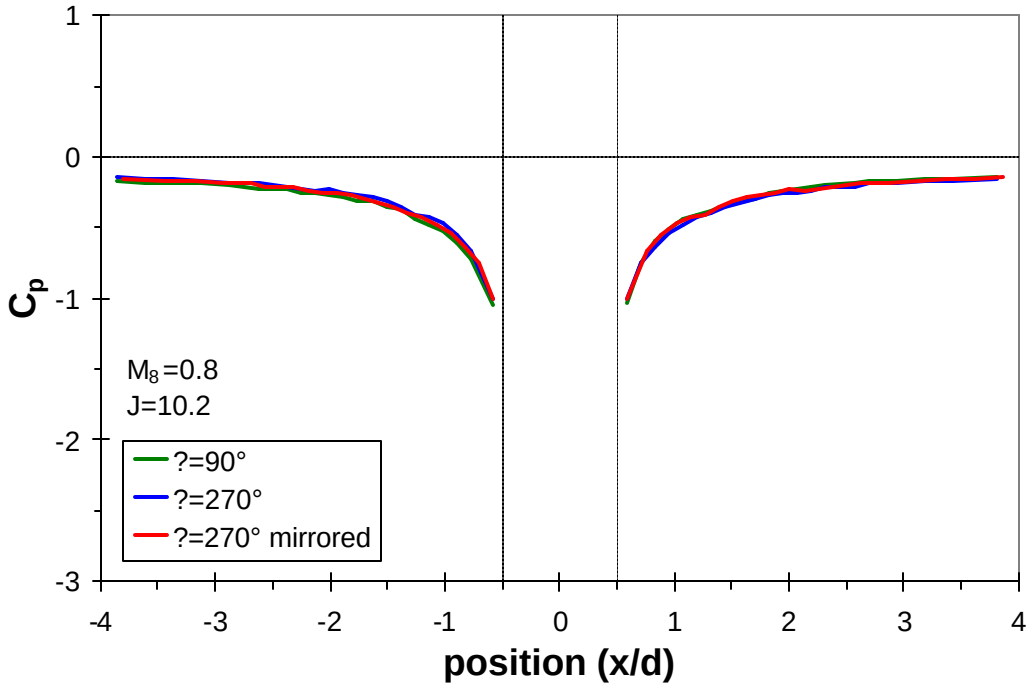

(b)

Figure 16: Flowfield nonuniformity shown by pressure traces acquired with the nozzle oriented into two different symmetrical positions across the wind tunnel centerline. Each plot also shows a single pressure trace reflected across the line of symmetry for comparison. Data is shown: (a) around an annulus surrounding the jet exit; (b) along a line perpendicular to the freestream.

insert to place the pressure taps into a different but symmetric position, any pressure tap containing a leak would be relocated and its former position in the pressure trace then would be measured by a different (presumably non-leaking) pressure tap. The variation between the leaking and non-leaking taps thus would be incorporated into Figure 16 and the quoted uncertainty estimates include this effect.

As an additional exercise into possible nonuniformity effects, the jet stagnation chamber was rotated into a different radial position while the nozzle remained oriented at ?=90° such that the two pressure tap rays were perpendicular to the freestream direction. No discernable change in the flat plate pressures was observed. The thermocouple within the jet stagnation chamber is present on only one side of the chamber and thus plausibly may induce a nonuniformity, but this cannot be the case since rotating the stagnation chamber had no impact on the data. A more direct test was conducted where the thermocouple was removed for two wind tunnel runs, but again, no change in the data was detected. Therefore neither the jet settling chamber nor the incoming gas supply contribute to the flow nonuniformity.

The uncertainty of the measurements presented below is attributable to all of the above factors. The repeatability of the measurements was found to have an estimated mean of ±0.007 c_p and no more than ±0.02 c_p. Instrumentation uncertainty from the pressure transducers has been conservatively estimated as at most ±0.03 c_p. The largest source of error was found to be nonuniformities in both the wind tunnel flowfield and in the nozzle itself. The estimated mean of these errors is ±0.03 c_p and has a maximum of ±0.1 c_p at a small number of data points. The total effect of these error sources (root-sum-square method) is ±0.04 c_p with a maximum of ±0.1 c_p. This corresponds to 0.9% of the full-scale measurement of ±100 kPa (±15 psi) for ±0.04 c_p and 2% of full-scale for ±0.1 c_p. In the figures shown throughout this document, ±0.04 c_p is approximately three times the thickness of the pressure traces and is the most reasonable uncertainty estimate although a small number of data points may exceed this range and fall within an uncertainty of ±0.1 c_p (approximately 5% of the total data points would be subject to this larger value). It is recommended that the ±0.04 c_p uncertainty be employed in validation analysis since it is most generally applicable. No pretense is made that these uncertainty estimates are all inclusive; however, these estimates are the best that could be determined during the present experiment.

4.3.3 Detailed Measurements

Mean surface pressures were measured on the flat plate at a variety of nozzle orientations for each of the eight sets of flowfield conditions. This volume of pressure traces provides a quantitative means of examining the surface features in the near-field of the jet-in-crossflow interaction and offers the possibility of comparison with numerical results at many different locations. Some of these traces were created by interleaving the data from two separate runs at nozzle orientations 180° apart, while others used only a single tunnel run. Uncertainty bars are shown on only a few of the following figures, but the analysis used above in section 4.3.2 applies to all.

Figure 17 displays the pressure traces with the nozzle installed at an orientation of ?=0°, which aligns the two rays of pressure taps to the freestream direction of the wind tunnel. It actually is composed of two interleaved wind tunnel runs. Figure 17a shows the five cases where M_8=0.8 and J is varied and Figure 17b shows the four cases where J=10.2 and M_8 is varied. The nominal case is shown in both figures, hence nine pressure traces for only eight sets of flowfield conditions. A single set of uncertainty bars is shown in each figure to represent the estimated uncertainty for each data point; this is the ±0.04 c_p value determined above in section 4.3.2.

Figures 17 through 27 display the surface pressures at values of ? from 0° to 90° in increments of 7.5° or 15°. Most of these figures are similar to Figure 17, in that they show one plot for M_8=0.8 and a second for J=10.2. Figures 22 and 24, at ?=37.5° and ?=52.5°, show a single plot containing traces only for three cases, intended to provide some extra detail on the small decline in pressure seen in the jet's wake. No uncertainty bars are shown for any figure except Figure 17, but they are the same ±0.04 c_p value in all cases. Interleaved data is provided at ?=0° and ?=90° but only a single wind tunnel run was conducted for each pressure trace at every other angle. Although the figures are labeled with nozzle orientation angles from 0° to 90°, these actually fully cover the entire 360° of the flat plate. Since rays extend in both directions, 0° to 90° also covers 180° to 270°; employing symmetry arguments across the wind tunnel centerline allows the 0° to 90° wedge to also apply to the 270° to 360° wedge and the 180° to 270° wedge to additionally apply to 90° to 180°. Although section 4.3.2 above showed that symmetry does not perfectly apply, such mild discrepancies have been incorporated into the quoted uncertainty estimate. A ray of pressure data extending in the –x direction is aligned in the 0° to 90° direction since the nozzle installation is determined by this bearing The opposite ray of pressure data, in the +x direction, extends in the 180° to 270° direction although the nozzle orientation remains within 0° to 90° since it has not been physically reinstalled. Since the pressure data at ?=0° and ?=90° actually is interleaved from two different wind tunnel runs, the nozzle was physically installed into two different orientations despite the manner in which ? is expressed.

Some observations may be made concerning the flowfield features as illuminated by the surface pressure measurements. Figure 17a displays the behavior of the mean pressure coefficients aligned to the freestream direction, as in the initial measurements shown in Figure 14a, but multiple traces are given here for varying values of J while M_8 is held constant at 0.8. As anticipated, it shows that for increasing J, the size and strength of the stagnation region and inner horseshoe vortex increases upstream of the plume while the pressure decrease in the wake grows more extreme. This behavior is consistent with the vast body of jet-in-crossflow literature, including both supersonic and incompressible regimes. The local drop in pressure in the stagnation region can be seen to grow larger and move upstream as J is increased. This is consistent with the surface flow tracers of Figure 13, which show a larger horseshoe vortex for larger J. As noted previously, this pressure dip qualitatively appears to correspond to the separation point where the inner horseshoe vortex forms. It is not clear what induces the local minima in the wake pressures, though it seems likely that it is tied to the presumed wake vortices that were seen in the surface flow tracers (which alternatively may be explained as the liftoff location of the horseshoe vortices once they wrap around the jet plume).

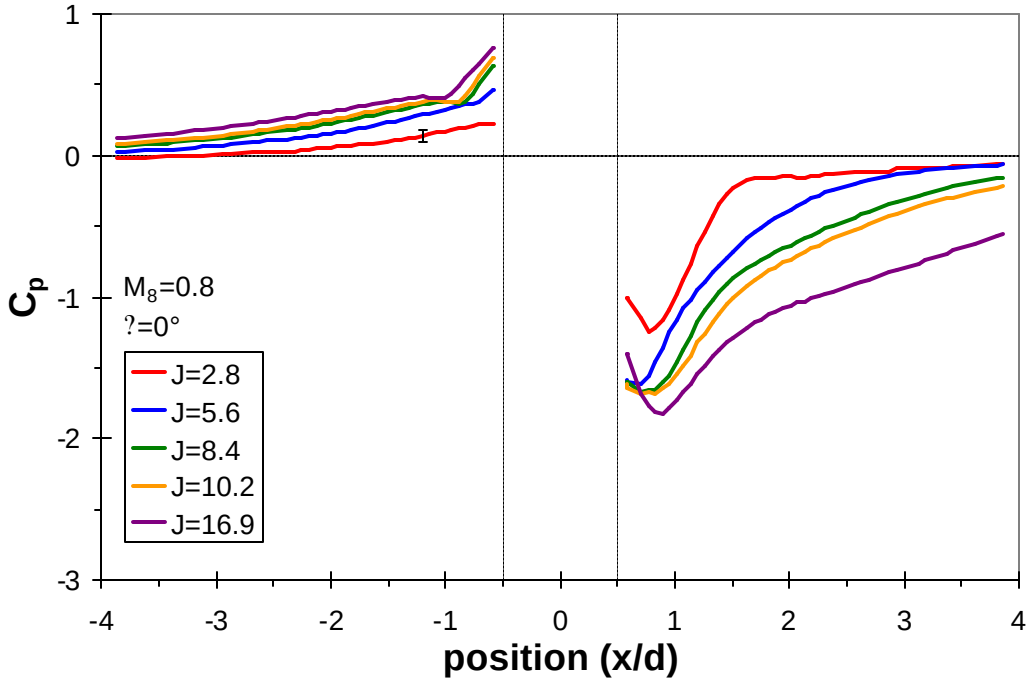

(a)

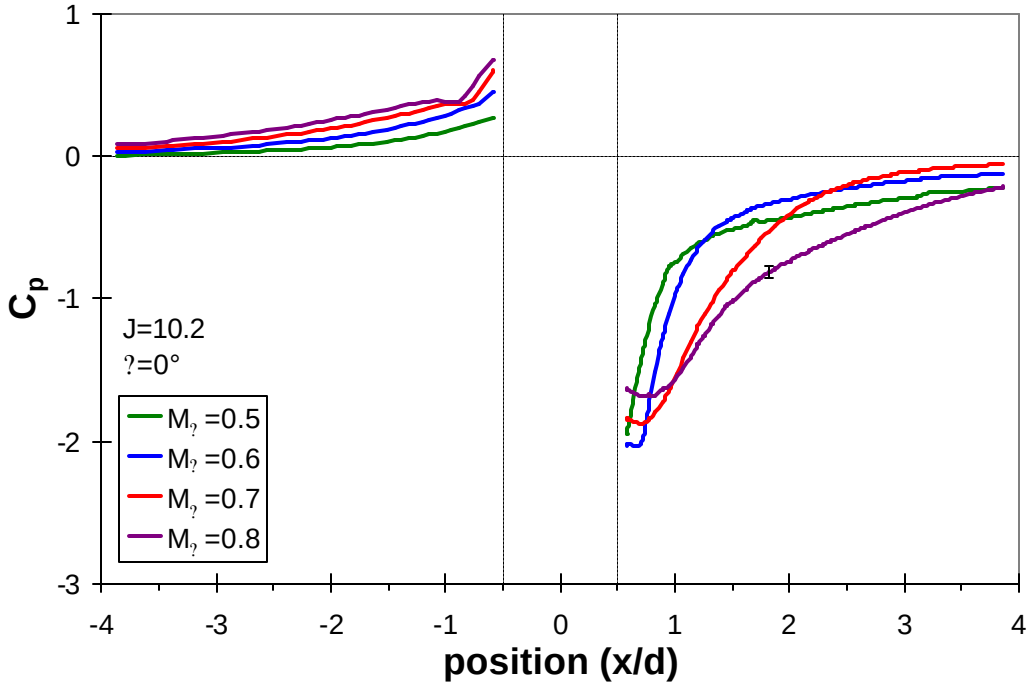

(b)

Figure 17: Mean surface pressure coefficients for a nozzle orientation of ?=0°; (a) varying J while maintaining a constant M_8=0.8; (b) varying M_8 while maintaining a constant J=10.2.

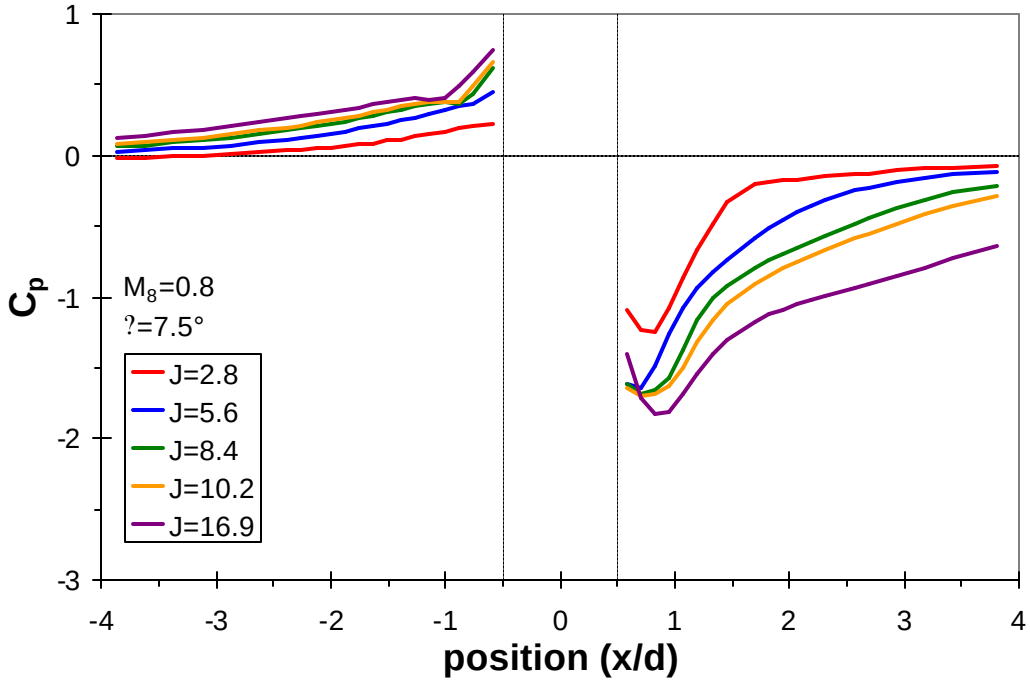

(a)

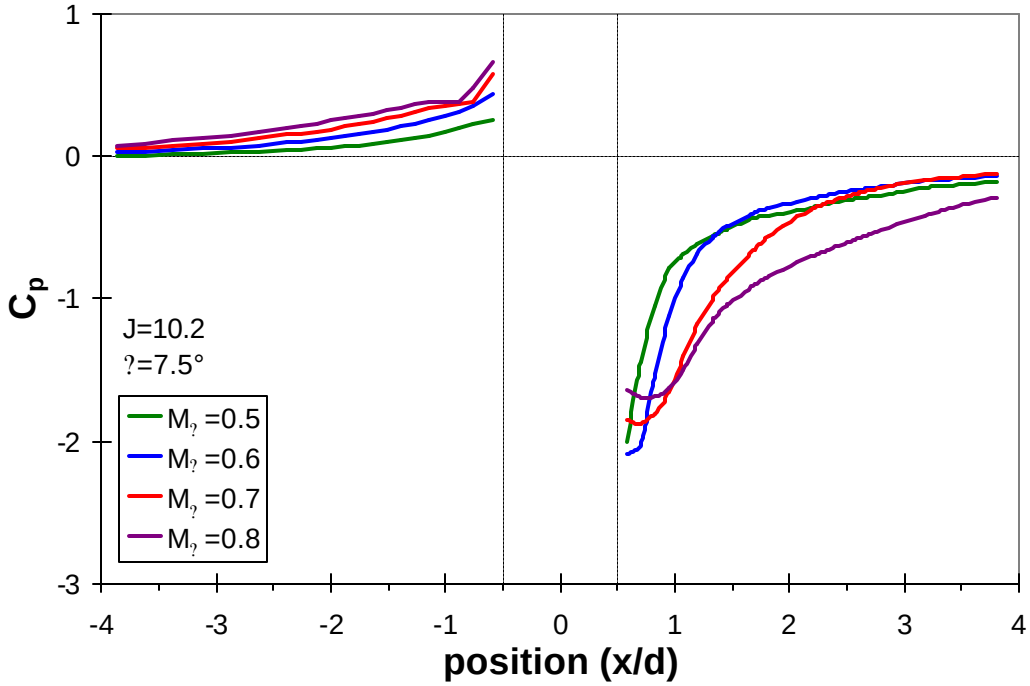

(b)

Figure 18: Mean surface pressure coefficients for a nozzle orientation of ?=7.5°; (a) varying J while maintaining a constant M_8=0.8; (b) varying M_8 while maintaining a constant J=10.2.

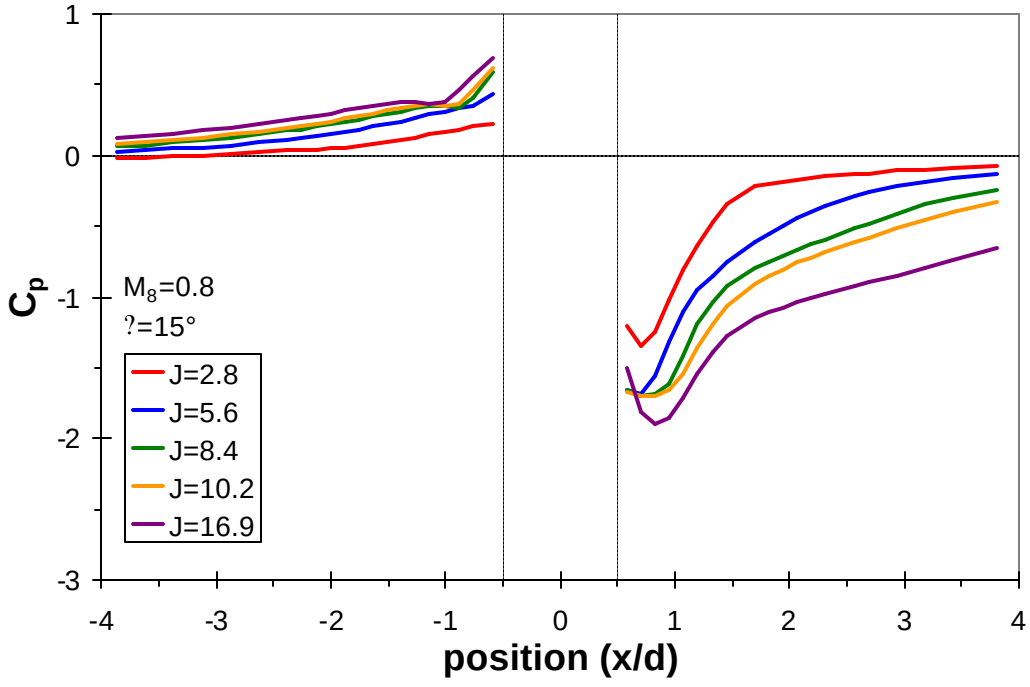

(a)

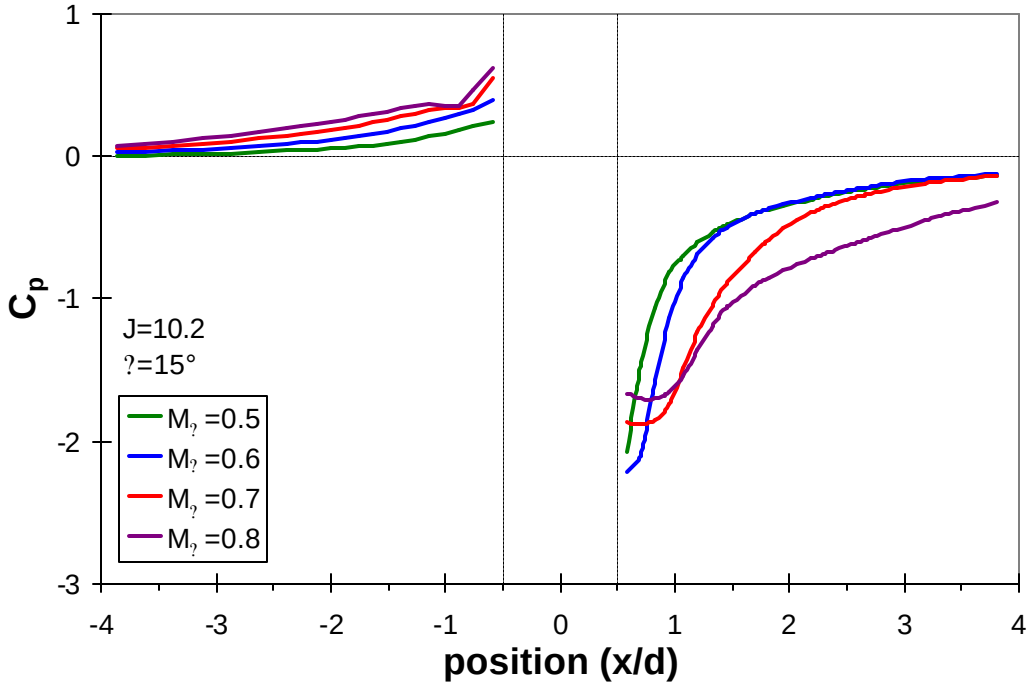

(b)

Figure 19: Mean surface pressure coefficients for a nozzle orientation of ?=15°; (a) varying J while maintaining a constant M_8=0.8; (b) varying M_8 while maintaining a constant J=10.2.

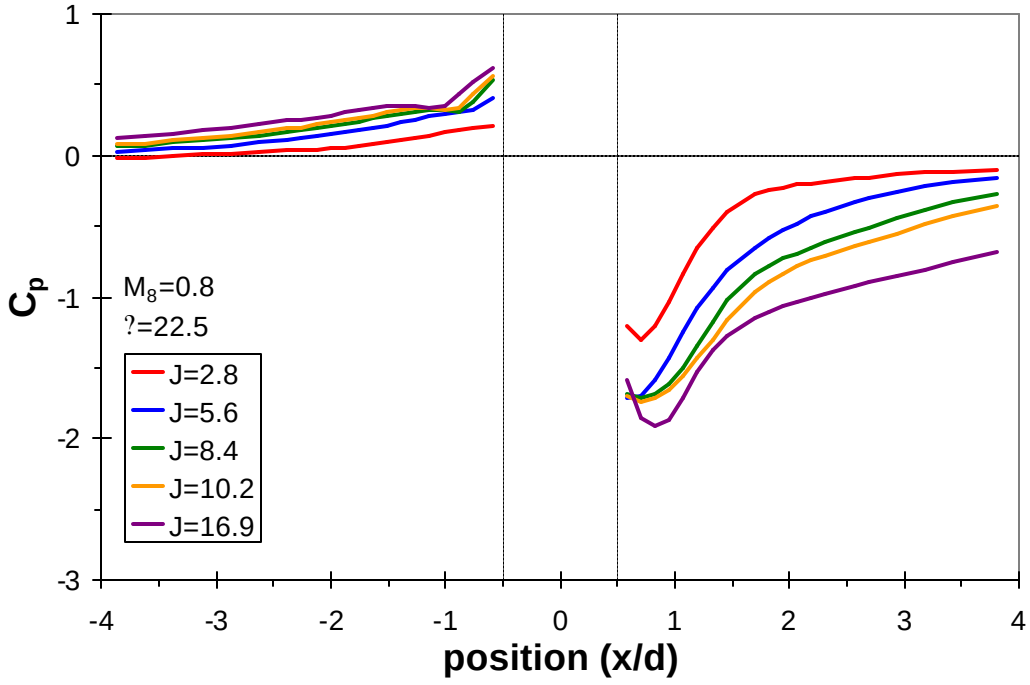

(a)

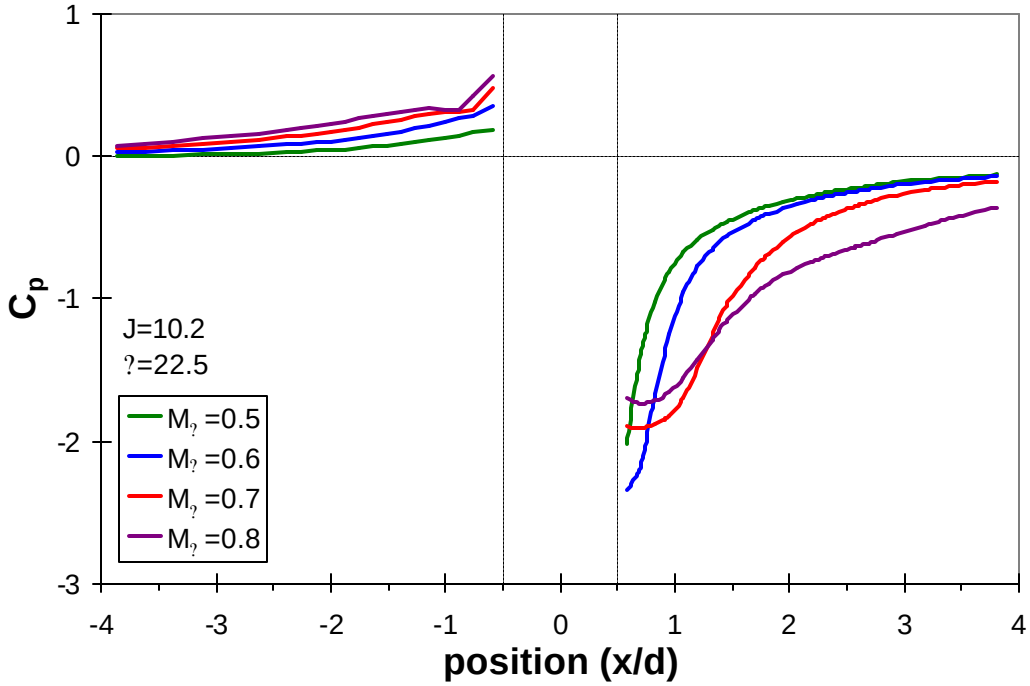

(b)

Figure 20: Mean surface pressure coefficients for a nozzle orientation of ?=22.5°; (a) varying J while maintaining a constant M_8=0.8; (b) varying M_8 while maintaining a constant J=10.2.

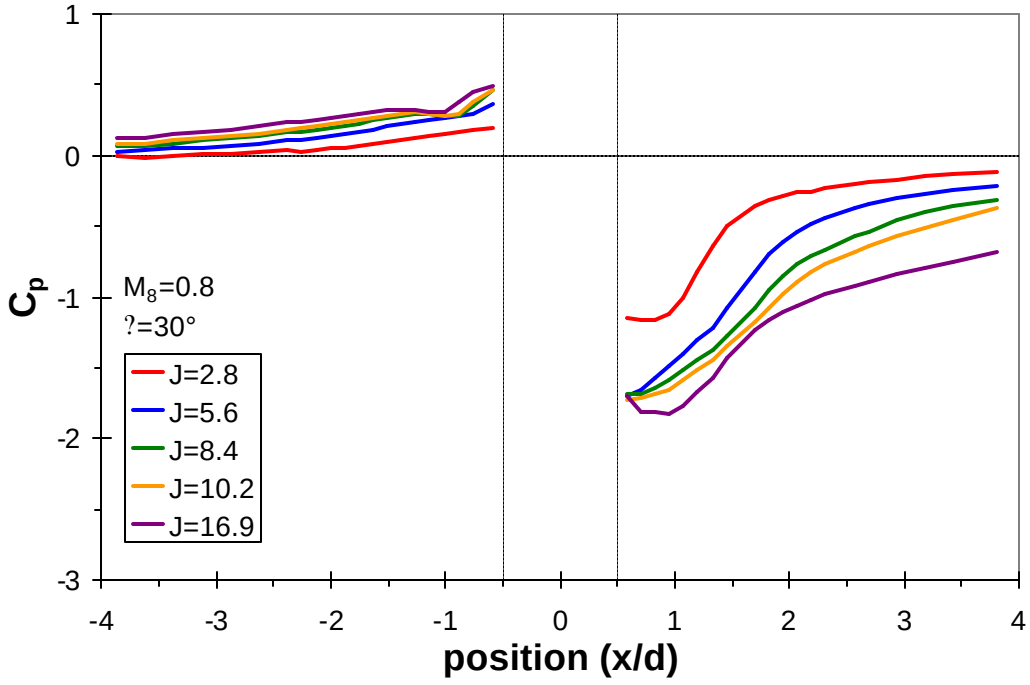

(a)

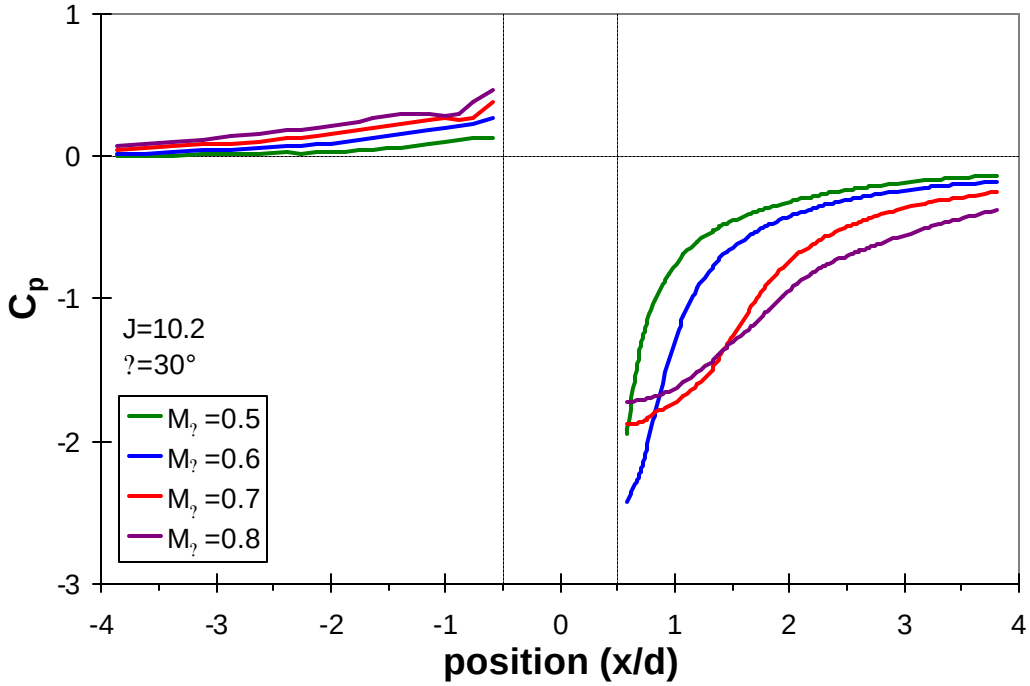

(b)

Figure 21: Mean surface pressure coefficients for a nozzle orientation of ?=30°; (a) varying J while maintaining a constant M_8=0.8; (b) varying M_8 while maintaining a constant J=10.2.

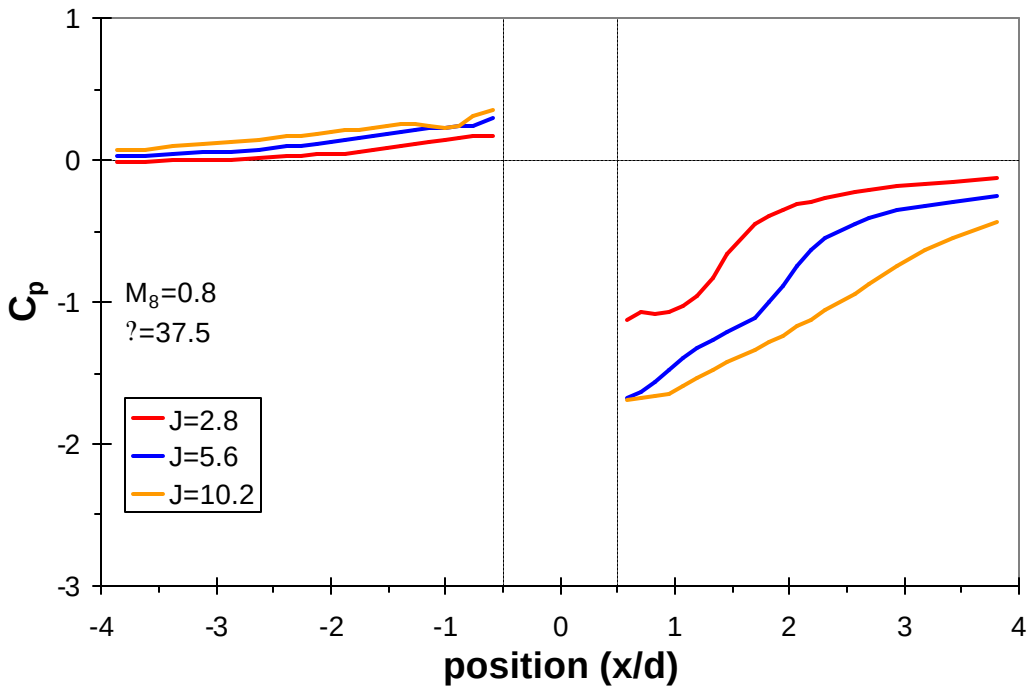

Figure 22: Mean surface pressure coefficients for a nozzle orientation of ?=37.5°; fewer cases were examined at this value of ?.

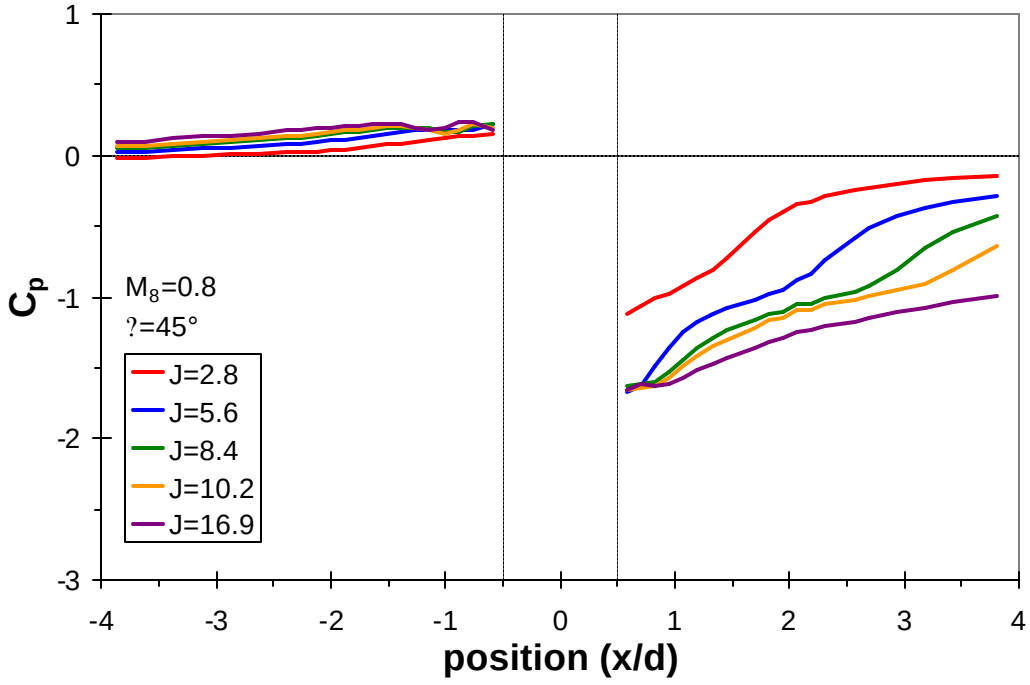

(a)

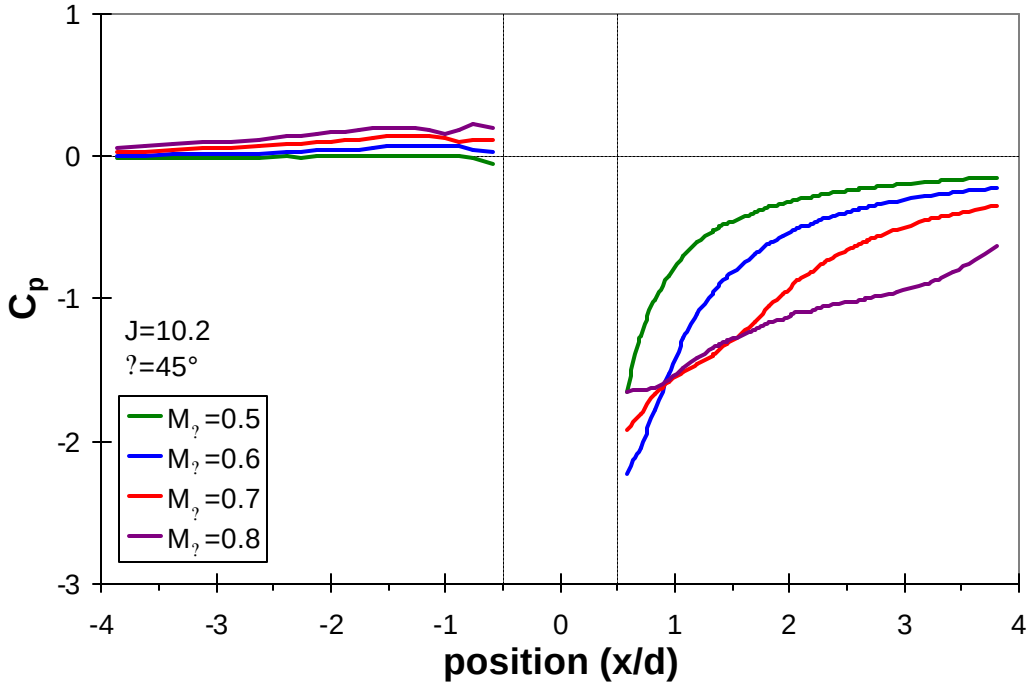

(b)

Figure 23: Mean surface pressure coefficients for a nozzle orientation of ?=45°; (a) varying J while maintaining a constant M_8=0.8; (b) varying M_8 while maintaining a constant J=10.2.

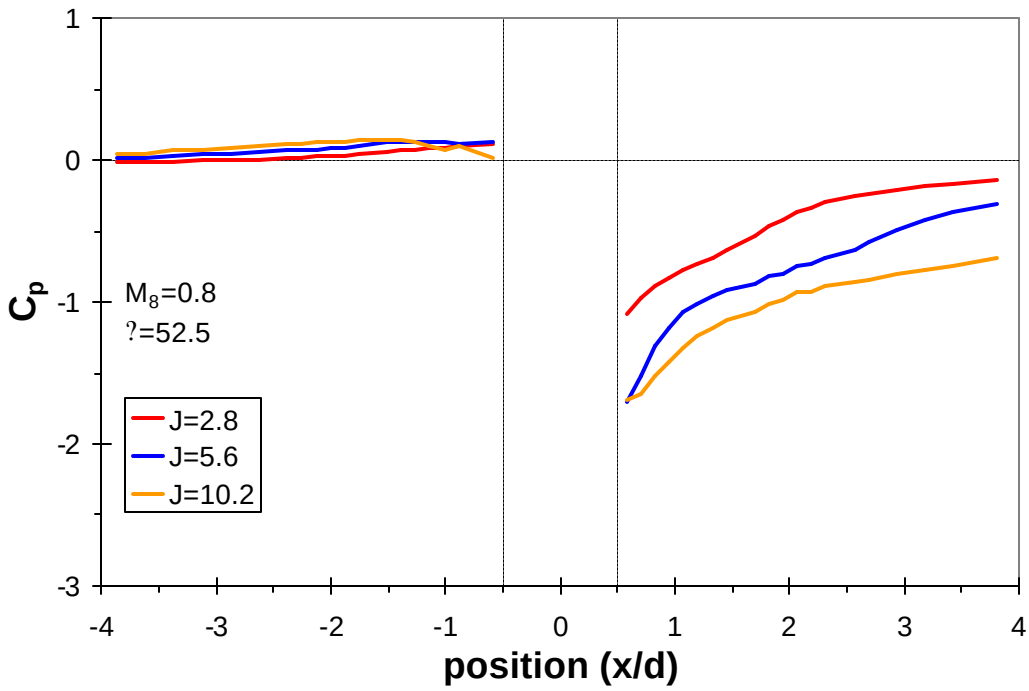

Figure 24: Mean surface pressure coefficients for a nozzle orientation of ?=52.5°; fewer cases were examined at this value of ?.

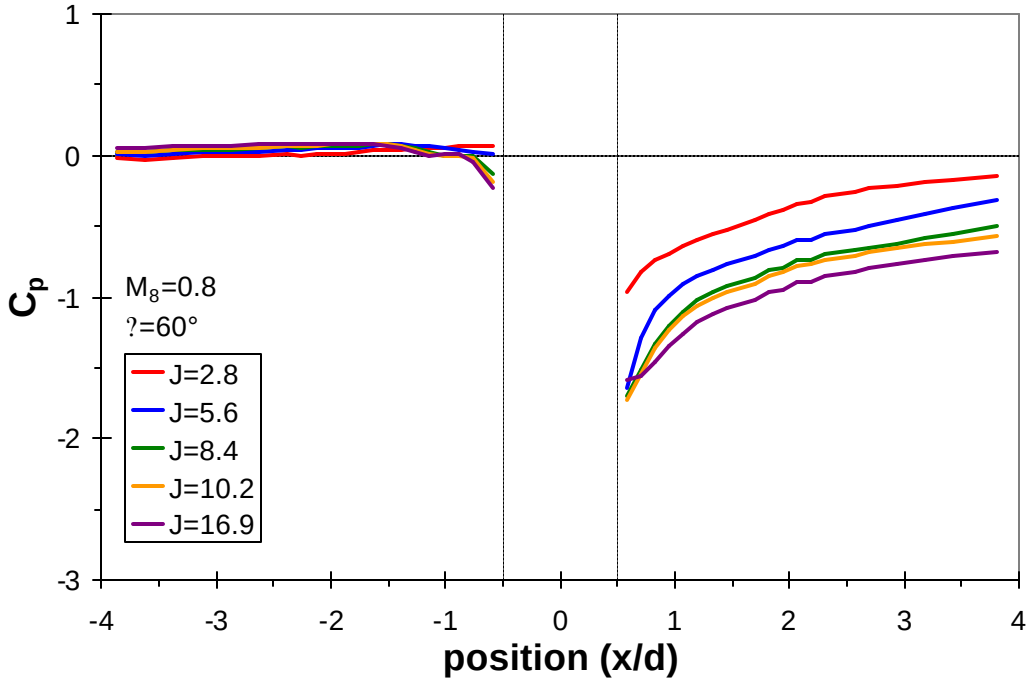

(a)

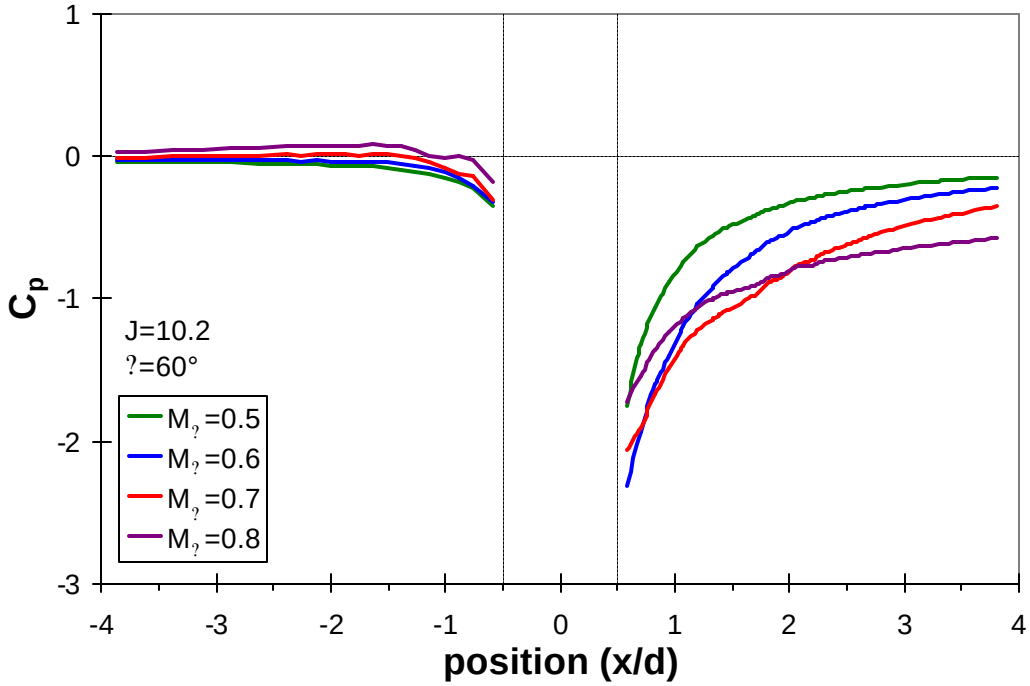

(b)

Figure 25: Mean surface pressure coefficients for a nozzle orientation of ?=60°; (a) varying J while maintaining a constant M_8=0.8; (b) varying M_8 while maintaining a constant J=10.2.

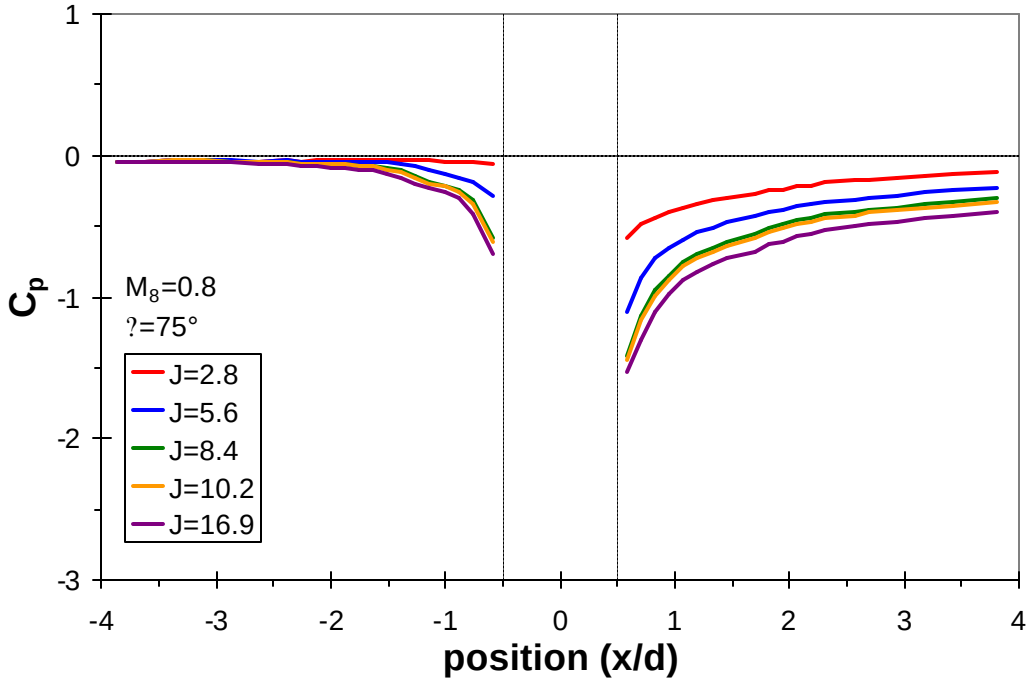

(a)

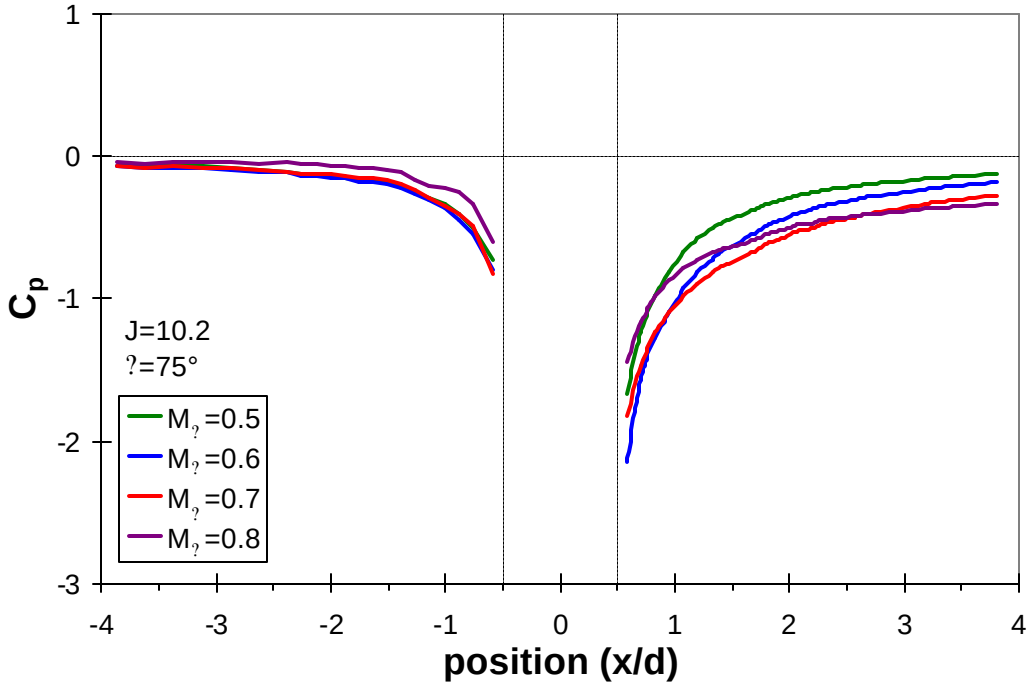

(b)

Figure 26: Mean surface pressure coefficients for a nozzle orientation of ?=75°; (a) varying J while maintaining a constant M_8=0.8; (b) varying M_8 while maintaining a constant J=10.2.

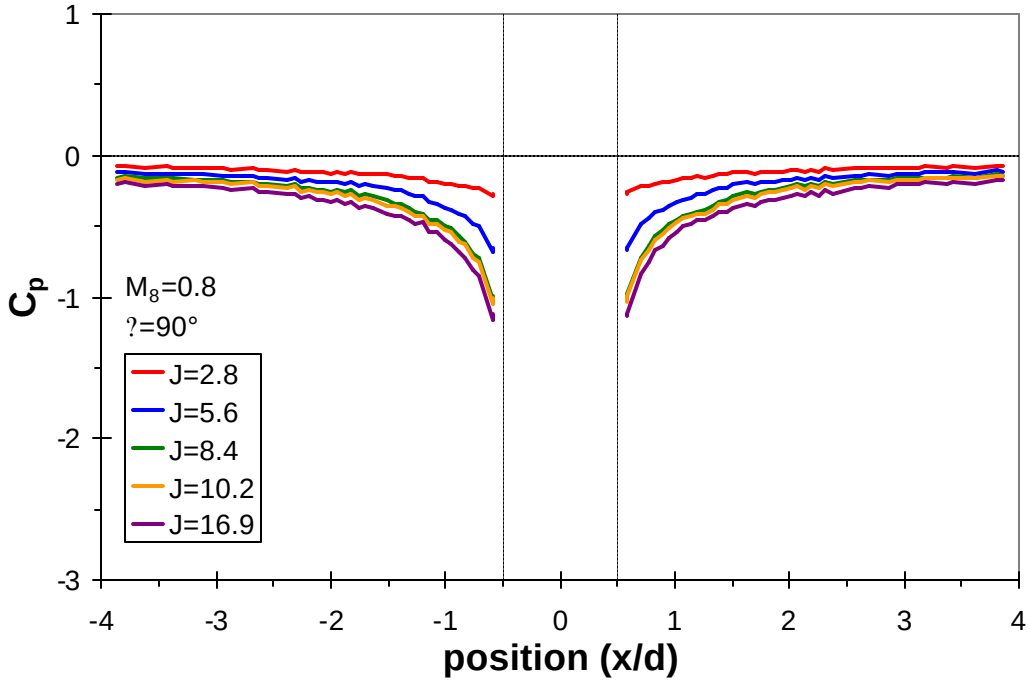

(a)

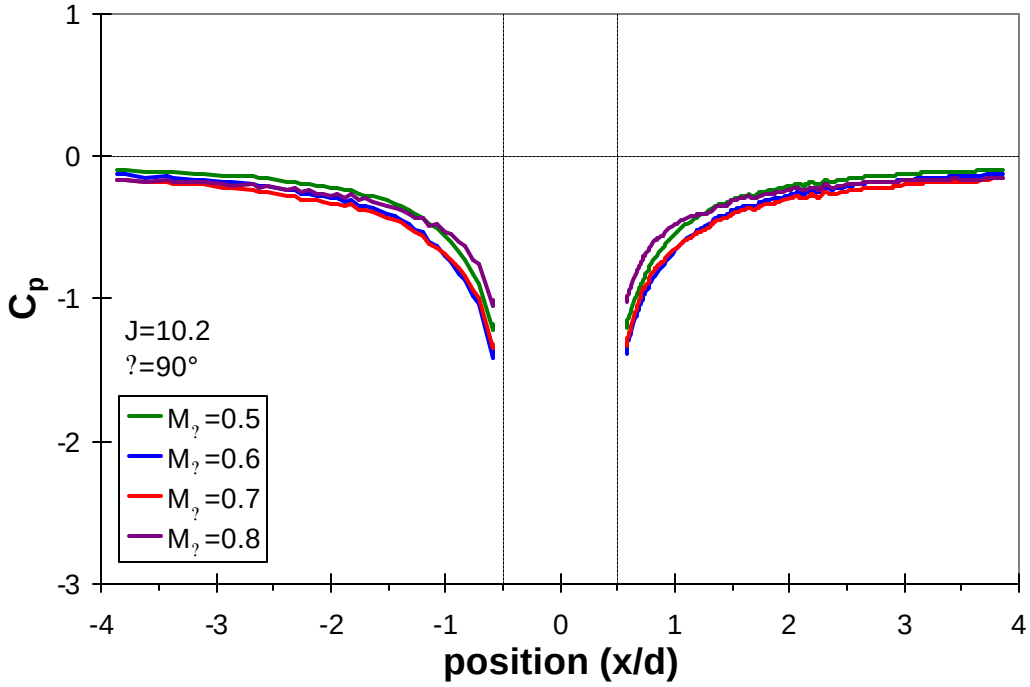

(b)

Figure 27: Mean surface pressure coefficients for a nozzle orientation of ?=90°; (a) varying J while maintaining a constant M_8=0.8; (b) varying M_8 while maintaining a constant J=10.2.

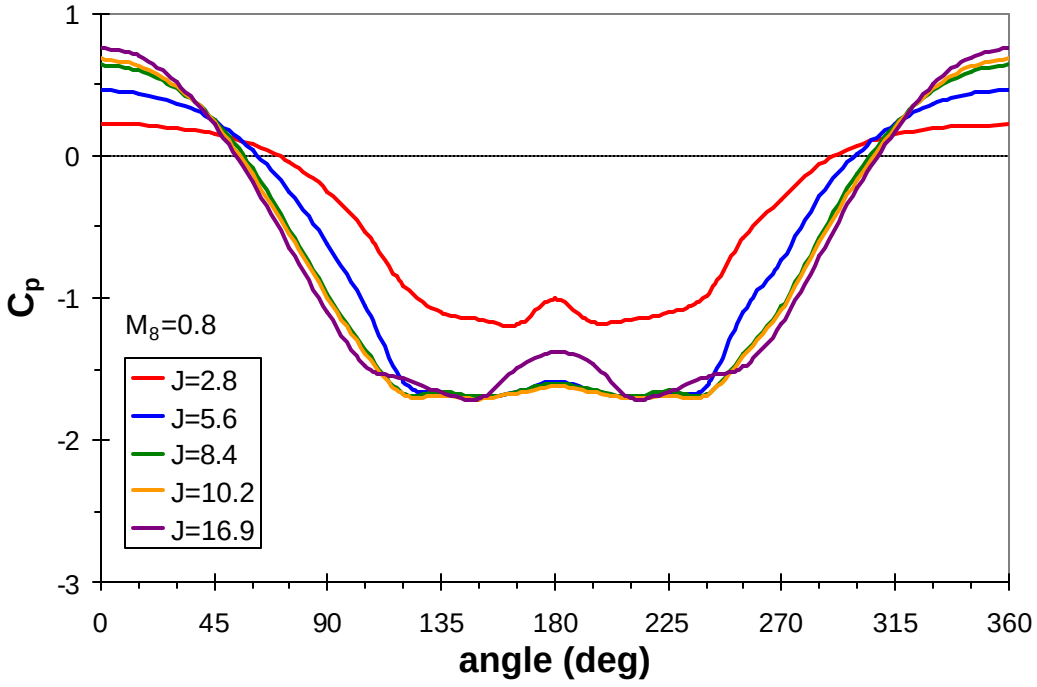

(a)

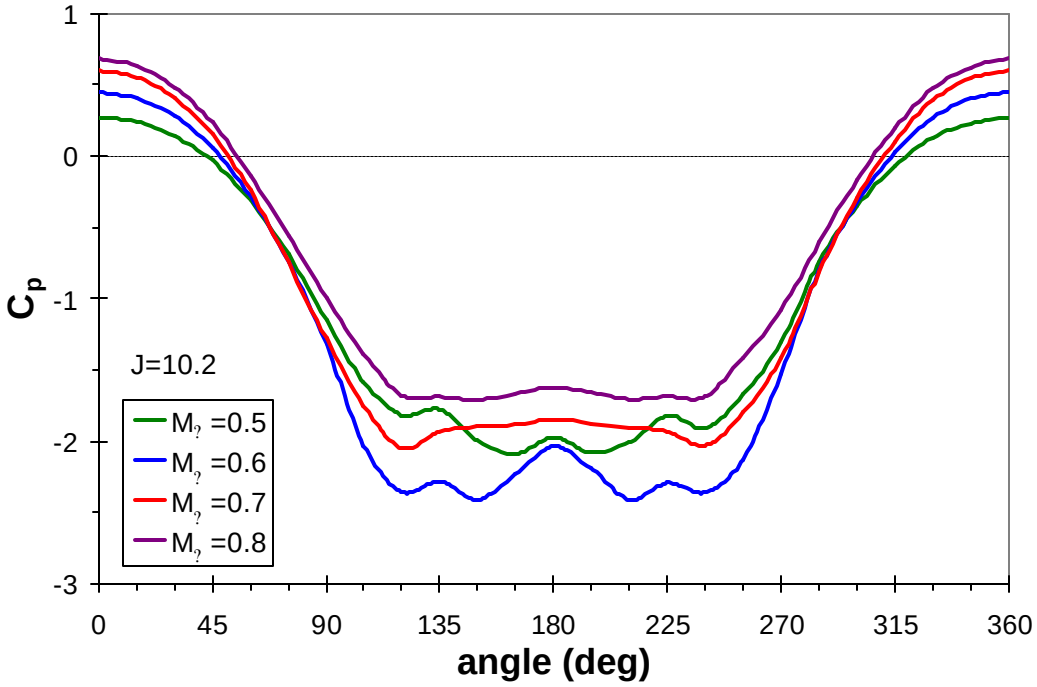

(b)

Figure 28: Mean surface pressure coefficients around an annulus surrounding the jet exit; (a) varying J while maintaining a constant M_8=0.8; (b) varying M_8 while maintaining a constant J=10.2.

Figure 17b shows the mean pressure coefficients for varying M_8 while J is maintained at 10.2, again with the nozzle aligned to the freestream. Similar to the behavior for increasing J, as M_8 rises the pressure increase in the stagnation region and the pressure decline in the wake both increase in magnitude. For larger M_8, the pressure dip in the stagnation region associated with the horseshoe vortex moves upstream, corresponding to the larger horseshoe vortex seen in the matching surface flow tracers in Figure 13. This pressure dip cannot be seen for the lowest two Mach numbers, but the surface flow tracers indicated that the horseshoe vortex is relatively small and weak at these conditions. Local minima can be seen in the wake pressures, similar to those seen in Figure 17a; though such a minimum is not visible for M_8=0.5, the trend of the figure suggests that it is simply too close to the jet to be measured by the pressure transducers which are a finite distance away.

As the nozzle orientation is gradually altered from 0° to 90° in Figure 17-27, the pressure rise along the –x axis as the crossflow approaches the jet is reduced since the pressure taps are moved out of the stagnation region. Eventually the measurements transition to a drop in pressure starting at approximately ?=52.5° or ?=60°, depending upon the value of J or M_8. Thus a pressure drop can be seen from the interaction effects while the pressure taps are still oriented to the upstream half of the jet exit plane, which is prior to what would typically be considered the wake. This also was evident in Figure 14b, where it could be observed that the pressure coefficients transitioned from positive to negative at approximately ?=55°. While the pressure remains elevated up through ?=52.5° or ?=60°, the small dip in pressure just upstream of the jet appears to remain at about the same radial distance from the jet exit. Again, this is consistent with the oil flow tracers in Figure 13, which show that the horseshoe vortex maintains approximately the same size until the wake of the jet is reached. This is additional circumstantial evidence that this mild drop in pressure just prior to the stagnation of the crossflow corresponds to the separation point of the largest (darkest, in Figure 13) horseshoe vortex.

Similarly, as ? increases from 0° to 90° in Figures 17 through 27, the pressure drop in the wake of the jet (which actually is in a direction of 180° to 270° since this is along the ray of pressure taps in the +x direction) alters its appearance. The strongest pressure drop does not necessarily lie in the 180° direction (i.e., directly behind the jet plume), as was apparent in Figure 14b (and is even clearer in Figure 28 below). As the nozzle orientation is rotated from 180°, the lowest observed pressure may actually decrease further before beginning to rise as ? moves the pressure taps toward the sides of the jet. The local minima in the wake pressures move to different radial distances from the jet exit as ? is changed, unlike the minima seen in the stagnation region. This is consistent with the supposition that these wake minima are tied to the presence of wake vortices or the liftoff of the horseshoe vortices, since the surface flow tracers in Figure 13 showed that the structures in the wake varied significantly with ? whereas the horseshoe vortices in the stagnation region maintained a relatively constant breadth prior to reattachment in the wake.

The variation of the pressure coefficients measured by the annulus of pressure taps surrounding the exit orifice of the nozzle is shown in Figure 28. As in the previous figures, Figure 28a shows the changes in the pressure trace as J is varied while M_8=0.8

and Figure 28b shows pressure traces as M_8 is varied while J=10.2. Each pressure trace was measured from a single wind tunnel run with the nozzle installed at an orientation of 0°. Differences in the annular pressures for other nozzle orientations were within the uncertainties stated in section 4.3.2, of course, since those uncertainties for the flowfield nonuniformities were derived in part from these measurements at different nozzle orientations. As can be seen, the same basic appearance is visible for all cases, but as either J or M_8 is reduced the magnitude of the pressure difference between the stagnation region and the wake also drops. However, the undulations in the jet's wake are different for each case, which is consistent with the oil flow tracers in Figure 13 showing that the structure immediately behind the jet exit varied with the flowfield conditions. The same phenomena that contributes to this wake structure probably explains the local minima in the wake pressures in Figures 17 through 27. In those figures, the local minima in the wake were found to shift radially as the flowfield conditions were changed; here it is observed that they similarly shift angularly.

The collection of pressure data in Figures 17 through 28 may be compared directly to surface pressures predicted by numerical models. Because the pressure traces shown here, when used in conjunction with the surface flow tracers in Figure 13, were used to identify the presence of distinct flowfield structures generated on the flat plate by the interaction, the validation efforts need not be a simple rote comparison of pressure coefficients. A demanding test of any computational model would be to identify similar structures in such numerical results and verify that they are present in the same locations as measured here. Since the current data include such measurements for a variety of flowfield conditions, trends for alterations in J or M_8 can be validated.

The final piece of available data for the flat-plate-instrumented nozzle is the surface pressures measured by the instrumented window blank while the jet was operating. This is the same window blank used for the tunnel empty measurements detailed in section 4.1, which in this case was mounted in the side wall opposite the location of the jet. Figure 29 displays the resulting surface pressures, where Figure 29a shows the pressure traces as J is varied while M_8=0.8 and Figure 29b shows pressure traces as M_8 is varied while J=10.2. Tunnel empty pressure traces are shown as well for reference; these data are the same as found in Figure 10. In Figure 29a, only one tunnel empty curve needs to be shown since all data is with M_8=0.8; Figure 29b includes four tunnel empty curves, one for each M_8 shown. From the tunnel empty measurements, the uncertainty bounds for the present data can be estimated as ±0.005 c_p including the flowfield nonuniformity effects. However, the nonuniformity estimated by the tunnel empty measurements does not include additional nonuniformities created by the jet plume, so the actual uncertainty may be higher. It is unlikely to exceed the ±0.03 c_p value found in the near-field of the jet. This is too small a value to be shown in the figures. The effects of the greater tunnel blockage due to a stronger jet are readily apparent in Figure 29a, where more pressure drop across the test section occurs for larger values of J. Note that flow visualization has shown that the jet does not reach the wall opposite from the flat plate from which it exhausts,[36] so jet impingement cannot be a factor in the pressure distribution on the window blank. The larger pressure drop at higher Mach numbers shown in Figure 29b is due to the additional blockage imposed by the presence of the jet. Even though the jet

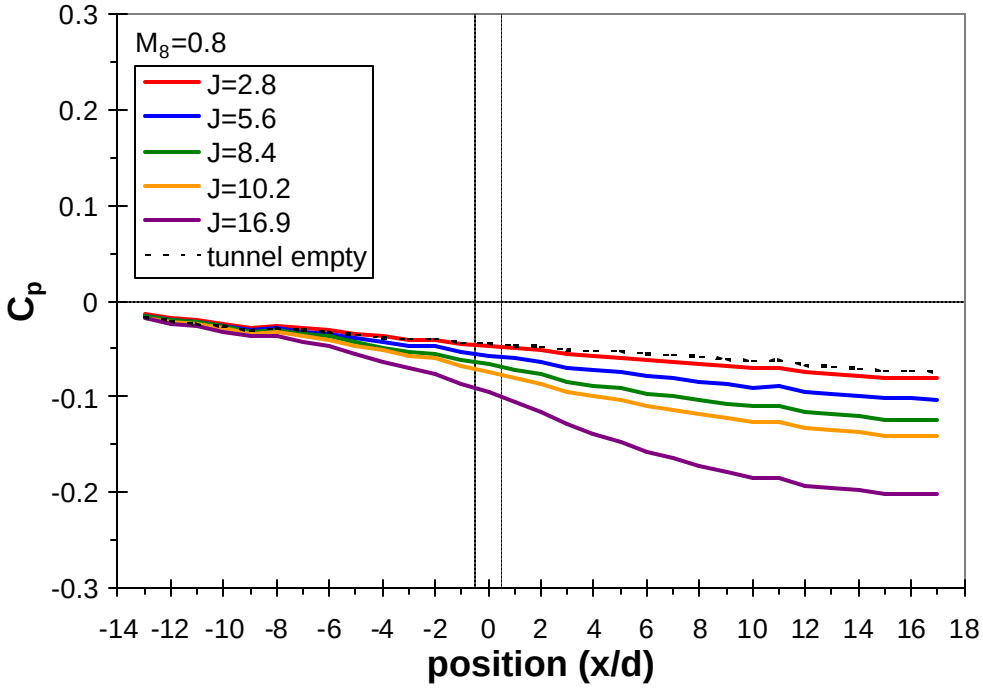

(a)

(b)

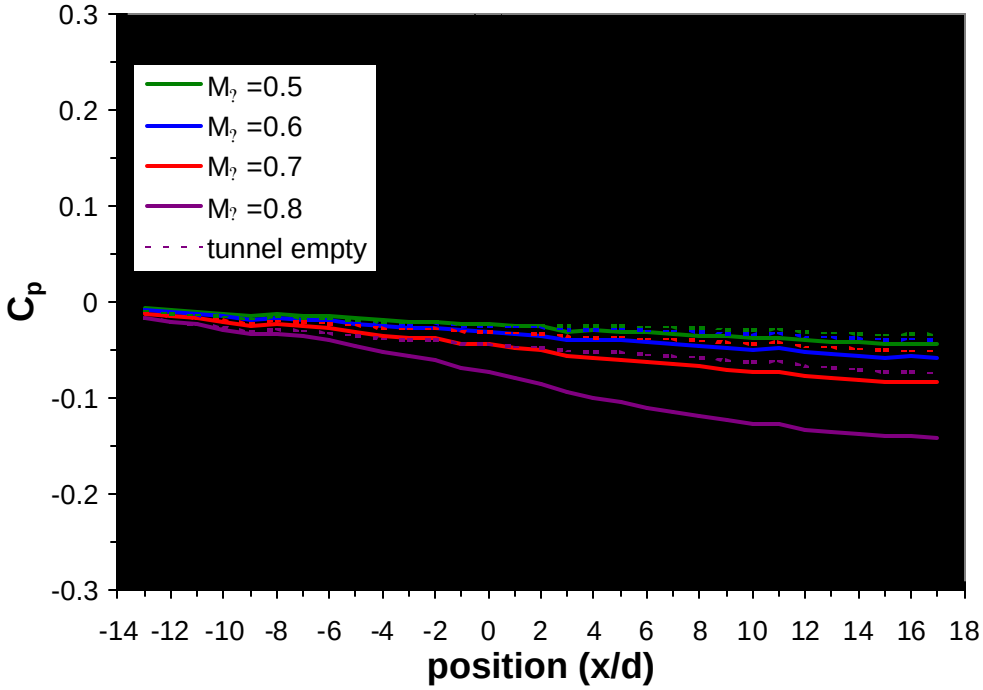

Figure 29: Mean surface pressure coefficients from the instrumented window blank located on the side wall opposite the jet position; (a) varying J while maintaining a constant M_8=0.8; (b) varying M_8 while maintaining a constant J=10.2.

penetration is relatively unvarying while J remains constant at 10.2,[36] at higher M_8 choking effects are more prevalent.

4.4 Nozzle Wall Surface Pressure Measurements

4.4.1 Initial Measurements

An interesting phenomenon to explore is the possibility of flow separation within the nozzle itself. This may occur because the exit pressure of the Mach 3.73 jet will be low as a result of the large expansion ratio, while the static pressure of the crossflow will remain relatively large because of the subsonic Mach number of the freestream. Depending upon the selected nozzle stagnation pressure and freestream static pressure, the jet may be either underexpanded or overexpanded. If overexpanded, the backpressure on the nozzle may be sufficient to create shock-induced separation within the nozzle itself. Furthermore, this separation may be highly asymmetric despite the axisymmetric design of the nozzle, because the pressure will vary around the exit orifice of the nozzle due to jet-in-crossflow effects.

Studies of nozzle flow separation in free jets are a useful investigative tool for the behavior in a jet-in-crossflow scenario. Although the work of both Romine[19] and Schilling[10] indicates that a Mach 3.73 free jet is unlikely to experience internal separation at the nominal operating conditions (case 1), neither analysis accounts for asymmetries in the backpressure. The backpressure around the exit plane of the jet will vary due to the jet-in-crossflow interaction, and this may locally induce internal separation where the backpressure is higher; i.e., in the stagnation region at the upstream edge of the jet exhaust. Furthermore, it is more likely that internal separation will occur as the nozzle stagnation pressure is reduced from the nominal conditions of P_{0j}=4.96 MPa, which is analogous to increasing the backpressure, or lowering J, which would occur during the initiation or termination of a rocket burn.

These possible flow separation effects can be investigated using the nozzle with internal surface pressure instrumentation. Although, as discussed previously, these pressure measurements may experience biases due to the large size of the pressure taps with respect to the nozzle flow length scales, they should still be useful in identifying the presence of flow separation. Flow separation can be identified by a sudden increase in surface pressure along the nozzle wall, rather than the steady decline in pressure associated with a nozzle expansion. Thus, while these pressures are likely to experience a bias owing to the tap size, it should be possible to identify separation regions based on changes in the surface pressure even if their magnitude is in error.

The internal surface pressures along a line on the upstream edge of the nozzle are shown in Figure 30 for seven sets of flowfield conditions. The axial length l is measured from the throat of the nozzle. This portion of the nozzle flow will exhaust onto the wind tunnel centerline and will experience the maximum backpressure due to the stagnation of the freestream against the jet plume (as shown at 0° in Figure 28). As in previous figures, two figures are shown, one to display the effects of varying P_{0j} while M_∞ remains

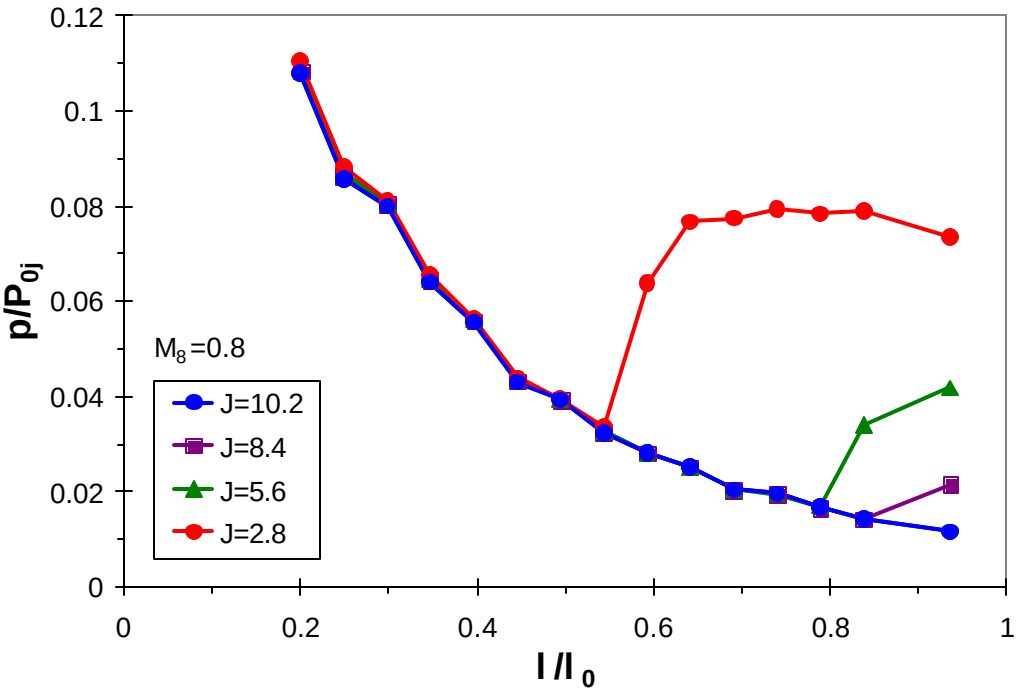

(a)

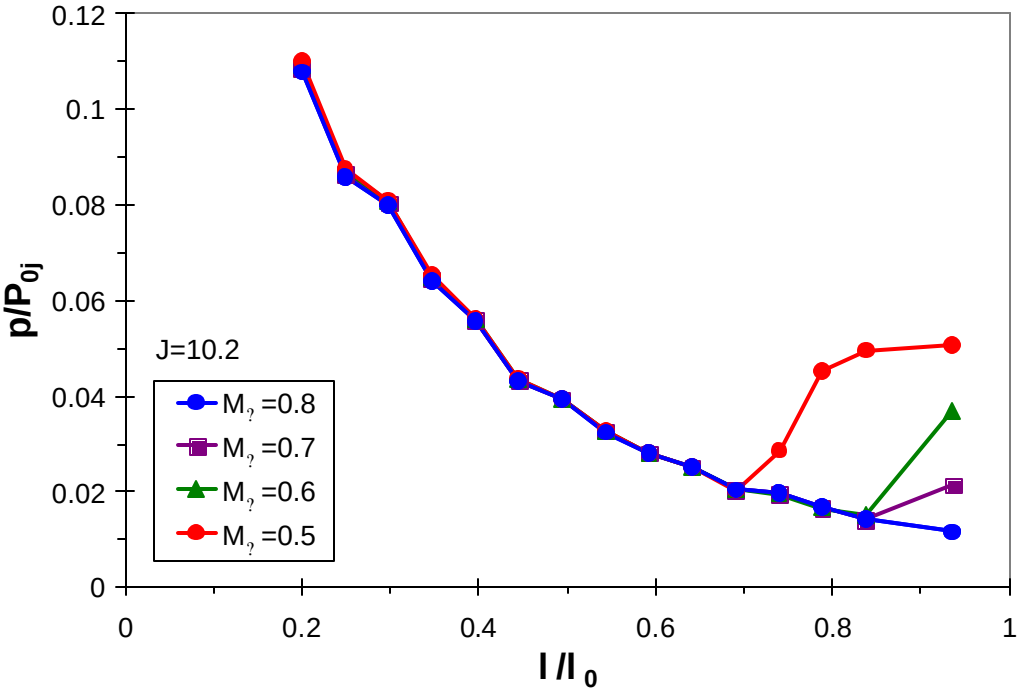

(b)

Figure 30: Mean nozzle internal surface pressures along a line on the nozzle's upstream edge; (a) varying J while maintaining a constant M_8=0.8; (b) varying M_8 while maintaining a constant J=10.2.

constant at 0.8 and the other to show the effects of varying M_∞ while J is constant at 10.2. Case 5, where J=16.9, is not shown because no separation occurs for either case and it is therefore identical to the nominal conditions of case 1. Pressure data were combined from two different wind tunnel runs, one of which rotated the nozzle by 180° to interleave the pressure taps for greater spatial resolution. This accounts for the slight waviness observed in some of the pressure traces, which resulted from a slightly non-uniform expansion through the nozzle as opposed to run-to-run variations and will be discussed at length in section 4.4.2 below.

Despite the small nonuniformity due to the pressure tap interleaving, Figure 30 shows that flow separation is clearly indicated by a distinct rise in surface pressure as the nozzle exit is approached. The magnitude of the pressure rise and the length of the separation zone both increase for decreasing J, which is analogous to raising the backpressure for a fixed P_{0j}. Precisely locating the separation point is limited by the poor spatial resolution offered by the pressure taps in such a small nozzle. Figure 30 demonstrates that despite this difficulty and any bias in the pressure measurements due to the relatively large diameter of the taps, it is possible to identify flow separation within the nozzle.

It is evident in Figure 30 that no separation occurs at the nominal flow conditions of J=10.2 and M_∞=0.8, despite the increase in backpressure above the freestream static pressure resulting from the jet-in-crossflow interaction. However, as either J or M_∞ is reduced, separation is observed, where smaller values of J or M_∞ produce a larger separation region and a higher separation pressure. Reducing M_∞ from its nominal value of 0.8 induces separation despite the constant J=10.2 because the smaller value of M_∞ demands a proportionally larger value of p_w/p_e to maintain the value of J. Hence, the backpressure increases sufficiently to induce separation. The parameter most strongly controlling the location of the separation point is the pressure ratio P_{0j}/p_b, where p_b is the local backpressure, but this value varies around the nozzle perimeter due to the jet-in-crossflow interaction. The use of J and M_∞ to describe the flowfield is convenient because it determines the p_b distribution.

4.4.2 Uncertainty Analysis

To examine the repeatability of the measurements, the nominal flow conditions were duplicated in four additional wind tunnel runs with the internally-instrumented nozzle aligned to the 0° orientation. The data examined for this analysis were not interleaved with additional runs in which the nozzle was oriented to 180°; this eliminated the possibility that nozzle nonuniformity issues would contribute to the repeatability. The pressure measurements were found to have an estimated mean repeatability of 2×10^{-5} p/P_{0j} and never more than 4×10^{-5} p/P_{0j} (as before, determined as the 95% confidence interval using Student's t-distribution). The extreme repeatability of these measurements is because they are given normalized to P_{0j}, which is the only significant parameter in producing the wall pressure distribution in an unseparated supersonic nozzle when the nozzle geometry and gas composition remain fixed. Therefore the variations in P_{0j} that naturally result from experimental control of the pressure regulator are removed from the

data. However, a separated nozzle flow additionally will be dependent on the parameters governing the crossflowing freestream, since these will determine the backpressure experienced by the nozzle. Pressures in the attached region of the nozzle are highly repeatable as indicated, but the separated pressures will be subject to greater variability.

As is always the case, instrumentation uncertainties will be present in the pressure transducer measurements. Because the nozzle wall pressures can rise to as large as 600 kPa (85 psia) at the pressure tap closest to the nozzle throat for the highest pressure conditions, a ±700 kPa (±100 psi) PSI ESP module was used for the two rays of pressure taps. The remaining taps on the annulus near the jet exit (see Figure 7b for a sketch of the pressure tap locations) were placed on a ±100 kPa (±15 psi) transducer module since the pressures near the jet exit will be much lower. Assuming that the total instrumentation uncertainty resulting from the transducers, amplifiers, filters, cables, etc, totals 0.25%, the pressure uncertainty for those taps using the ±700 kPa module is at most ±0.005 p/P_{0j} and will be reduced from this value as P_{0j} increases. Pressure taps connected to the ±100 kPa module will have an instrumentation uncertainty of at most ±0.001 p/P_{0j}. These worst-case values occur for the lowest value of P_{0j} tested.

Analogously to the flat plate measurements, it is expected that the separated nozzle wall pressure distributions will collapse if values of J and $M_{¥}$ are identical regardless of alterations in p_w or P_{0j}. To confirm this, pressure data on the nozzle wall were acquired along the upstream edge of the nozzle wall for three different values of P_{0j} at J=5.6 and $M_{¥}$=0.8 and are presented in Figure 31. At these flowfield conditions, the nozzle flow is separated and thus P_{0j} alone is insufficient to collapse the nozzle wall pressures; J and $M_{¥}$ are additionally required to ascertain the backpressure. As did the earlier flat plate pressure measurements, the nozzle wall pressures collapse for identical values of J and $M_{¥}$.

Flowfield nonuniformities may be present in the nozzle flow in similar fashion to the nonuniformity discovered on the flat plate. The waviness in the nozzle expansion pressure traces evident in Figure 30 suggests that this is indeed the case, where the interleaving of data from two nozzle orientations 180° opposed creates a similar effect to the undulations seen on the flat plate in Figure 16b. To investigate further, Figure 32 shows pressure traces at four different nozzle installation angles, denoted by ?, each acquired with the nominal flowfield conditions for which no nozzle flow separation occurs. Data from the two different rays of pressure taps are shown independently rather than interleaving them as in Figure 30. One ray is termed the uniform ray and the other is the staggered ray. The uniform ray, as its name indicates, is the ray of eight equally spaced pressure taps, shown on the right in Figure 7b. The staggered ray, shown on the left in Figure 7b, is offset from the uniform ray by one-half a tap spacing. The figure very clearly shows that all pressure measurements acquired with the uniform ray overlie one another while all those measurements acquired with the staggered ray form their own pressure trace. This is true regardless of the selection of the nozzle installation angle. From this information, it is straightforward to conclude that the nonuniformity is created by the nozzle itself and does not result from the crossflow into which it exhausts. Neither is the nonuniformity produced by the jet stagnation chamber or its gas supply, since neither the crossflow nor the stagnation chamber rotate with the nozzle.

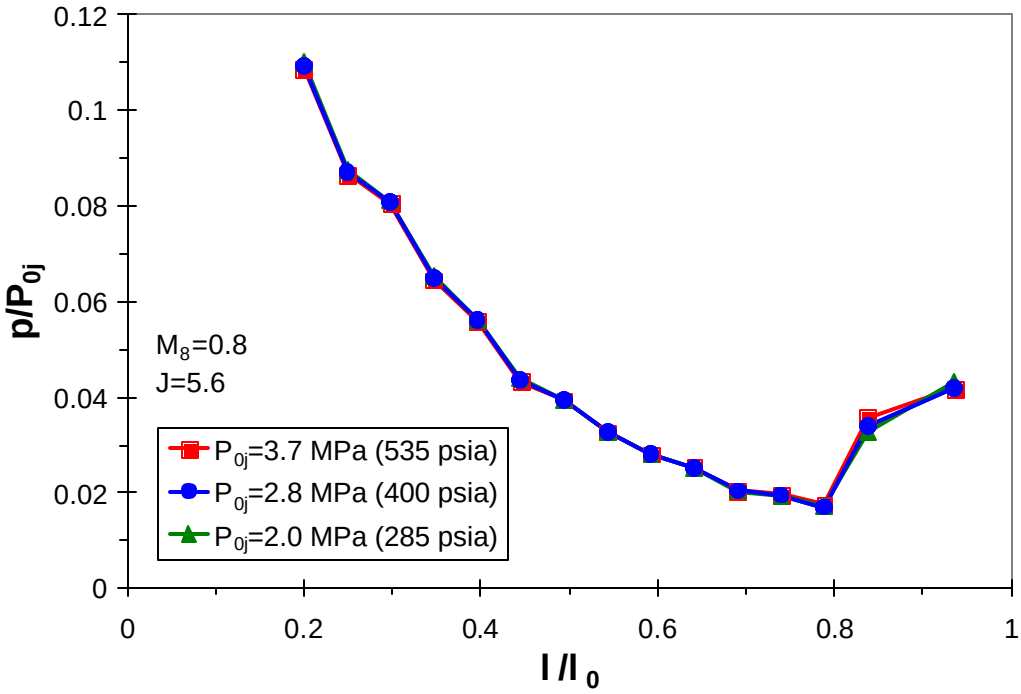

Figure 31: Collapse of the mean surface pressure coefficients along the upstream edge of the nozzle wall for a separated nozzle flow where M_8=0.8 with P_{0j} and P_w varied to maintain J=5.6.

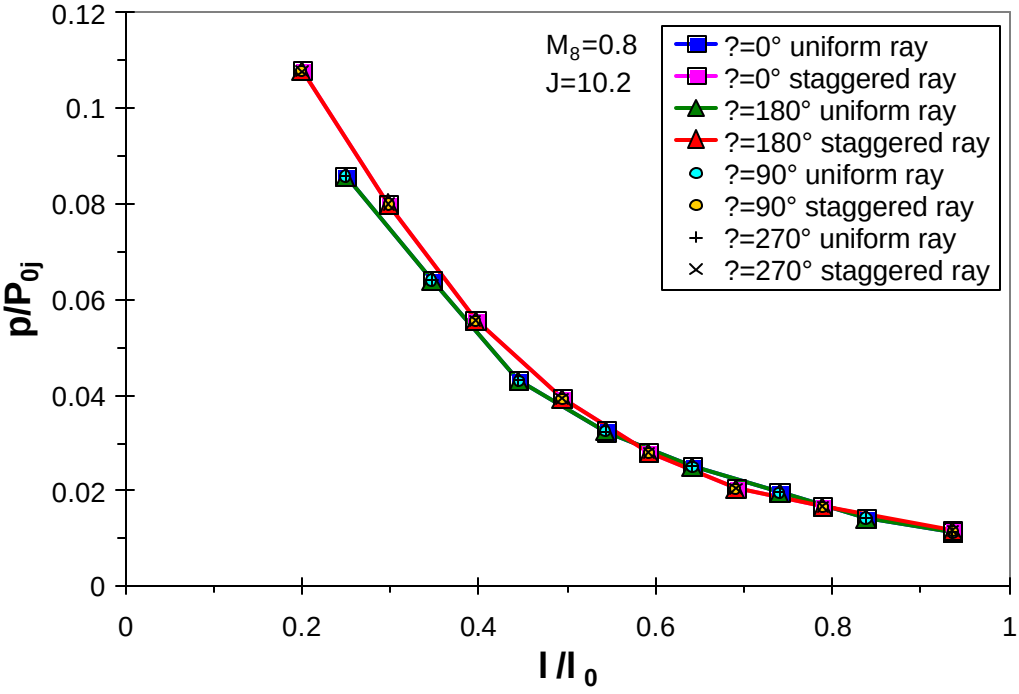

Figure 32: Nonuniformity of the nozzle flow as shown by mean wall surface pressures along the two rays of pressure taps, one termed the uniform ray and one the staggered ray. Data are shown for four different nozzle installation angles.

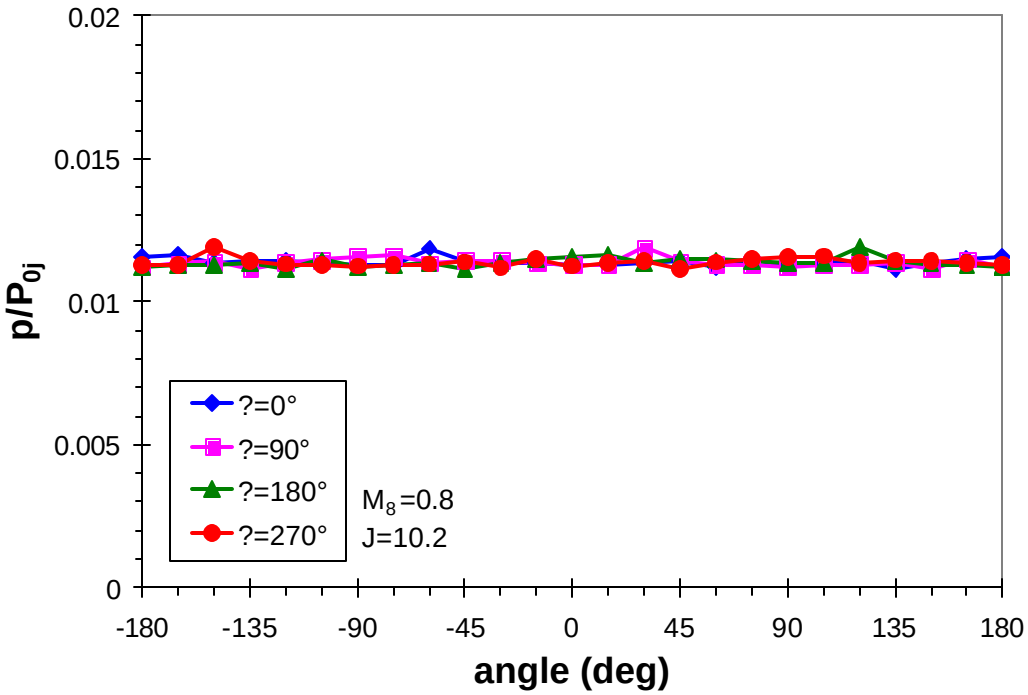

Figure 33: Mean nozzle wall surface pressures measured with the circumferential ring of pressure taps near the nozzle exit plane, measured at four different nozzle installation angles.

Figure 33 provides further evidence that this is the case by displaying the pressures measured with the annulus of taps near the nozzle exit plane. They are shown for four different nozzle installation angles. Regardless of nozzle orientation, the pressures are not significantly different. This is consistent with Figure 32, which showed appreciable nonuniformities prior to the exit plane of the nozzle, but the uniform and staggered rays of pressure taps converged to a single consistent pressure value near the nozzle exit. However, Figure 33 does have one distinct data point that is larger than the rest, which rotates with the nozzle and appears in the figure at every 90°. This mild discrepancy is, like the nonuniform expansion displayed in Figure 32, inherent to the nozzle and not the crossflow or the jet stagnation chamber. A burr in the pressure tap or a bias in the transducer is the most likely explanation for this single outlier.

The jet also was run in free jet mode, in which the wind tunnel was not operating. This provided a backpressure equivalent to approximately 83 kPa (12.1 psia), the atmospheric pressure in the laboratory, which was not sufficient to induce separation. The recorded pressures were found to be, as should certainly be the case, identical to the unseparated data shown in Figures 32 and 33 and thus are not shown in any additional figure.

The preceding data demonstrate that the nozzle expansion is somewhat nonuniform and that this nonuniformity is caused by the nozzle itself and not the crossflow or the jet stagnation chamber. When the nozzle was rotated 180°, this nonuniformity rotated 180°

as well, so each of the two lines of taps measured slightly different pressure distributions regardless of rotational position. This created the waviness to the interleaved data shown in Figure 30. Unfortunately it is not possible to provide data on the nature of the nonuniform expansion at angles other than 0° and 180° since pressure taps are found only at these positions. Furthermore, this nonuniformity strictly applies only to the internally-instrumented nozzle; any nonuniformity in the expansion may be different for the flat-plate-instrumented and the uninstrumented nozzles, depending upon the source of the nonuniformity and its consistency from one nozzle to another. The magnitude of the nonuniformity shown in Figures 32 and 33 will be assumed to be characteristic of any nozzle since no other means of assessing this uncertainty is available.

The simplest explanation for the nonuniformity found in the expansion of the nozzle flow is to ascribe it to machining tolerances in the nozzle; it cannot result from the mounting plate into which it is secured because the pressure traces for an unseparated flow in a supersonic nozzle would not be influenced by a non-normal installation into the flat plate. Neither does the jet stagnation chamber or the incident piping contribute since these items do not rotate with the nozzle and its nonuniform flow. However, fabrication of the nozzle contour is an unlikely culprit because the nozzles were inspected following machining and were found to be within tolerances, which were not sufficiently large to induce the observed nonuniformity. It is conceivable that once bolted into position and placed under pressure, the nozzle may deform to create the nonuniform expansion, but this seems implausible since the nonuniformity was identical after the nozzle was removed and reinstalled. Furthermore, since the nozzle is fabricated from the exceptionally strong 15-5PH stainless steel, significant deformation is improbable. It also is unlikely that biases in the transducers or the pressure taps create this problem since the pressure traces are quite uniform rather than exhibiting any tap-to-tap variability. Both rays of pressure taps were measured by the same ESP transducer module and hence referenced to the same pressure. One remaining possibility is that one of the pressure taps nearer the throat, or perhaps some other imperfection in the nozzle surface, induces a perturbation into the nozzle expansion. A small difference between the two rays of pressure taps could create the nonuniformity; in fact, the staggering of one row with respect to the other might be sufficient difference to perturb the nozzle flow differently and hence account for the nonuniformity seen in Figure 32. Moulden et al.'s study[41] provides some precedent for this. (Note that a similar argument cannot be used to explain the nonuniformity found on the flat plate, because in Figure 16b each flow streamline passes over only one pressure tap whereas in the nozzle a streamline passes over an entire row of pressure taps and hence can carry a perturbation caused by one tap to the measurement made by another tap.)

For the purposes of understanding the uncertainty created by the nonuniform expansion through the nozzle, a quantitative value must be derived from the data found in Figures 32 and 33. The best estimate possible, given the limited quantity of data around the nozzle perimeter, is to calculate the difference between the uniform ray and the staggered ray and to use this as the expected nonuniformity error. The largest error occurs closest to the nozzle throat, where the discrepancy between the two pressure traces is $\pm 0.008\ p/P_{0j}$. Near the exit plane, this value drops to below $\pm 0.001\ p/P_{0j}$. From Figure 30, it is apparent that flow separation occurs solely downstream of $l/l_0=0.5$ for all tested

conditions; in this region the nonuniformity error is never larger than ±0.002 p/P_{0j}. Which of these values is to be used for an uncertainty estimate should depend upon which pressure tap is considered.

Finally, in addition to the uncertainties discussed thus far in this section, a significant bias may be superimposed due to the large size of the pressure taps with respect to the scale of the nozzle boundary layer passing over it. This was discussed at some length in section 2.3.1, where it was determined that biases induced by the nozzle wall curvature and the velocity gradient are likely to present a significant difficulty only near the nozzle throat. The bias due to the pressure tap size remains, however, and was estimated to be no larger than ±0.01 p/P_{0j}. This estimate was extrapolated from limited information and, although it is the best possible value that can be offered, the actual pressure uncertainty may be substantially larger or smaller than this. As was stressed in the discussion of this error source in section 2.3.1, this bias error applies to measurement of the pressure magnitude but should not influence the determination of the separation point. Figure 30 clearly shows that a large rise in the wall pressure is observed where separation occurs. Any bias due to the pressure tap size would be superimposed upon this pressure rise, but the separation point is still easily determined. A much greater limitation results from the spatial resolution of the pressure measurements, since only a few pressure taps could be fit into such a small nozzle. This concern is discussed in section 4.4.3 below.

The total uncertainty estimate for the pressure measurements gathered within the nozzle results from the flow nonuniformity, the pressure tap size, and the instrumentation uncertainty. The repeatability of the measurements is three orders of magnitude smaller and can be safely ignored. The combination of errors yields a total worst-case estimate of the uncertainty in the pressure measurements as ±0.014 p/P_{0j}. This value is dominated by the estimate for the bias error induced by the pressure tap size, which is an admittedly imprecise prediction. However, even if this error were actually an order of magnitude less, the remaining uncertainty would total ±0.009 p/P_{0j}, still a substantial value. The uncertainty in the determination of the separation point is governed by the spatial resolution of the pressure taps and is discussed at length in section 4.4.3 below.

4.4.3 Detailed Measurements

Figure 30 established the maximum level of nozzle flow separation for each set of flowfield conditions, because the data shown were acquired with the nozzle oriented to ?=0° where the backpressure is highest due to stagnation of the crossflow against the jet plume. Separation was observed for every case except the nominal conditions of J=10.2 and M_8=0.8; therefore the nominal case need not be tested further since its pressure distribution is simply that of the nozzle expansion. For the remaining conditions, the asymmetry of the nozzle flow separation needs to be explored.

To determine the variation of the separation point around the perimeter of the nozzle as the backpressure changes due to the jet-in-crossflow interaction, the azimuthal angle of the pressure taps was adjusted from one wind tunnel run to the next. Pressure traces at different angles within the nozzle are shown in Figure 34 for the six sets of flowfield

conditions for which separation occurs. Data are given for only one half of the nozzle since symmetry arguments apply (the nonuniformity on the flat plate is too minor to measureably influence the nozzle separation). For each of the six plots, all but one of the curves corresponding to angles for which no separation is visible are removed to avoid redundancy. Figure 34a displays a sample set of uncertainty bars corresponding to the ±0.014 p/P_{0j} value estimated above. Since this uncertainty is dominated by biases superimposed on the entire pressure curve, it does not invalidate the separation seen near the exit, but instead simply questions the given magnitude of these separation pressures.

The backpressure experienced by the nozzle is given most closely by the pressure measurements in Figure 28, which were made on the flat plate by the annulus of pressure taps surrounding the nozzle exit. As would be expected based upon these backpressures, the largest amount of separation is found at the upstream edge of the nozzle with the separation point moving closer to the nozzle exit as the measurements are moved towards the sides of the nozzle. The J=5.6 case in Figure 34b exhibits a larger separation region at the leading edge of the nozzle than does J=8.3 in Figure 34a because it has a smaller nozzle pressure ratio. The nozzle pressure ratio is even smaller for the J=2.8 case shown in the rather crowded Figure 34c, which exhibits separation around its entire perimeter and reaches almost halfway back to the throat at its maximum. Similarly, the degree of separation at J=10.2 increases as $M_¥$ is lowered, attaining separation around the entire nozzle for the lowest value of $M_¥$.

Figure 34 exhibits the limitations in the spatial resolution of determining the separation point due to the small size of the nozzle, and hence the minimum distance at which pressure taps could be spaced. This is particularly clear in Figure 34e, where the flow is observed to be separated from ?=0° to ?=75° but no distinction can be made in the separation point because separation at each of those angles occurs between the same pair of pressure taps. Unless a substantial variation occurs in the separation point, such as in Figure 34c, the instrumentation is unable to provide much spatial detail.

The exit pressures shown in the highly separated case of Figure 34c exhibit a somewhat different trend at the downstream edge of the jet than around the rest of the jet perimeter. As the measurements move from the upstream edge of the jet at ?=0° towards the rear, the separation point consistently moves towards the jet exit and the pressure at the exit (the value at l/l_0=0.936) falls as well. This is consistent with the backpressures displayed in Figure 28a. However, the pressure trace at the downstream edge, ?=180°, shows a larger pressure than those shown at ?=165° through ?=120°; similarly, the exit pressure at ?=165° is slightly higher than that at ?=150°. Analogous behavior is shown by the ?=180° and ?=165° pressure traces in Figure 34f. For the other four cases, the exit pressures monotonically fall from the upstream edge of the jet to the end of the separation region; it is only for the completely separated cases that a disruption to this trend is observed.

The explanation lies in the backpressure traces of Figure 28. For the case J=2.8 and $M_¥$=0.8 and the case J=10.2 and $M_¥$=0.5, both of which create the completely separated cases respectively shown in Figures 34c and 34f, strong undulations in the backpressure are seen in the wake of the jet. This local increase in backpressure presumably induces

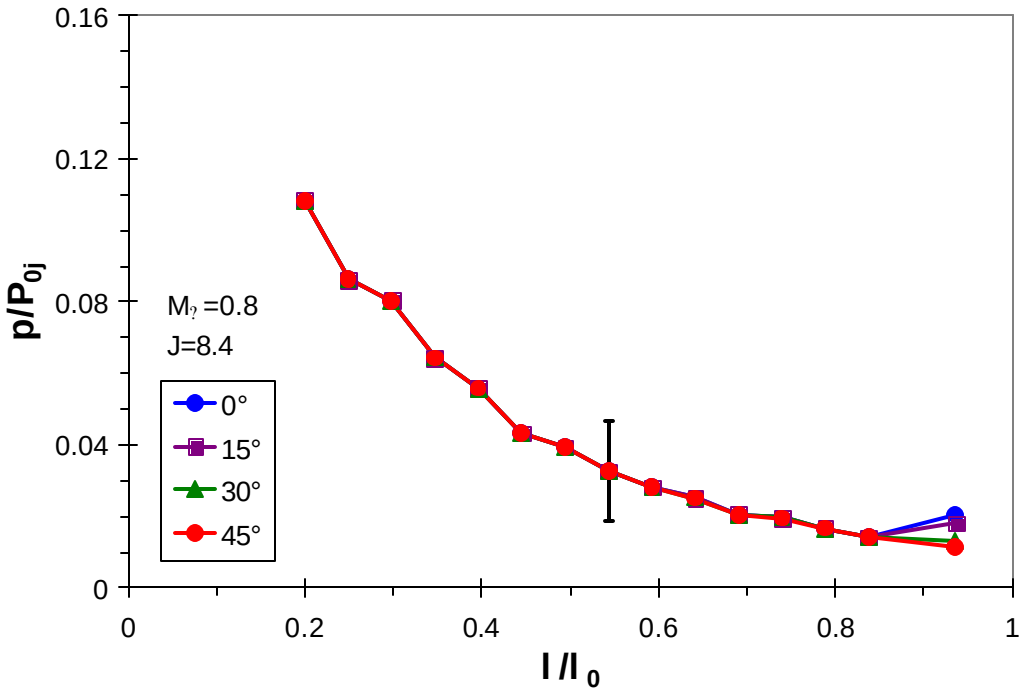

(a)

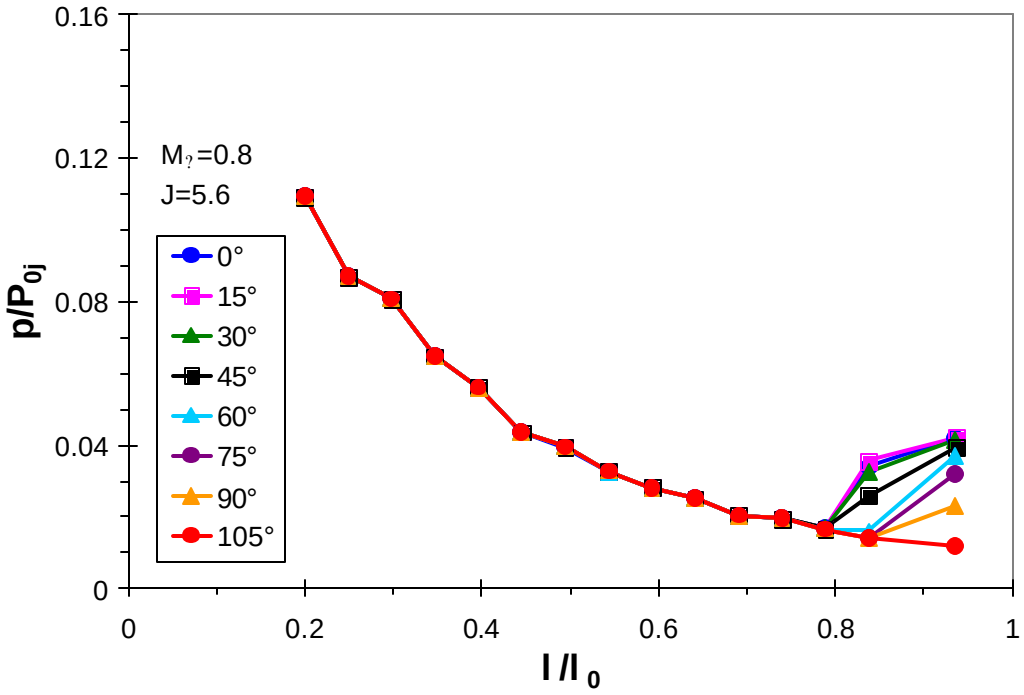

(b)

Figure 34: Mean nozzle internal surface pressures at different angles about the nozzle's perimeter. All but one of the curves corresponding to angles for which no separation is visible are removed to avoid redundancy. Plots are shown for each of six sets of flowfield conditions in (a) through (f). The upstream edge of the jet is located at 0º. (continued on the following pages)

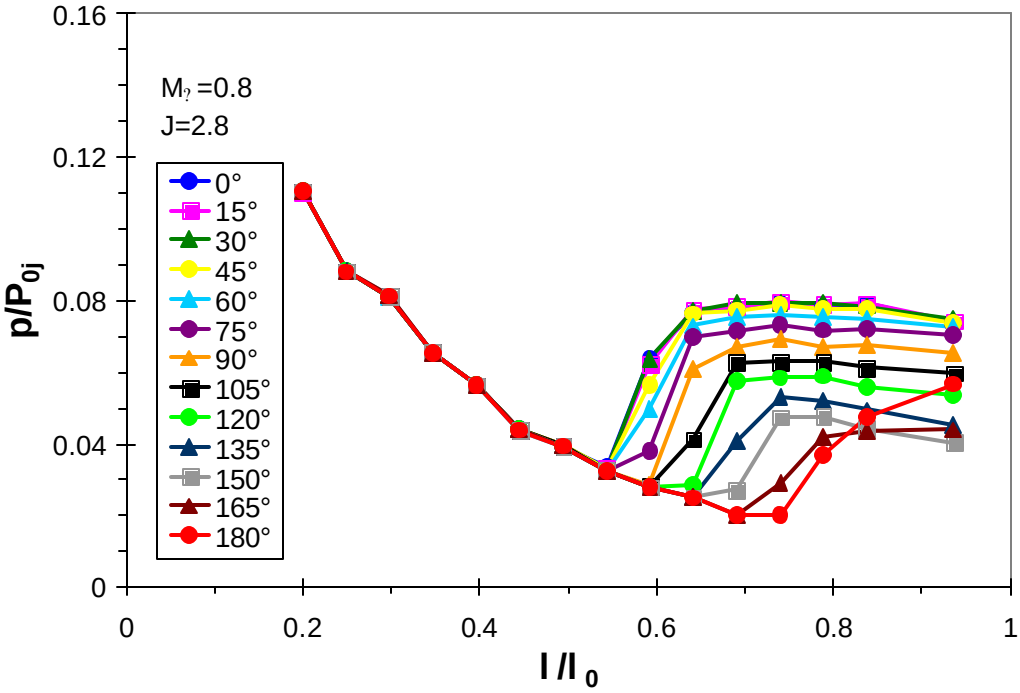

(c)

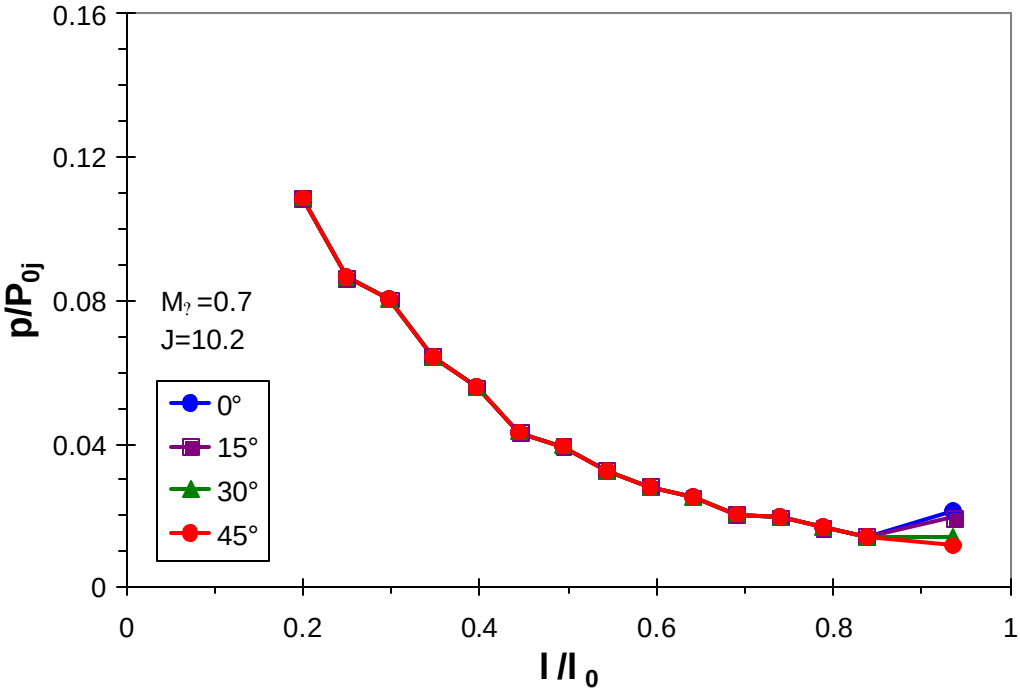

(d)

Figure 34, continued

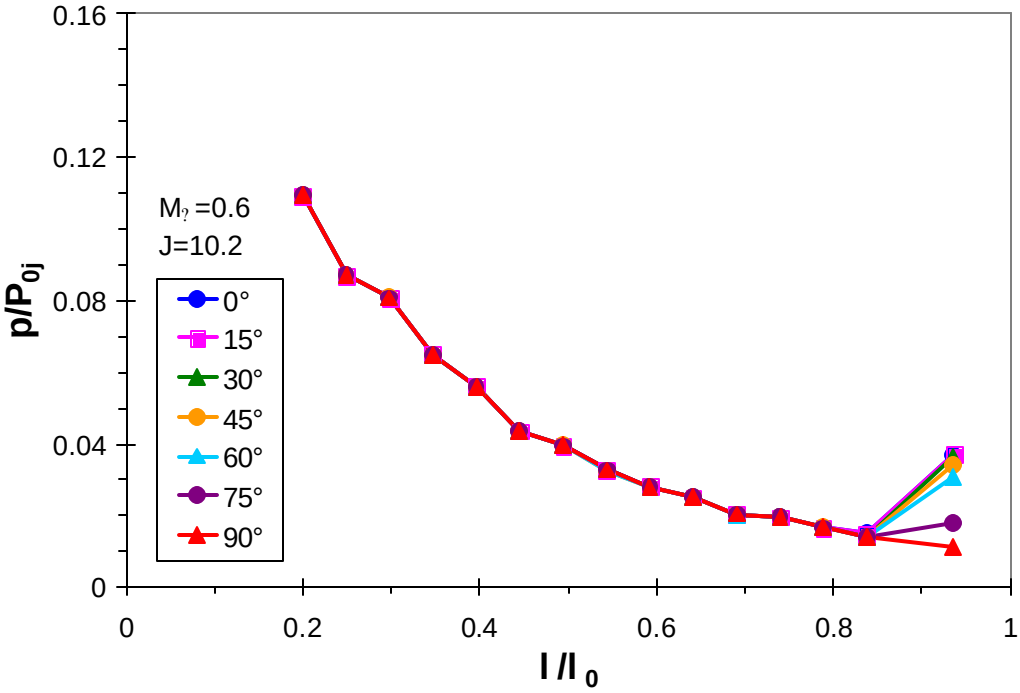

(e)

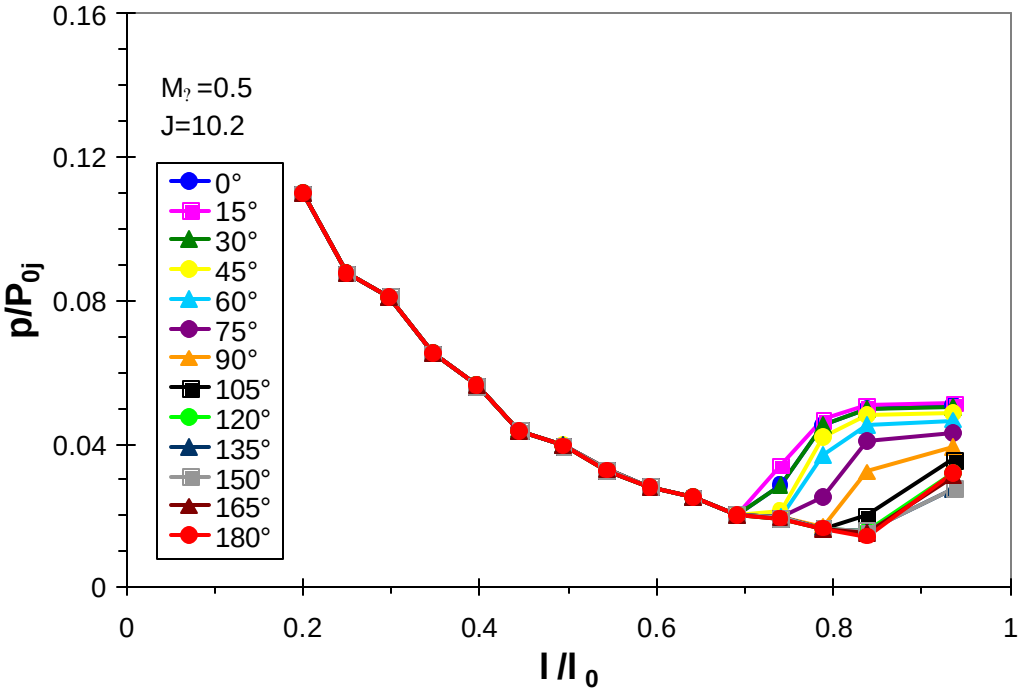

(f)

Figure 34, concluded

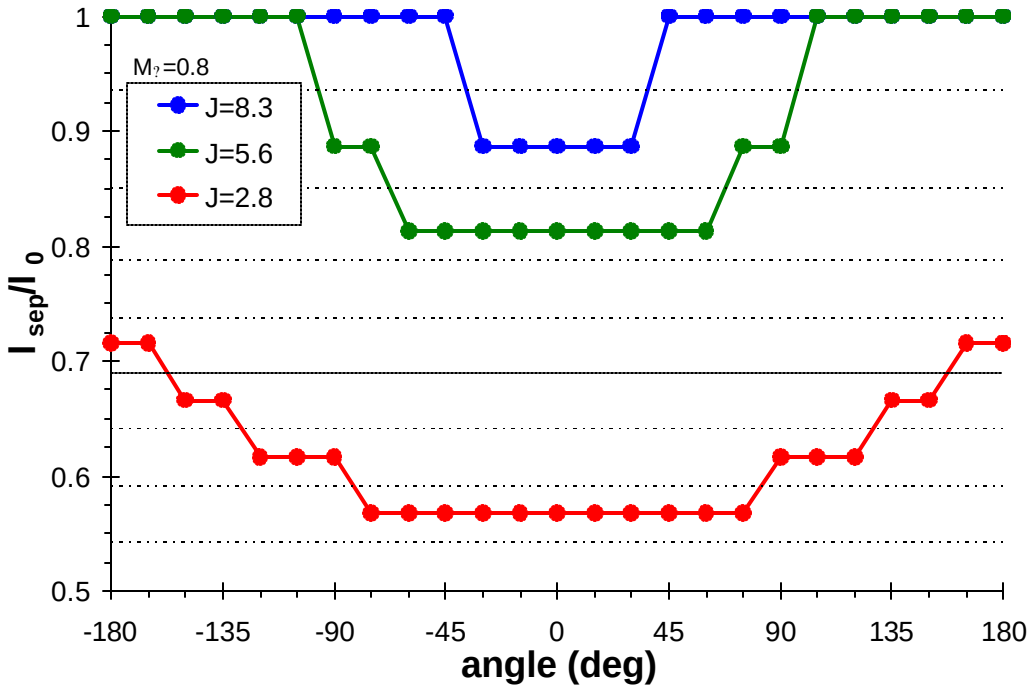

(a)

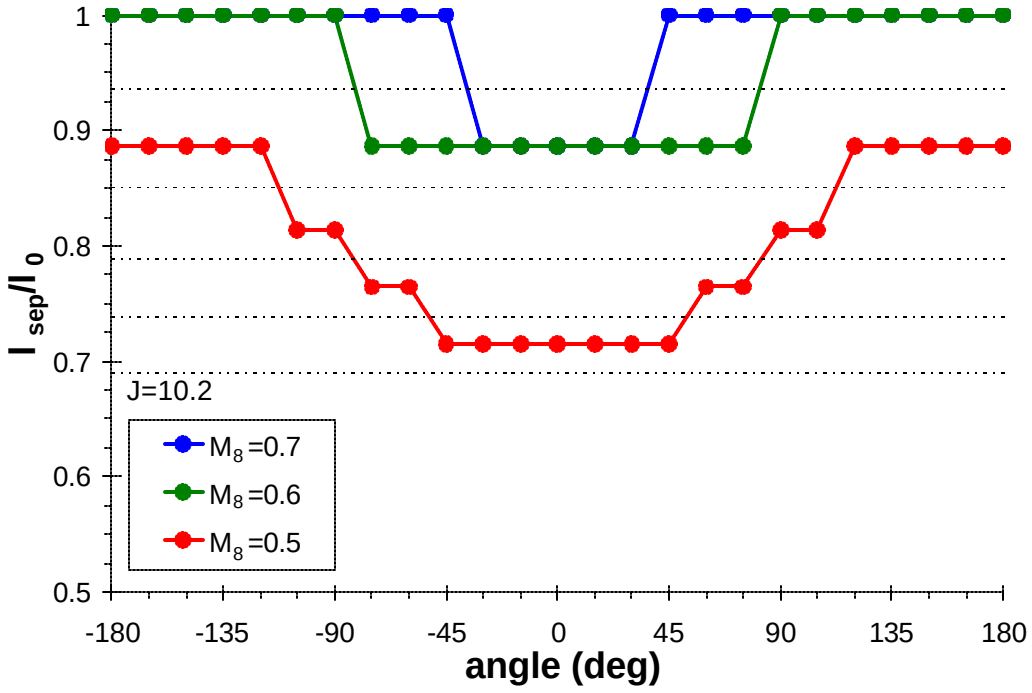

(b)

Figure 35: Flow separation lines within the jet nozzle determined from the mean surface pressure data shown in Figure 34. The horizontal dashed lines represent the limits of the spatial resolution created by the pressure tap spacing. (a) varying J while maintaining a constant M_8=0.8; (b) varying M_8 while maintaining a constant J=10.2. The upstream edge of the jet is located at 0°.

the higher exit pressures observed in Figures 34c and 34f. A corresponding movement of the separation point closer to the nozzle throat is anticipated, but probably cannot be detected by the limited spatial resolution of the pressure taps. This wake structure in the backpressure seen in Figure 28 also is visible at J=10.2 and $M_{¥}$=0.6, but the spatial resolution limits in Figure 34e probably prevent its influence from becoming evident.

A simpler method is needed to envision the shape of the separation line along the nozzle wall. One way to accomplish this is to determine the separation point from each of the pressure curves seen in Figure 34 and then to assemble them into a trace of the separation line as though the nozzle wall had been laid out flat. This is done in Figure 35 for all six cases shown in Figure 34, where Figure 35a displays the inferred separation line for cases where $M_{¥}$=0.8 and J is varied, and Figure 35b shows the separation line for J=10.2 and $M_{¥}$ varied. The separation point was defined as the location midway between those pressure taps where the pressure was observed to rise above the value associated with the nominal unseparated expansion. For virtually all data points, the separation pressure was found to be strongly in excess of the precision uncertainty of the pressure measurement, which made determining the separation point quite dependable. The horizontal dashed lines in Figure 35 represent the limits of the spatial resolution due to the distance between pressure taps. The actual separation point could occur anywhere between the two dashed lines bracketing each plotted separation point. Flowfield symmetry was invoked to reflect the data about the wind tunnel centerline and thus trace the separation line around the entire nozzle perimeter. The analysis gleaned from Figures 16, 32, and 33 provides an experimental verification of flowfield symmetry.

Displaying the nozzle flow separation data in the manner of Figure 35 provides a much clearer picture of the shape of the separation line since the clutter of Figure 34 is removed. The limitations of the spatial resolution of the pressure taps are dramatically highlighted by the coarseness of Figure 35. However, a reasonable representation of the shape of the separation line is displayed. These data probably should be considered more reliable than the pressure data that spawned them, since the pressure data is subject to vague uncertainties such as the pressure tap size bias discussed in section 4.4.2 whereas the separation data shown in Figure 35 is subject simply to the clear uncertainty range of the spatial resolution. Therefore, a more confident validation of numerical simulations may be made by comparing the shape of the separation line rather than the actual pressures.

4.5 Pressure Measurements on the Top Wall of the Test Section

To this point, all pressure measurements have been gathered with the nozzle mounted on one side wall of the wind tunnel. This is because ease of access to the pressure instrumentation is much greater on the side wall and it was found to be prohibitively difficult to conduct a large volume of pressure measurements with the nozzle mounted on the top wall. However, it is useful to make a small set of pressure measurements in the top-wall configuration to compare with those from the side wall. This activity cannot be said to be a true investigation of the tunnel nonuniformity since the boundary layer is known to be approximately 10% thinner on the top wall as compared with the side wall,

as noted in section 3.0. Thus measurements are conducted in a slightly different flowfield. Nevertheless, a comparison of one set of pressures to the other allows for a sensitivity study of the effects of small changes in the boundary layer. These measurements are additionally useful because optical flow measurements, such as the schlieren photographs reported in Reference 36 or forthcoming laser-based diagnostics, must be acquired with the nozzle installed into the top wall such that it is properly aligned with the windows. Thus a direct comparison between such optical data and the pressure data presented thus far in this document is not possible; the acquisition of a limited set of pressure measurements on the top wall will help to bridge this gap.

The primary experimental conditions for the top-wall measurements are given in Tables 5 and 6, where Table 5 shows the values acquired when using the flat-plate-instrumented nozzle and Table 6 shows the values using the internally-instrumented nozzle. No precision uncertainties are provided because at most three wind tunnel runs were conducted for any one case. Note that case 2, J=8.4 and $M_{¥}$=0.8, had runs conducted for ?=0° but not ?=90° or ?=270° with the flat-plate-instrumented nozzle. Case 5 was omitted from the internal measurements, as it was for the side-wall internal measurements in section 4.4, because no separation is observed for this case and the normalized results are identical to case 1.

The top-wall runs were conducted with the same fundamental values as in previous runs without accounting for the slight alteration in flowfield; that is, parameters such as P_0 and P_{0j} were constant rather than J and $M_{¥}$. Since the jet penetration was slightly different, J was altered, which, for some flowfield conditions, changed the choking of the wind tunnel and thus shifted $M_{¥}$. For the thinner boundary layer on the top wall, it is anticipated that the jet penetration would be greater and hence J would be higher and $M_{¥}$ lower. This is in fact what Tables 5 and 6 show, although the decrease in $M_{¥}$ scarcely exceeds the precision uncertainties found in Table 1.

4.5.1 Flat Plate Measurements

Figure 36 shows pressure measurements gathered with the flat-plate-instrumented nozzle aligned at a nozzle orientation of ?=0°. These data consist of a single wind tunnel run per condition rather than interleaving data from two runs with the nozzle 180° opposed. As previously, the runs for varying J and constant $M_{¥}$ are shown in Figure 36a and the runs for varying $M_{¥}$ and constant J are shown in Figure 36b. The figures additionally show the analogous data from the side-wall measurements of Figure 17, which are displayed as dashed black lines alongside the colored lines representing the current top-wall data. It is readily apparent that no significant difference exists between the top-wall and the side-wall pressure traces, since the black dashed lines for the side-wall measurements typically overlie their colored top-wall counterparts. Certainly whatever small differences are present remain within the uncertainty bounds displayed in Figure 36a (which are derived from the analysis in section 4.3.2 above).

Data acquired at ?=90° are shown in Figure 37. These data are interleaved from wind tunnel runs at ?=90° and ?=270°, which returns the waviness to the pressure traces first

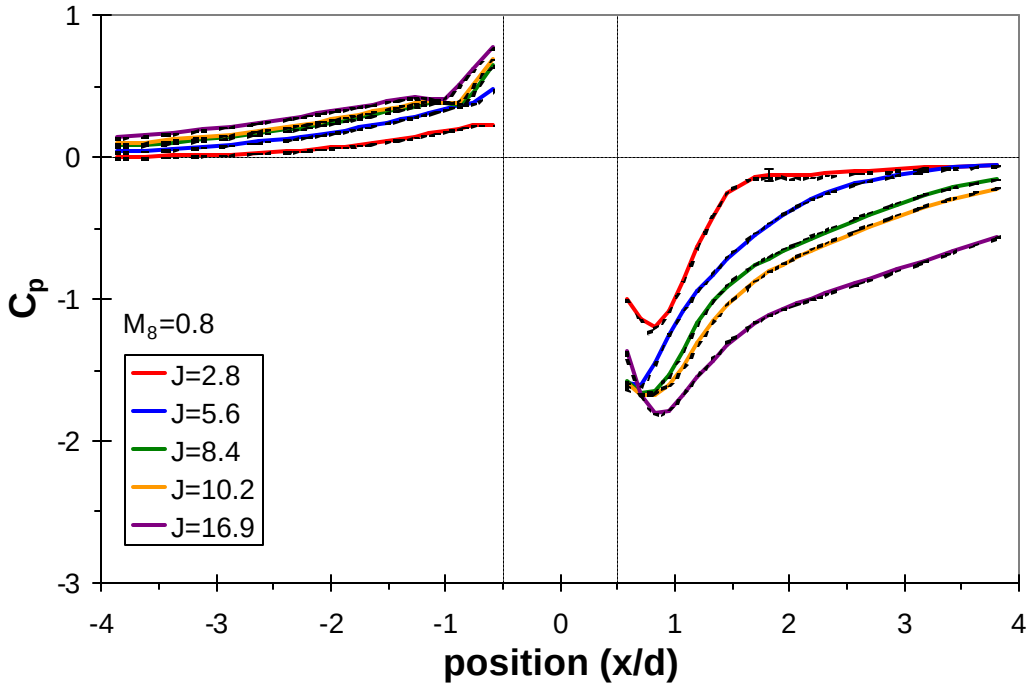

(a)

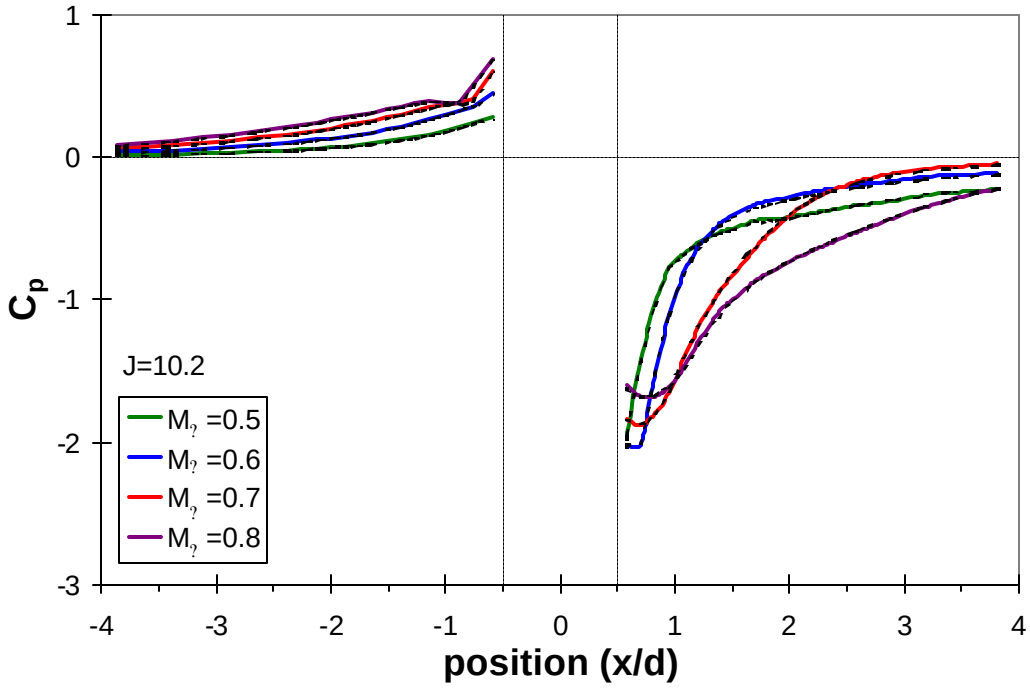

(b)

Figure 36: Mean surface pressure coefficients with the nozzle mounted on the wind tunnel top wall at an orientation of ?=0°. The black dashed lines represent the previous side-wall pressure measurements. (a) varying J while maintaining a constant M_8=0.8; (b) varying M_8 while maintaining a constant J=10.2.

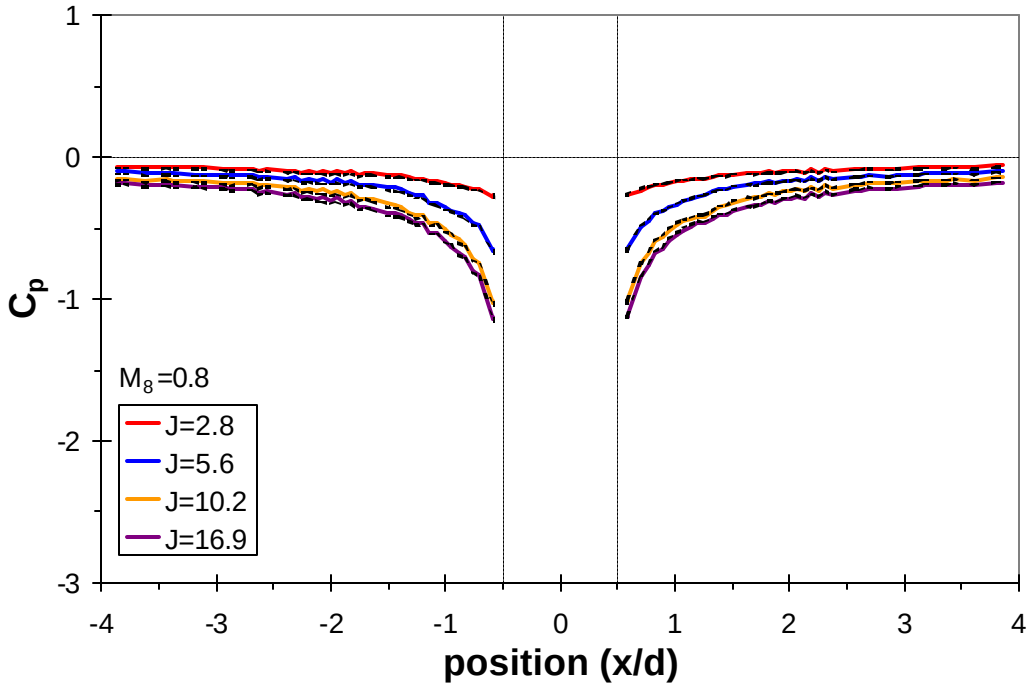

(a)

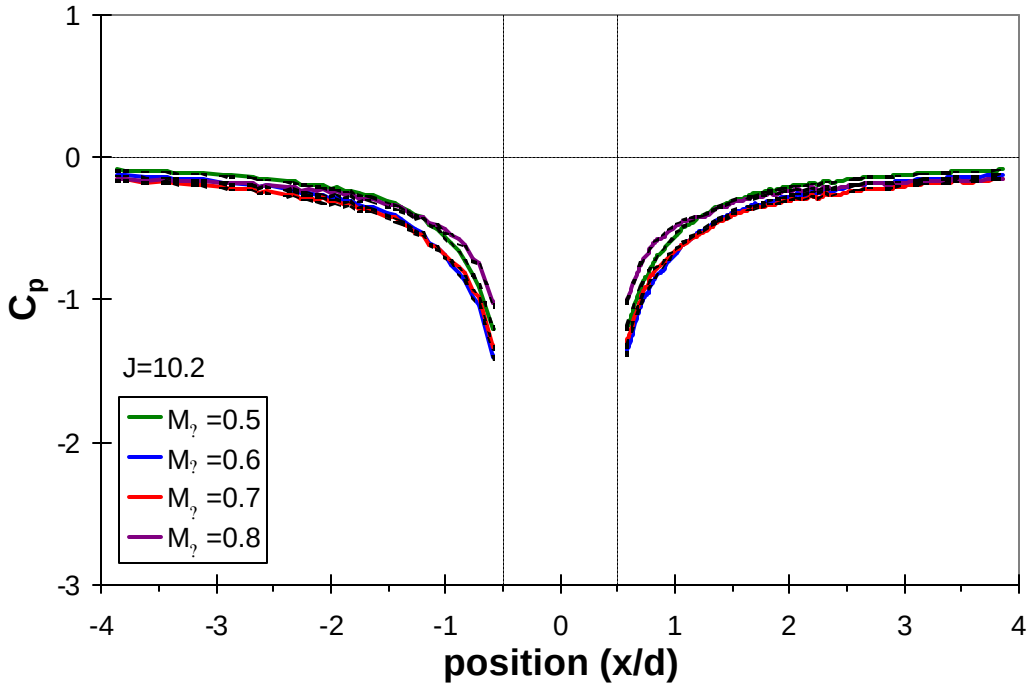

(b)

Figure 37: Mean surface pressure coefficients with the nozzle mounted on the wind tunnel top wall at an orientation of ?=90°. The black dashed lines represent the previous side-wall pressure measurements. (a) varying J while maintaining a constant M_8=0.8; (b) varying M_8 while maintaining a constant J=10.2.

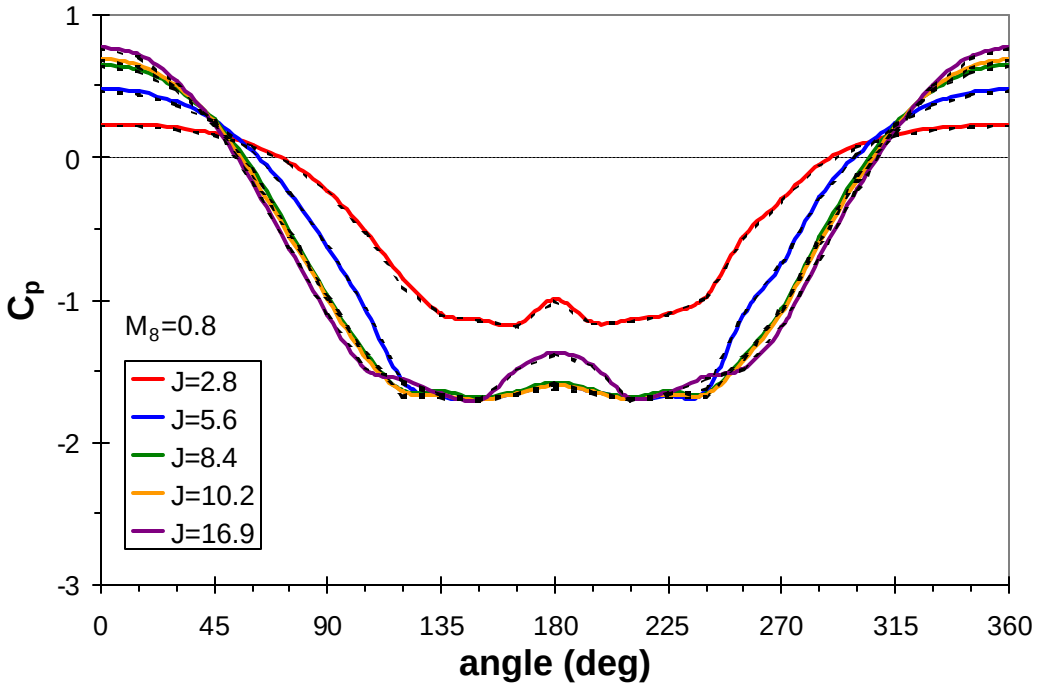

(a)

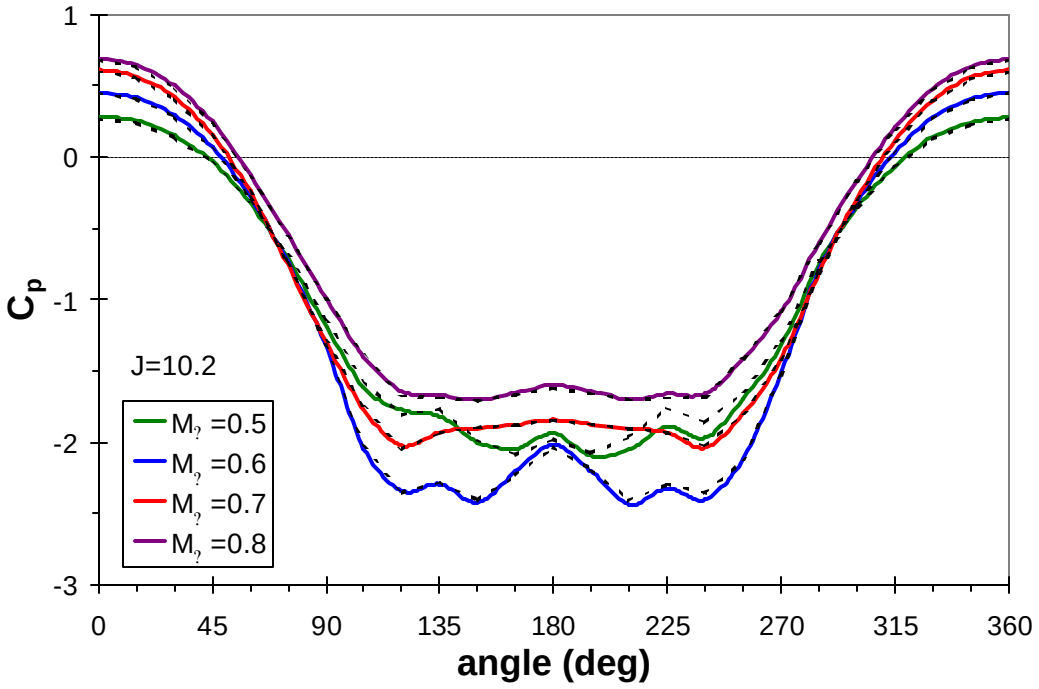

(b)

Figure 38: Mean surface pressure coefficients around an annulus surrounding the jet exit with the nozzle mounted on the wind tunnel top wall. The black dashed lines represent the previous side-wall pressure measurements. (a) varying J while maintaining a constant M_8=0.8; (b) varying M_8 while maintaining a constant J=10.2.

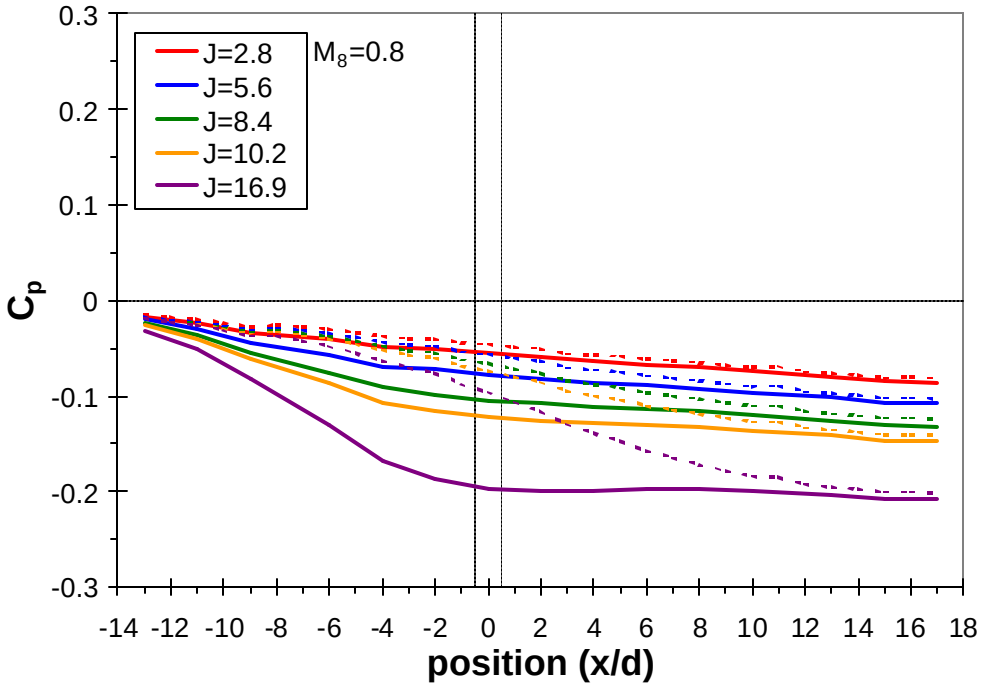

(a)

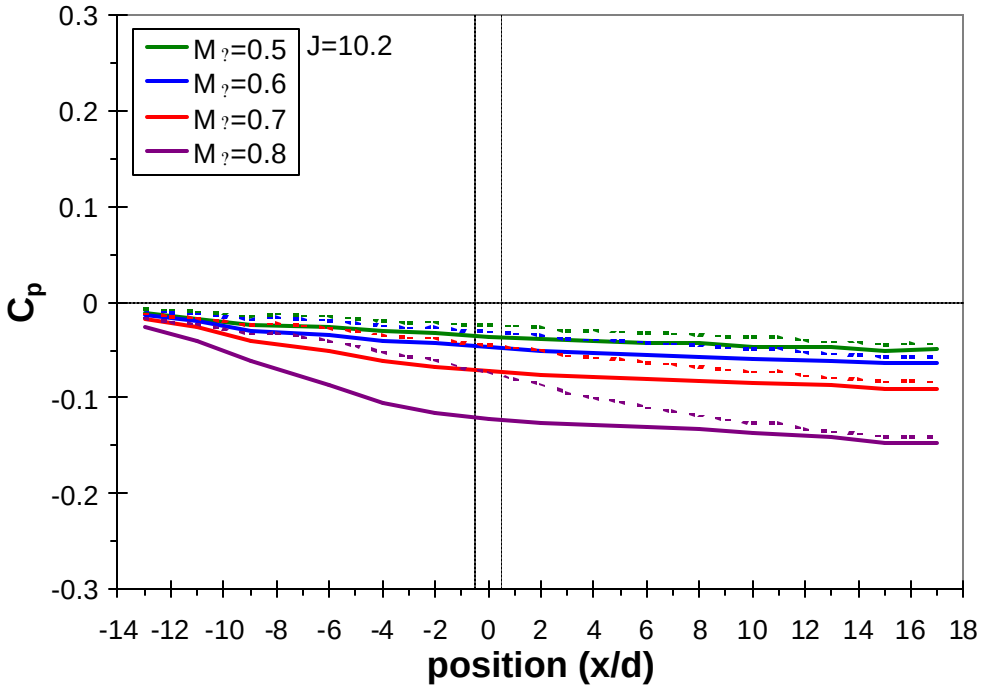

(b)

Figure 39: Mean surface pressure coefficients from the side-wall instrumented window blank with the jet mounted on the top wall. The thinner dashed lines show the data where the jet was mounted on the side wall, first shown in Figure 29. (a) varying J while maintaining a constant M_8=0.8; (b) varying M_8 while maintaining a constant J=10.2.

seen in Figure 15. As in Figure 36, the matching side-wall pressure measurements are shown as black dashed lines, and again these are not appreciably different from the top-wall pressures. Since the undulations in the new traces are similar in magnitude to those shown in Figure 15, and analyzed more closely in Figure 16b, this indicates that any contribution by a freestream nonuniformity is no stronger on the top wall than on the side wall. The contribution due to the flat plate nozzle insert is, of course, identical since the same nozzle is used.

Figure 38 shows the pressures on an annulus surrounding the jet exit, again with the side-wall measurements displayed alongside. This figure contains the only pressure difference between the top wall and the side wall that exceeds the measurement uncertainty. At flowfield conditions of J=10.2 and $M_{¥}$=0.5, the top-wall measurements are about 0.15 c_p lower than for the side wall in the vicinity of ?=225°. Insufficient data has been taken to substantiate that this is a result of a difference in the crossflow, but it has been shown to be repeatable rather than a single anomalous occurrence.

The wind tunnel side-wall pressures acquired using the instrumented window blank are shown in Figure 39 for the top-wall mounted jet. This is actually a different configuration than for the side-wall mounted jet, since the jet has now been moved to the top wall while the window blank remains in the same location. When the jet was mounted in the side wall, the window blank was positioned opposite it; now, it is positioned to one side of the jet (see Figure 5) because the jet is now located on the top wall and the window blank has not moved. The difference that this produces in the pressure distribution is evident in comparing the solid lines representing the top-wall mounted jet with the thinner dashed lines that reproduce the side-wall jet data first shown in Figure 29. Since Figures 36-38 indicate that the pressure field near the jet is essentially the same on the top wall as on the side wall, it is probably acceptable to regard the measurements in Figure 39 as accurate for the jet's relative side wall regardless of which wall into which the jet actually is mounted. That is, when the jet is mounted in the side wall, the data on Figure 39 would represent the pressure distribution found on the top wall or bottom wall of the wind tunnel.

With the exception of the region near ?=225° for the J=10.2 and $M_{¥}$=0.5 flow conditions in Figure 38b (and the instrumented window blank measurements, which were expected to differ), the pressure measurements with the jet mounted on the wind tunnel top wall are not significantly different that those with the jet mounted on the wind tunnel side wall. It is not definitive what is the source of this one exception, though a wind tunnel flow nonuniformity seems most plausible. Despite this lone discrepancy, the data indicate that the small alteration in the flowfield due to relocating the jet from the side wall to the top wall does not appreciably influence the measurements. This suggests that the data detailed in this report, the vast majority of which was acquired with the jet mounted in the side-wall position, is compatible with data acquired where the jet was mounted on the top wall, such as the schlieren measurements of Reference 36 or forthcoming laser diagnostics. However, while the present data supports such a concept, it is somewhat of an extrapolation because only pressure data have been examined and because the available data is only within the near-field of the jet. Other measurements could exhibit appreciable differences between the top-wall and side-wall jet interactions,

such as jet penetration into the freestream or far-field effects such as the location of the induced vortex pair.

4.5.2 Nozzle Wall Measurements

To provide additional evidence that the jet-in-crossflow interaction on the wind tunnel top wall is substantially the same as that on the side wall, the internally-instrumented nozzle was used to provide top-wall data. For unseparated cases, the data should be precisely identical since the pressure distribution inside the nozzle is not influenced by the crossflow, but instead results only from the nozzle nonuniformities found in section 4.4.2. This was confirmed experimentally for the top-wall mounting location, which provides further evidence that the piping to the settling chamber does not create the nonuniformities seen in Figure 32.

Figure 40 shows the nozzle wall surface pressures along a line on the upstream edge of the nozzle, analogous to the side-wall data shown in Figure 30. The black dashed lines included in Figure 40 represent the side-wall data from Figure 30 and thus provide a comparison between the top-wall and side-wall pressure traces. As in previous figures, two figures are shown, one to display the effects of varying P_{0j} while $M_{¥}$ remains constant at 0.8 and the other to show the effects of varying $M_{¥}$ while J is constant at 10.2. The figures show clearly that only for the two highly separated cases (J=2.8 and $M_{¥}$=0.8 in Figure 40a and J=10.2 and $M_{¥}$=0.5 in Figure 40b) can an appreciable difference be seen between the top-wall and side-wall pressures, and even here the variation is small. The differences are no larger than those seen in Figure 31 where the collapse with J was identified, which are well within the uncertainties established in section 4.4.2 above. Therefore, Figure 40 supports the conclusions of section 4.5.1 that the interaction produced by the top-wall mounted jet is not appreciably different from the interaction on the side wall.

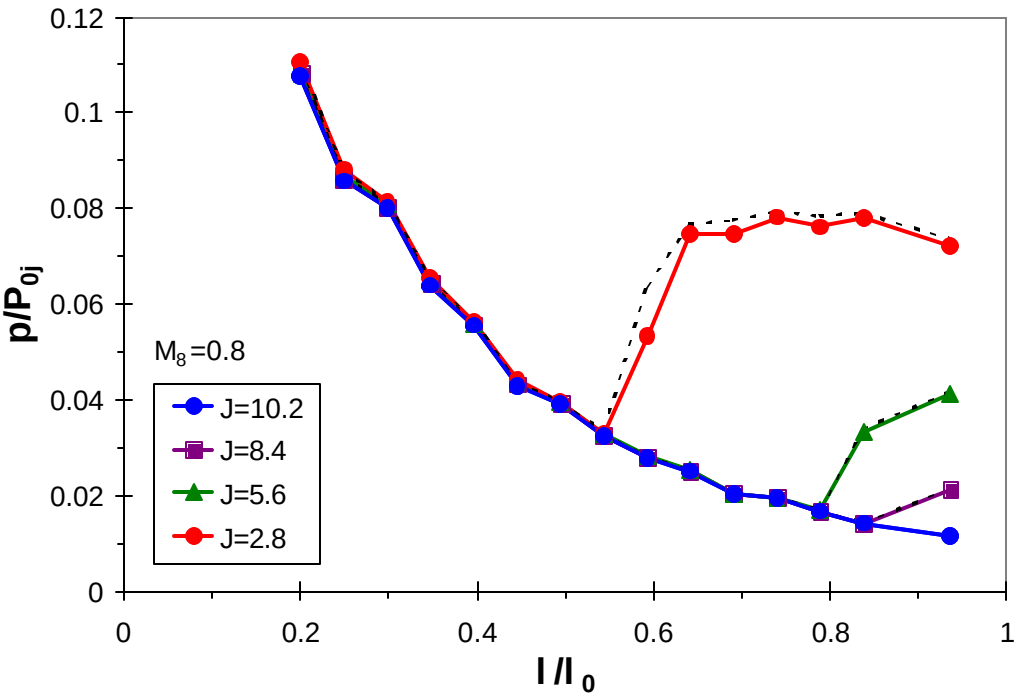

(a)

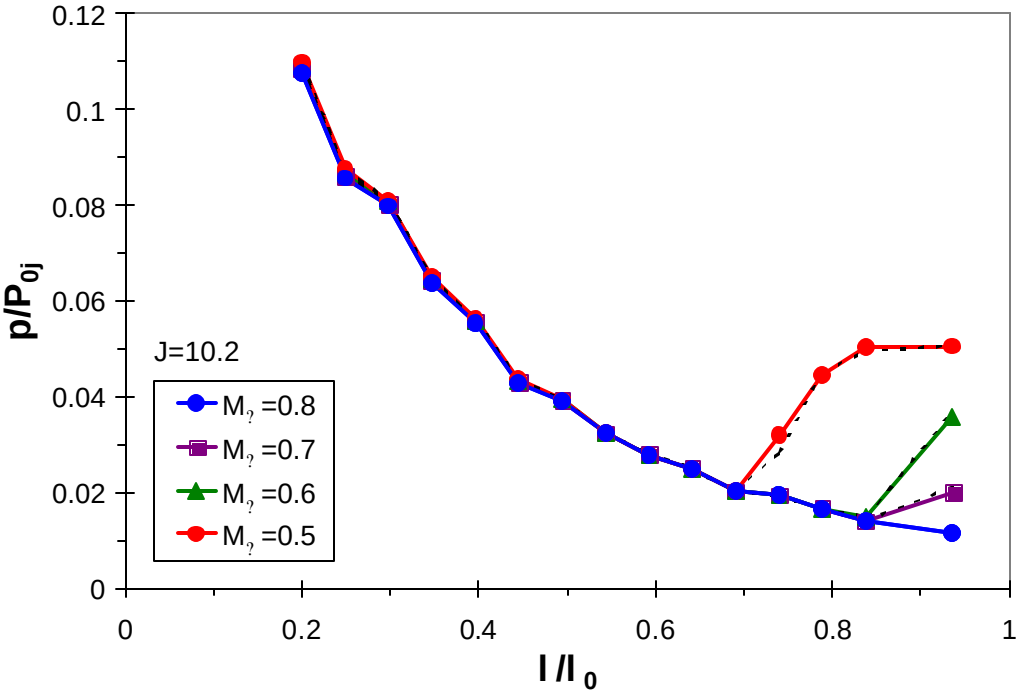

(b)

Figure 40: Mean nozzle internal surface pressures along a line on the nozzle's upstream edge with the nozzle mounted on the wind tunnel top wall. The black dashed lines represent the previous side-wall pressure measurements. (a) varying J while maintaining a constant M_8=0.8; (b) varying M_8 while maintaining a constant J=10.2.

5 Summary and Conclusions

The present investigation has examined the flowfield structure of an axisymmetric Mach 3.73 jet exhausting transversely from a flat plate into a subsonic compressible freestream. Experiments were conducted in a solid-wall, near-sonic test section using one wind tunnel wall as the flat plate from which the jet issued, which was determined to be a favorable configuration for quantitative comparison to computational simulations. Since the data are intended for use in validating computational models, attention is paid to providing details regarding the experimental geometry, boundary conditions, flowfield nonuniformities, and uncertainty analyses. Eight different sets of data are provided, covering a range of values of the jet-to-freestream dynamic pressure ratio and the freestream Mach number. Data include images of the mean surface flow features as identified by employing an oil-based flow tracer and a large volume of surface pressure coefficients measured on the both on the flat plate and on the nozzle internal wall.

The following conclusions can be drawn from the data:

- Wall surface pressure measurements were conducted in an empty wind tunnel (i.e., no jet exhausting into it) to provide baseline data with which a computation's ability to simulate the wind tunnel itself may be validated. The repeatability of these measurements was excellent and no substantial wind tunnel nonuniformity was identified through these data.

- Surface oil flow tracers provided qualitative images that show the locations of horseshoe vortices, reattachment lines, wake extent, and wake vortices. These observations provide a means by which to seek an approximate match with coherent structures predicted by computations.

- Mean surface pressure measurements on the flat plate from which the jet exhausts were gathered around the entire periphery of the jet to a radial extent of about four jet diameters. These data allow a quantitative comparison to computational results, and additionally identify features that are consistent with those visualized by the oil flow tracers.

- A mild flow nonuniformity was located using the flat plate pressure measurements, which appeared to result from both the flow through the test section and the jet plume itself. The latter source alternatively may be due to machining tolerances in the flat plate surface near the jet rather than the jet nozzle itself. Neither the jet settling chamber nor the incoming gas supply contribute to the flow nonuniformity. Although the nonuniformity was found to be the greatest source of uncertainty, the total uncertainty of the flat plate measurements remained small.

- A distinct flowfield nonuniformity was found in the surface pressures along the jet nozzle internal wall. This nonuniformity is created by the nozzle itself and not the crossflow into which it exhausts or the jet stagnation chamber or gas supply. Therefore the supersonic expansion through the nozzle is somewhat nonuniform.

- A substantial bias in the nozzle wall pressure measurements may be created by the large size of the pressure taps with respect to the small nozzle dimensions. Although estimating the magnitude of this bias is difficult, it appears to be strongest near the nozzle throat and may remain a significant contributor to the pressure uncertainties nearer the nozzle exit. However, this bias does not inhibit the ability to detect nozzle flow separation since separation is characterized by a distinct pressure rise regardless of the bias superimposed upon it.

- Although the wind tunnel boundary layer thickness is about 10% smaller on the top wall than on a side wall, no appreciable difference has been found in the jet-in-crossflow interaction produced on the top wall as compared to that produced on a side wall. This suggests that optically-based data acquired using the top-wall configuration in other studies are fully compatible with the predominant side-wall pressure data provided in the present study.

- The present study has confirmed that for a given value of the freestream Mach number M_8, the data collapse with the jet-to-freestream dynamic pressure ratio J. This knowledge can be used to limit the number of computational cases that need to be validated.

- Both the pressure measurements and the surface flow tracers show that as either J or M_8 is increased, the size of the horseshoe vortex system increases, as does the extent of the jet's wake. The pressure increase in the stagnation region at the leading edge of the jet and the pressure drop in the wake become stronger as J or M_8 increase. The structure of the wake vortices is complex and shifts greatly with the flow conditions.

- Surface pressure data acquired on the nozzle wall have shown that nozzle flow separation does occur under flowfield conditions that may be found on flight vehicles. Furthermore, the axially asymmetric nature of the separation has been identified, which results from the angular variation in the backpressure on the nozzle generated by the jet's interaction with the freestream. As either J or $M_¥$ is reduced, the size of the separated flow region becomes larger because the backpressure on the nozzle is increased.

- Surface pressures also were recorded along the centerline of the wall opposite the jet and on one wall adjacent to the jet to provide data on the pressure drop induced in the solid-wall test section by the presence of the jet.

6 References

1 Chocinski, D., Leblanc, R., and Hachemin, J.-V., "Experimental/Computational Investigation of Supersonic Jet in Subsonic Compressible Crossflow," AIAA Paper 97-0714, January 1997.

2 Chocinski, D., "Contribution to the Modeling of Interactions of a Supersonic Jet in a Subsonic Compressible Crossflow," Doctoral Thesis, University of Poitiers, France, 1998.

3 Reichenau, D. E. A., "Interference Effects Produced by a Cold Jet Issuing Normal to the Airstream from a Flat Plate," AEDC TR-67-220, October 1967.

4 Lee, E. E. Jr, and Willis, C. M., "Interaction Effects of a Control Jet Exhausting Radially from the Nose of an Ogive-Cylinder Body at Transonic Speeds," NASA TN D-3752, January 1967.

5 Manela, J., and Seginer, A., "Interaction of Multiple Supersonic Jets with a Transonic Flowfield," *AIAA Journal*, Vol. 24, No. 3, 1986, pp. 418-423.

6 Kuiper, R. A., "Control Jet Effectiveness in the Subsonic and Transonic Flight Regimes," Philco Aeronautic Division publication U-2932, December 1964.

7 Cassel, L. A., Durando, N. A., Bullard, C. W., and Kelso, J. M., "Jet Interaction Control Effectiveness for Subsonic and Supersonic Flight," Report No. RD-TR-69-21, U. S. Army Missile Command, Redstone Arsenal, September 1969.

8 Manela, J., and Seginer, A., "Jet Penetration Height in Transonic Flow," *AIAA Journal*, Vol. 24, No. 1, 1986, pp. 67-73.

9 Spring, D. J., "An Experimental Investigation of the Interference Effects Due to a Lateral Jet Issuing from a Body of Revolution over the Mach Number Range of 0.8 to 5," Report No. RD-TR-68-10, U.S. Army Missile Command, Redstone Arsenal, August 1968.

10 Dahlke, C. W., "An Experimental Investigation of Downstream Flow-Field Properties Behind a Sonic Jet Injected into Transonic Free Stream from a Body of Revolution," Report No. RD-TR-69-2, U.S. Army Missile Command, Redstone Arsenal, February 1969.

11 Street, T. A., "An Experimental Investigation of a Transverse Jet Ejecting from a Flat Plate into a Subsonic Free Stream," Report No. RD-TM-70-5, U.S. Army Missile Command, Redstone Arsenal, May 1970.

12 Shaw, C. S., and Margason, R. J., "An Experimental Investigation of a Highly Underexpanded Sonic Jet Ejecting from a Flat Plate into a Subsonic Crossflow," NASA TN D-7314, December 1973.

13 Wang, K. C., Smith, O. I., and Karagozian, A. R., "In-Flight Imaging of Transverse Gas Jets Injected into Compressible Crossflows," *AIAA Journal*, Vol. 33, No. 12, 1995, pp. 2259-2263.

14 Green, L. Jr., "Flow Separation in Rocket Nozzles," *ARS Journal*, Vol. 23, No. 1, 1953, pp. 34-35.

15 Summerfield, M., Foster, C. R., and Swan, W. C., "Flow Separation in Overexpanded Supersonic Exhaust Nozzles," *Jet Propulsion*, Vol. 24, Sep-Oct 1954, pp. 319-321.

16 Page, R. H., "Flow Separation in Nozzles," *Journal of the Aerospace Sciences*, Vol. 29, January 1962, pp. 110-111.

17 Schilling, M., "Flow Separation in a Rocket Nozzle," M. S. Thesis, Graduate School of Arts and Sciences, University of Buffalo, Buffalo, NY, June 1962.

18 Arens, M., and Spiegler, E., "Shock-Induced Boundary Layer Separation in Overexpanded Conical Exhaust Nozzles," *AIAA Journal*, Vol. 1, No. 3, 1963, pp. 578-581.

19 Arens, M., "The Shock Position in Overexpanded Nozzles," *Journal of the Royal Aeronautical Society*, Vol. 67, April 1963, pp. 268-269.

20 Sunley, H. L. G., and Ferriman, V. N., "Jet Separation in Conical Nozzles," *Journal of the Royal Aeronautical Society*, Vol. 68, December 1964, pp. 808-818.

21 Kalt, S., and Badal, D. L., "Conical Rocket Nozzle Performance under Flow-Separated Conditions," *Journal of Spacecraft*, Vol. 2, No. 3, 1965, pp. 447-449.

22 Miller, E. H., and Migdal, D., "Separation and Stability Studies of a Convergent-Divergent Nozzle," *Journal of Aircraft*, Vol. 7, No. 2, 1970, pp. 159-163.

23 Morrisette, E. L., and Goldberg, T. J., "Turbulent-Flow Separation Criteria for Overexpanded Supersonic Nozzles," NASA TP-1207, 1978.

24 Chen, C. L., Chakravarthy, S. R., and Hung, C. M., "Numerical Investigation of Separated Nozzle Flows," *AIAA Journal*, Vol. 32, No. 9, 1994, pp. 1836-1843.

25 Hamed, A., and Vogiatzis, C., "Overexpanded Two-Dimensional Convergent-Divergent Nozzle Performance, Effects of Three-Dimensional Flow Interactions," *Journal of Propulsion and Power*, Vol. 14, No. 2, 1998, pp. 234-240.

26 Romine, G. L., "Nozzle Flow Separation," *AIAA Journal*, Vol. 36, No. 9, 1998, pp. 1618-1625.

27 Hunter, C. A., "Experimental, Theoretical, and Computational Investigation of Separated Nozzle Flows," AIAA Paper 98-3107, July 1998.

28 Frey, M., and Hagemann, G., "Restricted Shock Separation in Rocket Nozzles," *Journal of Propulsion and Power*, Vol. 16, No. 3, 2000, pp 478-484.

29 Murdock, J. W., and Welle, R. P., "Downstream Gas Effect on Nozzle Flow-Separation Location," *Journal of Propulsion and Power*, Vol. 17, No. 4, 2001, pp. 935-937.

30 American Institute of Aeronautics and Astronautics, "Guide for the Verification and Validation of Computational Fluid Dynamics Simulations," AIAA G-077-1998, 1998.

31 Oberkampf, W. L., and Blottner, F. G., "Issues in Computational Fluid Dynamics Code Verification and Validation," *AIAA Journal*, Vol. 36, No. 5, 1998, pp. 687-695.

32 Aeschliman, D. P., and Oberkampf, W. L., "Experimental Methodology for Computational Fluid Dynamics Code Validation," *AIAA Journal*, Vol. 36, No. 5, 1998, pp. 733-741.

33 Oberkampf, W. L., and Trucano, T. G., "Validation Methodology in Computational Fluid Dynamics," AIAA Paper 2000-2549, June 2000.

34 McWherter-Payne, M. A., and Salari, K., "SACCARA Verification and Validation Plan, Version 1.0," Sandia Report SAND2000-1346, June 2000.

35 Beresh, S. J., Henfling, J. F., and Erven, R. J., "Surface Measurements of a Supersonic Jet in Subsonic Compressible Crossflow," AIAA Paper 2001-2786, June 2001.

36 Beresh, S. J., Henfling, J. F., and Erven, R. J., "Flow Separation Inside a Supersonic Nozzle Exhausting into a Subsonic Compressible Crossflow," AIAA Paper 2002-1067, January 2002.

37 McKee, M. L., "Digital Computer Oriented Methods for Determining the Response of Pressure Measurement to Step and Ramp Forcing Functions," AEDC Report TR-66-225, March 1967.

38 Shaw, R., "The Influence of Hole Dimensions on Static Pressure Measurements," *Journal of Fluid Mechanics*, Vol. 7, 1960, pp 550-563.

39 Guy, R. W., and Winebarger, R. M., "Effect of Orifice Size and Heat-Transfer Rate on Measured Static Pressures in a Low-Density Arc-Heated Wind Tunnel," NASA TN D-3829, February 1967.

40 Rainbird, W. J., "Errors in Measurement of Mean Static Pressure of a Moving Fluid Due to Pressure Holes," *National Aeronautical Establishment Quarterly Bulletin*, 1967, No. 3, pp 55-89.

41 Moulden, T. H., Wu, J. M., Collins, F. G., and Ramon, H. J., "Experimental Study of Static Pressure Orifice Interference," AEDC TR 77-57, June 1977.

42 Flack, R. D. Jr., "Static Pressure Hole Errors in Transonic Flow with Pressure Gradients," *ISA Transactions*, Vol. 17, No. 4, 1978, pp. 89-95.

43 Ducruet, C., and Dyment, A., "The Pressure-Hole Problem," *Journal of Fluid Mechanics*, Vol. 142, 1984, pp. 251-267.

44 Ducruet, C., "A Method for Correcting Wall Pressure Measurements in Subsonic Compressible Flow," *Transactions of the ASME*, Vol. 113, June 1991, pp. 256-260.

45 Fric, T. F., and Roshko, A., "Vortical Structure in the Wake of a Transverse Jet," *Journal of Fluid Mechanics*, Vol. 279, 1994, pp. 1-47.

46 Krothapalli, A., Lourenco, L., and Buchlin, J. M., "Separated Flow Upstream of a Jet in a Crossflow," *AIAA Journal*, Vol. 28, No. 3, 1990, pp. 414-420.

47 Kelso, R. M., and Smits, A. J., "Horseshoe Vortex Systems Resulting from the Interaction between a Laminar Boundary Layer and a Transverse Jet," *Physics of Fluids*, Vol. 7, No. 1, 1995, pp. 153-158.

48 Kelso, R. M., Lim, T. T., and Perry, A. E., "An Experimental Study of Round Jets in Cross-flow," *Journal of Fluid Mechanics*, Vol. 306, 1996, pp. 111-144.

49 Sykes, R. I., Lewellen, W. S., and Parker, S. F., "On the Vorticity Dynamics of a Turbulent Jet in a Crossflow," *Journal of Fluid Mechanics*, Vol. 168, 1986, pp. 393-413.

50 Yuan, L. L., Street, R. L., and Ferziger, J. H., "Large-eddy Simulations of a Round Jet in Crossflow," *Journal of Fluid Mechanics*, Vol. 379, 1999, pp. 71-104.

51 Everett, D. E., Woodmansee, M. A., Dutton, J. C., and Morris, M. J., "Wall Pressure Measurements for a Sonic Jet Injected Transversely into a Supersonic Crossflow," *Journal of Propulsion and Power*, Vol. 14, No. 6, 1998, pp. 861-868.

52 Gruber, M. R., and Goss, L. P., "Surface Pressure Measurements in Supersonic Transverse Injection Flowfields," *Journal of Propulsion and Power*, Vol. 15, No. 5, 1999, pp. 633-641.

53 Orth, R. C., and Funk, J. A., "An Experimental and Comparative Study of Jet Penetration in Supersonic Flow," *Journal of Spacecraft*, Vol. 4, No. 9, 1967, pp. 1236-1242.

54 Kamotani, Y., and Greber, I., "Experiments on a Turbulent Jet in a Cross Flow," *AIAA Journal*, Vol. 10, No. 11, 1972, pp. 1425-1429.

55 Papamoschou, D., and Hubbard, D. G., "Visual Observations of Supersonic Transverse Jets," *Experiments in Fluids*, Vol. 14, 1993, pp. 468-471.

56 Margason, R. J., "Fifty Years of Jet in Cross Flow Research," *Computational and Experimental Assessment of Jets in Cross Flow*, AGARD CP 534, 1993, pp. 1.1-1.41.

(this page intentionally left blank)

Distribution

External

Kevin C. Greenaugh
NA-115.3/Forrestal Building
U.S. Department of Energy
1000 Independence Ave., S.W.
Washington, D.C. 20585

William R. Roy-Harrison
NA-115.3/Forrestal Building
U.S. Department of Energy
1000 Independence Ave., S.W.
Washington, D.C. 20585

T. Y. Chu
NA-115.3/Forrestal Building
U.S. Department of Energy
1000 Independence Ave., S.W.
Washington, D.C. 20585

Sandia Internal

MS 0121	1200	C. M. Hart
MS 0429	2100	J. S. Rottler
MS 0453	2110	G. A. Sanders
MS 0447	2111	J. D. Mangum
MS 0447	2111	K. R. Eklund
MS 0447	2111	P. R. Hooper
MS 0447	2111	P. D. Hoover
MS 0447	2111	S. E. Pink
MS 0479	2113	J. O. Harrison
MS 0453	2130	H. J. Abeyta
MS 0427	2134	R. A. Paulsen
MS 9005	2820	R. G. Miller
MS 0634	2951	K. V. Chavez
MS 9007	8200	D. R. Henson
MS 9005	8220	G. A. Thomas
MS 9034	8221	R. N. Everett
MS 9405	8700	R. H. Stulen
MS 9402	8703	K. L. Wilson
MS 0841	9100	T. C. Bickel
MS 0841	9100	C. W. Peterson
MS 0824	9110	A. C. Ratzel
MS 0834	9112	M. R. Prairie

MS 0834	9112	V. A. Amatucci
MS 0834	9112	S. J. Beresh (25 copies)
MS 0834	9112	C. J. Bourdon
MS 0834	9112	R. J. Erven
MS 0834	9112	J. F. Henfling
MS 0825	9115	B. Hassan
MS 0825	9115	F. G. Blottner
MS 0825	9115	J. A. Keenan
MS 0825	9115	D. W. Kuntz
MS 0825	9115	M. A. McWherter-Payne
MS 0825	9115	J. L. Payne
MS 0825	9115	C. J. Roy
MS 0825	9115	W. P. Wolfe
MS 0824	9130	J. L. Moya
MS 0828	9133	M. Pilch
MS 0828	9133	W. L. Oberkampf
MS 0835	9140	M. J. McGlaun
MS 0819	9211	T. G. Trucano
MS 0421	9800	W. L. Hermina
MS 0139	9900	M. O. Vahle
MS 0139	9902	P. J. Wilson
MS 0139	9905	S. E. Lott
MS 1174	15414	W. R. Rutledge
MS 0825	15414	J. B. Christensen
MS 1174	15426	R. W. Greene
MS 9018	8945-1	Central Technical Files
MS 0899	9616	Technical Library (2 copies)
MS 0612	9612	Review & Approval Desk for DOE/OSTI